January 2014

A Feasibility Study On The Implementation Of Satellite-To-Satellite Tracking Around A Small Near-Earth Object

Christopher Joseph Church

[How does access to this work benefit you? Let us know!](#)

Follow this and additional works at: https://commons.und.edu/theses

A FEASIBILITY STUDY ON THE IMPLEMENTATION OF SATELLITE-TO-SATELLITE TRACKING AROUND A SMALL NEAR-EARTH OBJECT

by

Christopher J. Church
Bachelor of Science, James Madison University, 2005

A Thesis

Submitted to the Graduate Faculty

of the

University of North Dakota

in partial fulfillment of the requirements

for the degree of

Master of Science

Grand Forks, North Dakota
May
2014

This thesis, submitted by Christopher Church in partial fulfillment of the requirements for the Degree of Master of Science from the University of North Dakota, has been read by the Faculty Advisory Committee under whom the work has been done and is hereby approved.

Dr. Ronald A. Fevig, Chairperson

Dr. Michael J. Gaffey

Dr. Paul S. Hardersen

Dr. William H. Semke

This thesis is being submitted by the appointed advisory committee as having met all of the requirements of the School of Graduate Studies at the University of North Dakota and is hereby approved.

Dr. Wayne Swisher,
Dean of the Graduate School

May 7, 2014
Date

iii

PERMISSION

Title   A Feasibility Study on the Implementation of Satellite-to-satellite
Tracking Around a Small Near-Earth Object

Department   Space Studies

Degree   Master of Science

       In presenting this thesis in partial fulfillment of the requirements for a graduate degree from the University of North Dakota, I agree that the library of this University shall make it freely available for inspection. I further agree that permission for extensive copying for scholarly purposes may be granted by the professor who supervised my thesis work or, in their absence, by the chairperson of the department or the dean of the Graduate School. It is understood that any copying or publication or other use of this dissertation or part thereof for financial gain shall not be allowed without my written permission. It is also understood that due recognition shall be given to me and to the University of North Dakota in any scholarly use which may be made of any material in my thesis.

Christopher Church

April 7, 2014

TABLE OF CONTENTS

LIST OF FIGURES

LIST OF TABLES

ACKNOWLEDGEMENTS

To my son, Nicolas

ABSTRACT

Near-earth objects (NEOs) are asteroids and comets that have a perihelion

distance of less than 1.3 astronomical units (AU). There are currently more than 10,000

known NEOs. The majority of these objects are less than 1 km in diameter. Despite the

number of NEOs, little is known about most of them. Characterizing these objects is a

crucial component in developing a thorough understanding of solar system evolution,

human exploration, exploitation of asteroid resources, and threat mitigation. Of

particular interest is characterizing the internal structure of NEOs. While ground-based

methods exist for characterizing the internal structure of NEOs, the information that can

be gleaned from such studies is limited and often accompanied by large uncertainty. An

alternative is to use in situ studies to examine an NEO's shape and gravity field, which

can be used to assess its internal structure.

This thesis investigates the use of satellite-to-satellite tracking (SST) to map the

gravity field of a small NEO on the order of 500 m or less. An analysis of the mission

requirements of two previously flown SST missions, GRACE and GRAIL, is conducted.

Additionally, a simulation is developed to investigate the dynamics of SST in the vicinity

of a small NEO. This simulation is then used to simulate range and range-rate data in the

strongly perturbed environment of the small NEO. These data are used in conjunction

with the analysis of the GRACE and GRAIL missions to establish a range of orbital

parameters that can be used to execute a SST mission around a small NEO. Preliminary

mission requirements for data collection and orbital correction maneuvers are also

established. Additionally, the data are used to determine whether or not proven technology can be used to resolve the expected range and range-rate measurements.

It is determined that the orbit semi-major axis for each spacecraft should be approximately 100% to 200% of the NEO's mean diameter and the two spacecraft should be in circular, near polar orbits. This configuration will produce trajectories, which exhibit reasonable stability over a period of roughly 24 hours. Corrective maneuvers will therefore be required with a frequency of approximately once per day. Due to the potentially rapid changes caused by the highly perturbed environment, it is likely that these maneuvers will need to be made autonomously. During the period between corrective maneuvers SST data collection will be possible. The expected range and range-rate measurements will be on the order of $\pm 10^{-5}$ m and $\pm 10^{-5}$ m/s respectively and can be resolved using proven technology.

CHAPTER I.

INTRODUCTION

Overview

The first NEO designated 433 Eros, was discovered in 1898. There are currently, more than 10,000 known Near-Earth Objects (NEO) and more are continually being discovered. Nearly 97% of the currently known NEOs were discovered in the last 20 years. This can largely be attributed to the recommendation made by the American Institute of Aeronautics and Astronautics in 1990 to the U.S. House Committee of Science and Technology to increase the detection rate of NEOs (Morrison, 1992). Several years later in 1998, the National Aeronautics and Space Administration (NASA) was directed to detect, track, catalogue, and characterize all NEOs larger than 1 km. This initiative created the NEO survey program. The 1 km size limit was later reduced to all NEO larger than 140 m by the 2005 amendment to the National Aeronautics and Space Administration Act of 1958 (HR1022).

The majority of the NEOs discovered since the implementation of the Near Earth Object program, are small asteroids less than 1 kilometer in diameter and despite their numbers, little is known about the majority of these objects. Characterization of NEOs, and in particular, their internal structure, is an important component in developing a thorough understanding of solar system evolution, human exploration, exploitation of asteroid resources, and threat mitigation.

While characterization of the internal structure can be achieved with some degree of accuracy using a variety of ground-based techniques, it is challenging to apply these methods to small NEOs for a variety of reasons. Because the majority of NEOs are less than 1 kilometer in diameter, ground-based studies are not well suited for conducting extensive studies of these objects. Obtaining detailed information regarding the internal structure of a small NEO therefore requires another type of investigative technique. One option that is well suited to such a detailed investigation is an in situ study. In fact, one of the key goals for future asteroid missions will be to characterize the internal structure of the target (Scheeres, 2012b). However, placing a spacecraft in orbit around a small NEO presents its own set of challenges.

This thesis considers these challenges and examines the concept of satellite-to-satellite tracking (SST) around a small NEO on the order of 500 meters or less. In addition to the general requirement that the spacecraft occupy circular, near polar orbits commensurate with low-low SST, it is determined that the following will be required in order to implement SST to map the object's gravity field:

1. Semi-major axis maintained between approximately 100% and 200% of the central body's mean diameter;

2. Autonomous guidance and navigation of each spacecraft;

3. Execution of orbit corrections maneuvers with a frequency of approximately once per day; and

4. Each spacecraft must carry instrumentation capable of measuring range and range-rate with an accuracy of $\pm 10^{-5}$ m and $\pm 10^{-5}$ m/s respectively.

The concept of low-low SST has been around for at least 40-years and successfully demonstrated twice, first to map earth's gravity field and later to map the lunar gravity field. Several data analysis techniques have been established and the required hardware has proven flight heritage. However, to date, the use of SST to characterize the internal structure of an object other than the earth and Moon has not been attempted. Utilization of this technique to map the gravity field of a small NEO poses many challenges, which are considered throughout this thesis. It is questionable whether or not this method can be successfully applied in the environment around a small NEO and subsequently yield data that can be used to characterize its internal structure. This characterization estimates the object's internal mass distribution and constrains its bulk density and porosity.

This work determines whether or not two spacecraft can be placed in orbit around a small NEO and successfully resolve SST data based on existing technology. It also considers the limits associated such capabilities and establishes constraints for the orbit parameters, data collection, and mission duration. While this work does not attempt to use the data generated to produce a gravity model or assess the internal structure of a small NEO, consideration is given to understanding these topics and their relationship. It is assumed that the data analysis methods are understood to the extent that if data collection is possible it could be processed to generate a gravity model and constrain the internal structure of the object.

The remainder of Chapter I provides a brief history of the development of this research and the evolution of the work presented here. The key terminology used throughout, is also presented followed by a summary of the results obtained.

Chapter II briefly discusses the relationship between gravity models and internal structure. This is followed by an overview of the fundamentals of internal structure and a summary of current ground-based techniques used to study NEOs. The results achieved via in situ observations from the NEAR-Shoemaker and Hayabusa missions are then discussed for comparison.

Chapter III discusses the methodology used for both the systems analysis and STK simulation portions of this research.

Chapter IV presents the systems analysis research into the Gravity Recovery and Climate Experiment (GRACE) and the Gravity Recovery and Interior Laboratory (GRAIL) missions.

Chapter V describes the development of the STK simulation environment and Chapter VI presents the simulated data and subsequent analysis.

Chapter VII discusses the results presented in Chapter IV and Chapter VI. It compares the systems analysis with the STK simulation data and establishes the limits associated with SST operations around a small NEO. An assessment regarding the feasibility of such a mission based on the technology evaluated in Chapter IV is made. This chapter concludes with recommendations for further investigation into utilizing gravity mapping to assess the internal structure of a small NEO and proposes possible alternatives to SST.

<div align="center">Terminology</div>

Near-Earth Object (NEO) – Asteroid or comet with a perihelion distance less than 1.3 Astronomical Units (AU) (Near earth object program.2014).

Line of Sight (LOS) – An imaginary line joining two spacecraft.

Satellite-to-Satellite tracking (SST) – A method of detecting orbit perturbations caused by an irregular gravity field.

Low-low SST – Doppler shifts in a signal transmitted between the two spacecraft in coplanar orbits are measured to determine the LOS separation of the two spacecraft as well as their relative velocity.

Systems Toolkit (STK) – Software package developed by Analytical Graphics to model and analyze space, defense, and intelligence systems.

High-precision Orbit propagator (HPOP) – Algorithms that use various force models and numerical integration techniques to generate satellite ephemerid.

Solar radiation pressure (SRP) – Force is exerted on an object as a result of reflection or absorption of solar photons.

Summary of Results

The results presented in Chapter IV and Chapter VI show that under certain conditions, two spacecraft could be placed in orbit around a small NEO. Based on these conditions, it should be possible to collect data sufficient to map the object's gravity field using low-low SST. It is shown that for a NEO approximately 500 m in diameter, circular, near polar orbits with a radius of between 750 m and 1000 m produce the most stable trajectories for SST data collection. The strongly perturbed environment around the NEO causes the trajectories of the two spacecraft to diverge relatively rapidly. In nearly all cases examined, the orbits of the two spacecraft begin to diverge significantly within approximately 3-days. In most cases where this divergence is observed, one or both spacecraft enter an escape trajectory or impact the asteroid. In order to maintain the close orbit formation required for low-low SST, corrective maneuvers with a minimum

frequency of once per day would be necessary. Additionally, the rapid orbit decays observed as a result of the strongly perturbed environment will require that these maneuvers be executed autonomously.

Prior to significant divergence of the two spacecraft trajectories, the relative positions and velocities observed between them would be detectable using current technology based on the systems analysis conducted in Chapter IV. Therefore, implementation of low-low SST around a small NEO will require instrumentation with measurement capabilities equivalent or better than those included on the GRACE and GRAIL missions.

Research History

The original proposal for the work presented in this thesis stated that the goal of the research was to determine if and how accurately small spacecraft can characterize and constrain the internal structure of NEO smaller than around 500 meters. The research would consider this question from two different perspectives. The first of these would be from a systems analysis perspective where the individual payload elements required by the techniques being considered would be evaluated to determine if they could be deployed onboard small spacecraft. The second portion of the research would focus on the development of a simulation, based on a known NEO. This simulation would be used to generate spacecraft tracking data, which would in turn be used to produce a gravity model for the object. The gravity model would then be used to characterize the internal structure and compare it to an accepted model for the object. The results from these two segments of the research would be analyzed to conclude whether or not small spacecraft employing spacecraft tracking techniques can be used to constrain the internal structure

of small NEO based on the measurement capabilities of flight proven technology. While the methodology behind the systems analysis and simulation did not change significantly during the course of this work, the overall scope of what this thesis would achieve did.

To address the systems analysis portion of this work, several techniques capable of characterizing the internal structure of an object would be investigated. These originally included both high-low and low-low SST and radar tomography. While radar tomography has been studied in some detail, it has not been demonstrated on any asteroid missions to date. Because of this, it is excluded from the work presented here and emphasis is placed on SST. Both forms of SST have been successfully demonstrated around solar system bodies. Some of the missions that demonstrated these technologies include NEAR, GRACE, and GRAIL. In addition to these three missions, the Hayabusa mission was also investigated. While Hayabusa did not actually enter orbit around its target, the asteroid Itokawa is near the upper limit of the size being considered for this work.

The terms "small spacecraft" as they relate to this work were not clearly defined by the initial research proposal and continue as such in the work presented here. Because of this, the systems analysis research focuses primarily on instrument resolutions and measurement accuracies, rather than the ability to deploy these instruments onboard a spacecraft. Therefore, the "small spacecraft" component of this work was eliminated in favor of evaluating flight proven hardware.

The simulation portion of the research was initially developed using the software package STK version 9.2 and was later extended STK version 10.0.2. Asteroid Itokawa was used as the central body being investigated in the simulation. Development of this

simulation and model for Itokawa is discussed in detail in Chapter V. The original goal

was to use data generated from this simulation to produce a gravity model for Itokawa

and compare it to the accepted model. This goal led to a search for gravity modeling

software, which would use the data exported from STK to estimate the gravity

coefficients for Itokawa. Several avenues were pursued in this search. Software

packages including Geodyn and Orbit Reconstruction, Simulation, and Analysis (ORSA)

were examined. Geodyn was developed and is maintained by the Space Geodesy group

at NASA's Goddard Spaceflight center. Pasquale Tricarico at the Planetary Science

Institute developed ORSA. Estimation of the gravity coefficients was also pursued using

a method presented by Jekeli (1999) and further detailed by Han (2004).   It was

determined that each of these three methods would require efforts beyond the scope of

this thesis to employ. However, the research leading to this conclusion led to several

additional questions, which were not directly considered in the original research proposal.

Answering these questions is critical to being able to conclusively answer the overall

research question. Ultimately, this development led to a revised set of objectives for this

thesis.

Throughout this work, the immense scope of the original question became

increasingly clear. In order to conclusively answer the original question of whether or

not small spacecraft can use spacecraft tracking methods to characterize the internal

structure of small NEO, it has become evident that several interim questions must be

considered first. These questions have become the focus of this thesis with the intention

that their answers will permit continuation of this work toward the ultimate goal of

characterizing the internal structure of a small NEO using simulated data and conclusively answering the original research question.

The interim questions that have been established throughout this work can be broken into three categories; instrument precision, data requirements, and orbit dynamics. Instrument precision considers the performance requirements that are demanded by a small NEO mission. For instance, is existing technology capable of resolving the range and range-rate measurements that can be expected between spacecraft? Data requirements address not only the type and amount of data required but also the constraints on data collection intervals, breaks in the data stream, etc. Finally, orbit dynamics considers the ability to place a spacecraft in orbit about a small NEO, the stability of the orbit, and the requirements for orbit maintenance (frequency, effects on data collection, etc.).

My original thesis proposal addresses the first two of these categories to some extent in the systems analysis section. However, it ended with characterizing the payload elements and determining if they could be integrated into a small spacecraft. While this is still an important component to my research, there is the additional and perhaps more important question of whether or not these systems are capable of measuring with the accuracy necessary to track spacecraft around a small NEO. As it was proposed, the simulation portion of this investigation would address the orbital dynamics on a high level by attempting to estimate the gravity coefficients for the simulated NEO and only a high level correlation between data collection and orbit dynamics was suggested. The finer details of orbital dynamics in the vicinity of small NEO were not being considered directly.

Throughout this research, questions involving spacecraft dynamics around a small asteroid have surfaced. These include questions such as; How precise do the measurements need to be regarding position, velocity, range, range-rate, etc.? What orbit parameters need to be maintained? How stable is the orbit? How frequently will corrective maneuvers need to be made to each spacecraft's orbit? The answers to these questions affect how well or even if SST can be used to characterize the internal structure of small NEO. The questions will be answered by comparing the systems analysis and the simulated STK data. For example, initial results from the simulation indicate that the orbits of two spacecraft, initially in a configuration similar to GRACE and GRAIL, will diverge significantly within a few days (Church & Fevig, 2013). Because of this, corrective maneuvers will be required to maintain the desired orbit configuration, which will affect data collection.

The developments discussed above have led to revised objectives for this thesis. These objectives are as follows:

1. Determine a range of orbital parameters required for a low-low SST mission around a small NEO;

2. Determine the time available for data collection between orbital correction maneuvers; and

3. Determine the range and range-rate measurement requirements and whether or not these can be met using the technology proven by GRACE and GRAIL.

The work presented below will address these objectives and the conclusions made here will form the basis for continued research into characterizing the internal structure of small NEO and NEO mission design in general.

CHAPTER II.

BACKGROUND

Gravity Models

According to Newton's law of gravity, the force of gravity experienced between two objects is directly proportional to the product of their two masses and inversely proportional to the square of the distance between them. This law may be used to derive the acceleration felt by one mass caused by the gravitational attraction of the other. In the case of a spacecraft orbiting a planet, moon, or even an asteroid, this same relationship can be used to calculate its acceleration at some location **r** with respect to the object's center of mass and is given by Equation (1).

$$\ddot{\boldsymbol{r}} = -\frac{GM_{CB}}{r^3}\boldsymbol{r} \tag{1}$$

In Equation (1), M_{CB} represents the mass of the object being orbited, **r** is the location of the satellite, and G is the gravitational constant equal to $6.67259 \pm 0.00085 \times 10^{-11}$ m^3/kgs^2 (Montenbruck & Gill, 2000). Equation (1) is representative of the motion of a spacecraft with negligible mass in a gravitational field created by an object with mass, M_{CB}. Its use assumes that all the mass is concentrated at the center of the object. This is a valid assumption provided the mass distribution is uniform and spherically symmetric. However, this is not true in nature and serves only as a first order approximation when considering the motion of spacecraft in orbit around a solar system body. An extended

object such as a planet, moon, or asteroid is not generally spherically symmetric nor is the distribution of mass within it uniform. These deviations invalidate the assumptions made in Equation (1). Therefore, a more accurate model of the gravity field is required for extended objects.

To remedy the situation, it is convenient to define the gravitational potential U by Equation (2).

$$U = \frac{GM_{CB}}{r} \tag{2}$$

The acceleration felt by a satellite due to the gravitational field created by M_{CB} can then be written as the gradient of the potential as shown in Equation (3), where ∇ is the vector gradient operator defined in Cartesian coordinates and $\hat{x}, \hat{y},$ and $\hat{z}$ are unit vectors in the x, y, and z directions.

$$\ddot{\boldsymbol{r}} = \nabla U = \frac{\partial U}{\partial x}\hat{x} + \frac{\partial U}{\partial y}\hat{y} + \frac{\partial U}{\partial z}\hat{z} \tag{3}$$

When considering the gravitational potential due to an extended object, the object may be treated as if it is made up of individual mass elements. By doing this, the potential in Equation (3) may be generalized to any arbitrary mass distribution consisting of individual mass elements $dm = \rho(\boldsymbol{s})d^3\boldsymbol{s}$ (Montenbruck & Gill, 2000). Summing these individual mass elements over the entire body yields Equation (4). This expression represents the potential due to an arbitrary mass distribution.

13

$$U = \mathrm{G} \int \frac{\rho(\boldsymbol{s})}{|\boldsymbol{r} - \boldsymbol{s}|} d^3\boldsymbol{s} \tag{4}$$

The vector $\boldsymbol{s}$ locates the individual mass element within the extended object and $|\boldsymbol{r} - \boldsymbol{s}|$ is the distance between the satellite and the mass element.

Outside of a circumscribing sphere (sometimes referred to as a Brillouin Sphere) encompassing the object, Equation (4) is a harmonic function, which satisfies Laplace's equation, $\nabla^2 \mathrm{U} = 0$, and can therefore be written in terms of spherical harmonics (Hofmann-Wellenhof & Moritz, 2005; Scheeres, 2012b). By applying a series expansion in Legendre polynomials to the $\frac{1}{|\mathrm{r-s}|}$ term, the potential in Equation (4) for an arbitrary mass distribution such as a NEO, expressed using spherical harmonics, is then given by Equation (5) (Montenbruck & Gill, 2000). A detailed derivation of the gravitational potential for an arbitrary mass distribution as defined by Equation (5) can be found in most celestial mechanics and physical geodesy textbooks and is not provided here.

$$
\begin{aligned}
U = \frac{\mu}{r} \sum_{n=0}^{\infty} \sum_{m=0}^{n} \Bigg\{ &\left\{ \left(\frac{\mathrm{R_{CB}}}{r}\right)^n P_{nm}(sin\theta)\cos(m\lambda) \right\} C_{nm} \\
&+ \left\{ \left(\frac{\mathrm{R_{CB}}}{r}\right)^n P_{nm}(sin\theta)\sin(m\lambda) \right\} S_{nm} \Bigg\}
\end{aligned} \tag{5}
$$

The coordinates r, θ, and λ in Equation (5) are radial distance, latitude, and longitude respectively of the spacecraft in a coordinate system fixed to the object's center of mass. $\mathrm{R_{CB}}$ is the mean radius for the body, and μ is the object's gravitational parameter. The functions P_{nm} are the Associated Legendre polynomials, and C_{nm} and S_{nm} are the gravity coefficients of degree n and order m.

The coefficients C_{nm} and S_{nm} describe the gravity potential's dependence on the object's mass distribution (Montenbruck & Gill, 2000). Provided that the internal mass distribution is known, the unnormalized coefficients can be calculated from Equation (6) and Equation (7) respectively.

$$C_{nm} = \frac{2 - \delta_{0m}}{M_{CB}} \frac{(n-m)!}{(n+m)!} \int \frac{s^n}{R_{CB}^n} P_{nm}\big(\sin(\emptyset')\big)\cos(m\lambda')\rho(s)d^3s \qquad (6)$$

$$S_{nm} = \frac{2 - \delta_{0m}}{M_{CB}} \frac{(n-m)!}{(n+m)!} \int \frac{s^n}{R_{CB}^n} P_{nm}\big(\sin(\emptyset')\big)\sin(m\lambda')\rho(s)d^3s \qquad (7)$$

In the case of earth, the unnormalized gravity coefficients, given by Equation (6) and Equation (7), vary by as much as ten orders of magnitude (Montenbruck & Gill, 2000). Normalizing the coefficients according to the Kalua normalization given by Equation (8), removes this variation (Montenbruck & Gill, 2000).

$$\begin{Bmatrix} \bar{C}_{nm} \\ \bar{S}_{nm} \end{Bmatrix} = \begin{Bmatrix} C_{nm} \\ S_{nm} \end{Bmatrix} \sqrt{\frac{(n+m)!}{(2 - \delta_{0m})(2n+1)(n-m)!}} \qquad (8)$$

The dependence of an object's internal mass distribution on the coefficients C_{nm} and S_{nm} can be seen in Equation (6) and Equation (7). In general however, the mass distribution within an object is not known and therefore the coefficients C_{nm} and S_{nm} cannot be directly determined (Montenbruck & Gill, 2000). Because of this, the coefficients must be estimated using indirect methods such as SST.

A geometric representation of spherical harmonics is helpful in understanding how they apply to the gravitational potential of an object. Such a representation is shown

in Figure 1. Spherical harmonics are divided into three categories: zonal, sectorial, and tesseral. The Legendre functions, P_{nm}, with m equal to 0 are considered the zonal harmonics. The zonal harmonics do not depend on longitude and divide a sphere into latitudinal zones. When n is equal to m, the Legendre functions divide a sphere into positive and negative longitudinal sectors (Hofmann-Wellenhof & Moritz, 2005). Legendre functions with n ≠ m, divide the sphere into alternating positive and negative compartments represented by the red and blue sections in Figure 1.   Scheeres (2012b) has shown that the second degree and order component of a gravity field contribute the most to perturbations resulting from non-spherical bodies.
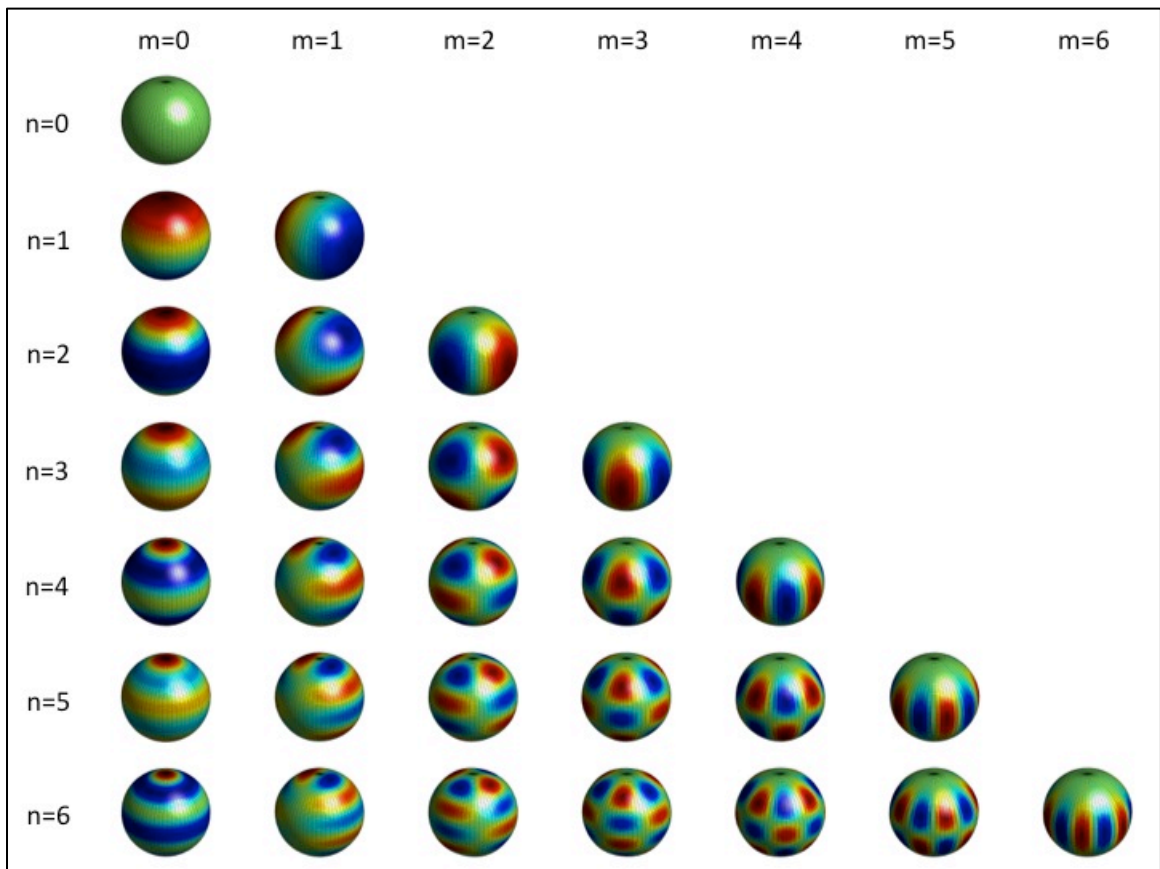
Figure 1. Graphical Representation of Spherical Harmonics

This figure shows a graphical representation of the de-convolution of spherical harmonics up to degree and order 6. Regions colored in red represent areas where the

Legendre polynomial of the same degree and order is positive. Blue regions represent areas where the same Legendre polynomial is negative. The color changes represent the gradient between positive and negative regions. This image is representative of a gravity field where the coefficients are all equal. An actual spherical harmonic representation of a complex gravity field is a combination of these images and will exhibit variations based on the size of each coefficient.

The first spherical harmonic, $n = 0$ and $m = 0$, gives the potential of a point mass and hence its graphical representation in Figure 1 shows no positive or negative regions. Higher order spherical harmonics describe an object's departure from a sphere of uniform density. In order to provide an accurate representation of an object, a sufficiently high degree and order model is desirable since the higher order coefficients more precisely define the object's mass distribution. For example, the EGM96 model of the earth's gravity field is of degree and order 360 (Montenbruck & Gill, 2000).

<div align="center">Internal Structure</div>

Knowledge of the internal structure of asteroids is a crucial component to understanding solar system evolution, human exploration, exploitation of asteroid resources, and threat mitigation. Arguably, the most important of these being for threat mitigation purposes. A NEO's internal structure is an important property that is necessary for understanding how an external force could be used to alter the orbit of the object, should it be on a collision trajectory with the Earth (Binzel et al., 2003). There are many different methods that have been suggested for mitigating a possible asteroid impact with the earth and in each scenario the structure of the asteroid plays a major role in how effective the method would be.

The following section will provide a synopsis regarding the fundamentals of asteroid internal structure. It is not intended to be a comprehensive examination of the topic, but rather it serves to provide a basic understanding of the principles and to

illustrate the capabilities and limitations of current ground-based techniques used to observe NEOs and characterize their internal structure.

While an understanding of the internal structure of NEOs has numerous applications, it is a topic in which we have comparatively little understanding relative to the number of known NEOs. For instance, Carry (2012) has compiled mass estimates for 267 small bodies. This means that less than 3% of all known asteroids and comets have mass and density estimates. The internal structure of an asteroid is characterized by several properties including mass, volume, density, and porosity. There are other properties such as the orientation of the object's spin-axis and rate of rotation that place limits on an asteroids structure and are consequential in observing an asteroid as well as estimating volume. The following section focuses on defining these properties and relationships between each of them.

<center>Density and Porosity</center>

Density can qualitatively be defined as mass per unit volume. In the case of asteroids, density may refer to either the grain density of the object or its bulk density. In both cases, these characteristics refer to the mass per unit volume of the object in slightly different ways. The grain density of an asteroid does not include any voids within the object. Rather, it only considers the mass and volume occupied by the constituent material. That is, it is the spatial volume occupied by the material the object is comprised of and not the volume occupied by the extended object. Bulk density on the other hand, takes into account the entire volume occupied by the object including internal voids. This means that two NEOs may have roughly the same grain density, but significantly different bulk densities.

<center>18</center>

The ratio of grain density to bulk density yields the object's porosity or the percentage of the object that is occupied by empty space (Britt, Yeomans, Housen, & Consolmagno, 2002). Porosity, like density can be described in two different ways, macroporosity and microporosity. Macroporosity describes the large-scale features of an NEO, while microporosity refers to features on a scale of only a few micrometers (Britt et al., 2002). Typically, microporosity is studied in meteorites found on earth and not their parent bodies. For ground-based and in situ studies of asteroids, macroporosity is the characteristic being examined and provides a description of the object's internal structure.

Classifications have been defined, which aid in describing the overall structure of NEOs. These classifications consist of monoliths, aggregates, primitive aggregates, fractured bodies, shattered bodies, rubble piles, coherent rubble piles, thermally modified primitive aggregates, and lithified primitive aggregates (Binzel et al., 2003; Binzel & Kofman, 2005). Specific details regarding these classifications are beyond the scope of this thesis, however, a brief description is provided below for the major types including monoliths, aggregates, and rubble piles.

Monoliths are bodies having strength roughly equal to their tensile strength. These are generally intact bodies with significant cohesion. Aggregates including primitive, fractured, and shattered aggregates are less cohesive than monoliths and are comprised of distinctive structural units. The extent of cohesion depends on the specific type of aggregate and serves as a distinction between the different types. Primitive aggregates have cohesive boundaries that are the result of primordial formation, fractured aggregates show evidence of collisional fracturing, and shattered aggregates have undergone fracturing to the extent where the internal structure of the object is disrupted

(Binzel & Kofman, 2005). In general, the structure and shape of fractured bodies remains intact while that of shattered bodies has been modified (Binzel et al., 2003). Rubble piles are basically completely shattered bodies that have been reassembled by self-gravity.

From these basic descriptions, it is clear that the internal structure of NEOs can vary significantly. However, classifying an NEO based on its structure requires knowledge of the properties previously discussed. Because density and in turn, porosity, are dependent on the mass and volume of the object, both of these properties must be determined with sufficient accuracy before the internal structure can be constrained. The following section discusses some of the current ground-base techniques that can be used to investigate these properties.

Ground-Based Studies

Before addressing the need for in situ studies of NEO, it is prudent to understand the capabilities and limitations that exist with ground-based equipment. The following discussion will be limited to the ground-based techniques that are used to examine the properties necessary to characterize an NEO's internal structure. Specifically, the next two sections will address means by which the mass and volume of NEOs can be established using ground-based observations.

Mass Estimation

Traditionally, the mass of an asteroid has been determined by observing gravitational perturbations with other solar system bodies. Several methods have been developed for this and are extensively discussed in the literature (Kochetova, 2004; Michalak, 2000; Somenzi et al., 2010). The three main methods for this are to observe

orbit deflections during close planetary encounters, planetary ephemeris, and motion of natural satellites (Carry, 2012). The uncertainty associated with each technique is directly related to the size of the object. Masses can be determined to within a few percent for the most massive asteroids; however, accuracy decreases dramatically with size and nearly a third of the published estimates have an uncertainty that exceeds 100% of the estimated mass (Carry, 2012).

The close planetary encounters and planetary ephemeris techniques rely on detecting perturbations resulting from an NEO's interaction with other, generally more massive, solar system bodies. The discovery of satellites around NEOs has significantly increased the number of NEOs that can be studied using mutual perturbations (Binzel & Kofman, 2005). In the case of these binary NEO systems, mutual perturbations between the two NEOs, which compose the system, can be used for mass estimates. This method is the second most accurate method presently available for determining asteroid masses and the most accurate of the ground-based methods with accuracies of a few percent being achievable with this technique (Carry, 2012). The limitation here however, is that not all NEOs are binary systems. At the time of this writing there are roughly 46 confirmed binary or ternary, near-earth asteroids (Benner, 2013b).

Somenzi et al. (2010) discusses how Mars Global Surveyor (MGS) and Mars Express (MEX) have been used for precisely determining the Martian ephemeris. During a close encounter with Mars, an asteroid will slightly perturb Mars' orbit. With the accurate knowledge of Mars' ephemeris, these perturbations can be measured and the mass of the perturbing body can be estimated. One constraint imposed by this method is that data show that perturbations caused by asteroids Ceres and Vesta are nearly

continuous. Perturbations caused by smaller asteroids can be distinguished provided their magnitude is greater than the uncertainties for the perturbations of Ceres and Vesta (Somenzi et al., 2010).

<div align="center">Volume Estimation</div>

Characterization of an NEO's internal structure is highly dependent on its macroporosity. In order to determine this, the object's volume must also be determined. Typically shape models are used for this. The three-dimensional shape of the object permits a numerical estimate of the object's volume to be established. Generally, shape models only include large-scale topographic features and are primarily representative of the general shape of the object. These models can be derived using a variety of techniques including radar delay Doppler echoes, light curves, stellar occultation, thermal radiometry, disk-resolving images, and interferometry (Carry, 2012; Koschny, Drolshagen, & Bobrinsky, 2010). There are however, limitations to these techniques that inhibit their application to small NEO. These limitations are discussed below.

Techniques for determining the size and volume of an asteroid have varying degrees of accuracy and limitations. With current ground-based equipment, NEOs having angular sizes greater than 0.10" can be accurately measured (Carry et al., 2012). Therefore, there is a lower limit on the size of NEOs that can be measured based on the distance to them. As the distance from earth increases, this lower limit on the size of the object increases.

There are presently only two stations capable of using radar delay Doppler echoes to observe NEO; the Arecibo antenna in Puerto-Rico; and the Goldstone antenna in the United States (Koschny et al., 2010). A major limitation to using this type of observation

to accurately determine size and shape is that the target must be within a few million kilometers of earth (Koschny et al., 2010). These close flybys must occur for the signal to noise ratio to be high enough to provide detailed information (Scheeres, 2012b). Given this constraint, the number of NEO that can be observed using Doppler radar is severely limited.

Stellar occultation is more capable of resolving small NEO but it requires observation of at least three events each by multiple observers and the events are infrequent (Carry et al., 2012). This technique is exceptionally accurate at establishing a 2-dimensional projection of the object's 3-dimensional shape. It also has the advantage that small telescopes can be used.

Benner (2013a) has compiled the existing 3D shape models for approximately 43 NEOs, out of the more than 10,000 known. With shape models for less than 1% of the known NEO population, our knowledge regarding the internal structure of these objects is sparse.

There have been several studies conducted, which focus on several properties of interest for NEO (Busch et al., 2006; Busch et al., 2007; Busch et al., 2008; De Luise et al., 2007; Dotto, Barucci, Binzel, & Delbó, 2005; Kohout et al., 2011; Koschny et al., 2010). Each of these papers present results from ground-based observations of NEOs. Carry (2012) provides a compilation of 994 published mass, volume, density, and porosity estimates for 287 small bodies. In addition, 1454 diameter estimates, made using a variety of techniques, have also been published (Carry, 2012).

The techniques discussed above are primarily focused on larger asteroids and as Figure 2 illustrates, determining the shapes and consequently, the volumes for objects

smaller than a few kilometers is limited using current ground-based technology.

However, while these techniques, are limited by resolution and range, the primary barrier

to estimating density is determination of the object's mass (Carry, 2012).
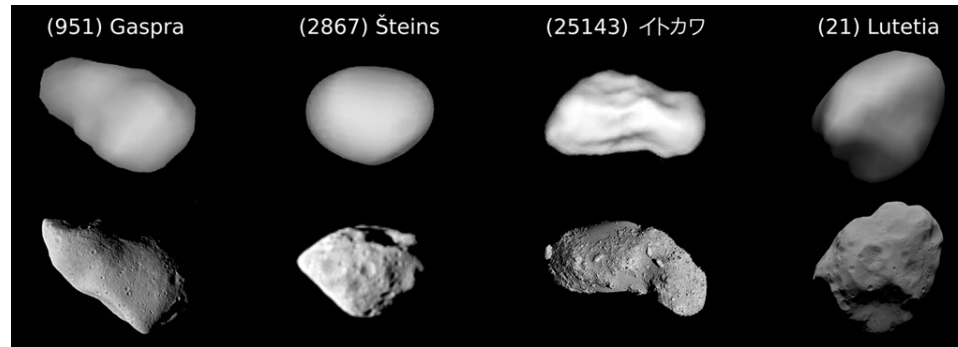
Figure 2: Shape Model Comparison

Shape models derived using technique KOALA are compared to images acquired the ESA's Rosetta mission at (21) Lutetia (Carry et al., 2012). This figure illustrates the limitations of ground-based observations compared to those of in situ observation. Reprinted from "Shape modeling technique KOALA validated by ESA Rosetta at (21) Lutetia,"by B. Carry, et. al, Planetary and Space Science, 66, p. 200-212. Copyright 2012 by Elsevier. Reprinted with permission.

Spacecraft Observations

An alternative to ground-based studies is to use spacecraft to perform in situ

observations of NEOs. As Figure 2 shows, in situ observations offer a significant

improvement over ground-based methods in terms of the level of detail attainable. More

accurate estimates of mass, shape, and volume are possible through in situ observations.

Increasing the accuracy of each of these, in turn increases the accuracy of density and

porosity estimates. To date, there have only been a few spacecraft missions that have

visited NEO and even fewer have been dedicated to the study of asteroid. These include

the NEAR-Shoemaker to asteroid 433-Eros, the DAWN mission to asteroids Vesta and

Ceres, Hayabusa to asteroid Itokawa.

The subsequent discussion focuses on the NEAR-Shoemaker and Hayabusa missions and discusses some of the mission aspects related to characterizing the internal structure of the respective targets. In particular, consideration is given to techniques used for determining mass, shape, gravity model, and ultimately constraining the internal structure for the target of each mission.

NEAR-Shoemaker

The NEAR (Near Earth Asteroid Rendezvous) mission was launched in February 17, 1996. The mission was the first planetary mission dedicated solely to the exploration of an asteroid (Cheng et al., 2002). On February 12, 2001 the spacecraft ended its 5-year mission by becoming the first spacecraft to land on an asteroid when it landed on the surface of asteroid 433 Eros. Upon successfully rendezvousing with Eros on February 14, 2000, the spacecraft was renamed NEAR-Shoemaker in honor of Eugene Shoemaker (1928-1997) (Cheng et al., 2002).

Just over a year after its launch, the NEAR spacecraft made a flyby of asteroid 253 Mathilde. On its closest approach to Mathilde, NEAR flew within 1212 km of the asteroid (Cheng, 2002). Following a thruster misfire to rendezvous with Eros, NEAR made an unplanned flyby of 433 Eros on December 23, 1998. The spacecraft entered orbit around the asteroid on February 14, 2000.

The NEAR mission was the first dedicated mission to study an asteroid. The spacecraft carried six scientific instruments including a Multispectral Imager (MSI), Near-Infrared Spectrometer (NIS), X-ray Spectrometer (XRS), Gamma-ray Spectrometer (GRS), Near Laser Rangefinder (NLR), and a Magnetometer. In addition to the science data gathered using these instruments, radio science experiments were also performed.

These were used to map the asteroid's gravity field. The NEAR-Eros-earth system essentially created a high-low SST scenario where earth served as the high spacecraft tracking a low spacecraft, NEAR. Doppler tracking of the spacecraft from earth-ground stations was used to track subtle variations in the spacecraft's orbit about Eros. The goal was to isolate the perturbations caused by the variations in the object's mass distribution. The gravity model that was produced using these data, enabled scientists to place constraints on the object's density and internal structure.

NEAR Science

While NEAR-Shoemaker carried six scientific instruments only those pertaining to the gravity model and internal structure will be discussed here. These include the MSI and NLR. Additionally, the spacecraft's telemetry, tracking, and control (TTC) subsystem was used to perform radio science experiments. Data from these three systems were used to construct shape and gravity models for Eros as well as make inferences on its internal structure.

Spacecraft guidance and navigation or the Orbit Determination and Control Subsystem (ODCS) measures and maintains the position of the spacecraft's center of mass (Wertz & Larson, 1999). This system is used to determine the spacecraft's position and velocity as a function of time. The tracking data is generated as part of ground communications with the spacecraft, which are handled by the TTC subsystem. The tracking data compiled on the ground is then processed using specialized orbit determination software (ODP) to generate a definitive orbit for the spacecraft. Orbit determination is the best estimate of the spacecraft's previous position (Wertz & Larson,

1999). The gravity model generated for Eros was a direct consequence of this type of orbit determination process (Miller et al., 2002).

In addition to providing communications and data transfer functions between ground stations and the various subsystems and payload elements onboard, modulated code or tones are included on the uplink signal to the spacecraft. These signals are received by the spacecraft and retransmitted back to the ground station. The turn-around time required is a measure of the distance to the spacecraft. When the signal is two-way coherent, the Doppler shift in the signal can be measured providing information on the LOS range rate (Wertz & Larson, 1999). The system onboard NEAR-Shoemaker used two-way X-band Doppler tracking and NASA's Deep Space Network (DSN) with an uplink frequency of 7.2 GHz and a downlink frequency of 8.4 GHz and two-way ranging (Cheng, 2002; Konopliv et al., 2002). The system was used to measure the LOS velocity with a noise level corresponding to approximately 0.03 mm/s (Miller et al., 2002). In order to determine NEAR's position relative to Eros additional data were required. These data came from the MSI in the form of photographs of landmarks on the surface of Eros. The photographs were used to provide two angle measurements relative to Eros and when combined with the Doppler range measurements the resulting orbit accuracy was within a few meters in all directions (Konopliv et al., 2002).

The spacecraft tracking data generated from the systems described above was used to generate a gravity model for Eros. The orbit perturbations observed were dependent on the distance between NEAR and Eros. While in orbit around Eros, NEAR-Shoemaker's orbit varied from several hundred kilometers from the asteroid to as few as 3-km. Tracking data was sampled on 60s intervals resulting in 317,600 measurements

(Konopliv et al., 2002). Table 1 provides a summary of the orbits occupied by the NEAR-

Shoemaker spacecraft while in orbit around 433 Eros.

Table 1. NEAR-Shoemaker Orbits around 433-Eros

This table shows data from the NEAR-Shoemaker orbits around asteroid 433-Eros over the course of 1-year. These data were originally presented by (Konopliv et al., 2002) and (Miller et al., 2002).

Segment	Start Date Time (UTC)	Length (Days)	Orbit (km x km)	Period (Days)	Inclination Eros Equator (°)
1	2/14/00 15:33	10.1	366 x 324	21.8	35
2	2/24/00 17:00	8.1	365 x204	16.5	34
3	3/3/00 18:00	29.3	209 x 200	10.0	38
4	4/2/00 02:03	9.8	210 x 100	6.6	56
5	4/11/00 21:20	10.8	101 x 99	3.4	60
6	4/22/00 17:50	8.0	101 x 50	2.2	65
7	4/30/00 16:15	68.1	52 x 49	1.2	90
8	7/7/00 18:00	6.3	51 x 35	1.0	90
9	7/14/00 03:00	10.6	40 x 35	0.7	90
10	7/24/00 17:00	7.1	56 x 36	1.0	90
11	7/31/00 20:00	8.2	52 x 49	1.2	90
12	8/8/00 23:25	18.0	52 x 49	1.2	105
13	8/26/00 23:25	10.0	102 x 49	2.3	113
14	9/5/00 23:00	37.3	103 x 100	3.5	115
15	10/13/00 05:45	7.6	98 x 50	2.2	131
16	10/20/00 21:40	5.0	52 x 50	1.2	133
17	10/25/00 22:10	0.8	64 x 19	0.7	135
18	10/26/00 17:40	7.4	203 x 64	5.3	144
19	11/03/00 03:00	34.5	197 x 194	10.0	147
20	12/07/00 15:20	6.2	193 x 34	4.2	178
21	12/13/00 20:15	41.8	38 x 34	0.7	178
22	1/25/01 16:05	3.4	36 x 22	0.6	178
23	1/28/01 01:25	0.7	37 x 20	0.6	179
24	1/28/01 18:05	4.6	36 x 35	0.7	179
25	2/02/01 08:51	4.4	36 x 35	0.7	179
26	2/06/01 17:45	5.9	36 x 35	0.7	179

The gravity model established for Eros based on the NEAR-Shoemaker data was determined up to degree and order 15, using 10-days of navigation data, acquired primarily from the 35 km orbit (Miller et al., 2002). This consisted of 74,180 range measurements with an RMS accuracy of 30 cm; however, calibration biases yielded an actual accuracy of approximately 3 m (Konopliv et al., 2002).

The radio science experiments alone were not sufficient to make inferences regarding Eros' internal structure. These conclusions required additional knowledge about the shape of the object. This information came from the shape model that was generated for the asteroid using data from the MSI and NLR. The MSI covered a spectral range of 0.4 to 1.1 μm and produce images 537 x 244 pixels (Cheng, 2002). The NLR was used to collect data on the surface topography of Eros. These data were subsequently used to construct a shape model of the asteroid with a horizontal resolution of roughly 400 m.

During the 1998 flyby, data was collected and combined with ground-based measurements to produce a priori parameter estimates, which were then used as part of the orbit determination strategy after NEAR rendezvoused with Eros (Miller et al., 2002). The orbit determination strategy combined Doppler measurements and optical data with the a priori estimates to generate the gravity model for Eros. Additionally, a gravity model was also produced solely from the shape model by assuming a constant density for the asteroid. This model was compared to the model generated from the orbit determination process as a means to quantify how Eros' internal structure deviates from that of a homogeneous body. Close agreement was found between the gravity coefficients determined from spacecraft dynamics and from those obtained by integrating

the shape model. This led to the conclusion that Eros has a nearly uniform density to within 1% (Miller et al., 2002). Variations in the gravity field were attributed to variations in the regolith and/or internal density (Miller et al., 2002).

Hayabusa

The Hayabusa mission to asteroid 25143 Itokawa was the first sample return mission to an asteroid (Kawaguchi, Fujiwara, & Uesugi, 2008). The Japanese Aerospace Exploration Agency (JAXA) launched the mission on May 9, 2003. During its close approach with earth in 2001, ground based photometry and spectrophotometry was used to characterize the surface composition and taxonomic class of Itokawa (Lederer et al., 2005). At the same time, radar observations were used to estimate its shape and rotation state (Ostro et al., 2004). Despite these observations, prior to Hayabusa's launch, relatively little was known about Itokawa (Kawaguchi et al., 2008).

The Hayabusa spacecraft arrived at its target on September 12, 2005. Upon arrival, the spacecraft did not enter orbit around Itokawa because of its size and low gravity. Instead the spacecraft hovered near one of two points along a line between the earth and Itokawa (Gaskell et al., 2006). The mission served to demonstrate several technologies not previously used for a space mission. The four key technologies were the use of ion engines as the primary propulsion system, autonomous guidance and navigation using optical data, sample collection in a low gravity environment, and reentry from an interplanetary trajectory and sample return (Kawaguchi et al., 2008). During its relatively short stay in the vicinity of Itokawa, the Hayabusa spacecraft made several approaches to the asteroid in preparation for the two touchdowns, which occurred on November 20 and 26 (Gaskell et al., 2006).

Hayabusa Science

The instrument payload onboard the Hayabusa spacecraft included a telescopic imaging camera (AMICA), a near-infrared spectrometer (NIRS), a laser range finder (LIDAR), and an x-ray fluorescence spectrometer (XRS) (Fujiwara et al., 2006). In addition to its onboard instrumentation, Hayabusa also carried a micro rover dubbed, MINERVA (micro/nano experimental robot vehicle for asteroid). The rover was intended to land on the surface of Itokawa, which however, was ultimately unsuccessful (Gaskell et al., 2006).

One of the key technologies that the Hayabusa spacecraft demonstrated was its autonomous navigation system. As this thesis will show, autonomous navigation will prove to be a critical requirement for any rendezvous mission with a small NEO. In the case of Itokawa, its small size and consequentially low gravity, result in an escape velocity of at its surface of less than 10 cm/s. This velocity is such that a person on the surface of Itokawa could escape the asteroid's gravity simply but jumping off of its surface. Escape velocity decreases as the distance from the object's center of mass increases. As a result of this, small fluctuations in Hayabusa's ion engines had a significant impact on the orbit determination solutions and the thrust from these engines was never negligible (Kawaguchi et al., 2008). In order to deal with this situation, an autonomous navigation and control system was required. The system employed autonomous optical navigation and control system by using a combination of stereographic images and LIDAR (Light Detection and Ranging). The stereographic images coupled with the range measurements from the LIDAR created three-dimensional landmark maps, which where then used to determine the position and orientation of the

spacecraft relative to Itokawa as well as estimate the rotational properties of the target

(Gaskell et al., 2006).

The Hayabusa spacecraft was not able to obtain sufficiently accurate

measurements from Itokawa's gravity field to estimate its internal density distribution

(Scheeres, 2012b). However, several estimations of Itokawa's mass were made

throughout the duration of the mission. These attempts are summarized in Table 2.

Itokawa's volume was found to be 1.78×10^{-2} km^3 using the detailed shape models

obtained during the Hayabusa mission (Scheeres et al., 2006). Combining these mass and

volume estimates, the bulk density was found to be 1.9 g/cm^3 ± 9% (Mukai et al., 2007).

While the gravity field was not directly mapped during the Hayabusa mission, the highly

accurate shape model acquired during the mission along with the assumption of a

constant density of 1.98 g/cm^3 were subsequently used to model the gravity field

(Scheeres et al., 2006).

Table 2. Itokawa Mass Estimates

This table provides a summary of the mass estimates and associated uncertainties made for Itokawa. These data were presented in (Fujiwara et al., 2006).

Method	Mass	Uncertainty
Range, Doppler, & LIDAR	3.43×10^{10} kg	±5%
LIDAR & Navigation Data	3.58×10^{10} kg	±5%
LIDAR & Navigation Data	3.54×10^{10} kg	±6%
Range and Doppler Data	3.51×10^{10} kg	±15%
Mean	**3.51×10^{10} kg**	-

The uncertainty in many of the values presented in Table 2 result from the effects

caused by solar radiation pressure being greater than the effects of Itokawa's gravity and

the use of thrusters to control altitude following a reaction wheel failure (Fujiwara et al.,

2006). The uncertainties caused by the seemingly magnified effects of SRP should be expected for any mission to a small NEO. The challenges presented by this type of dynamical environment required the use of new autonomous techniques for navigation and attitude control. The Hayabusa spacecraft demonstrated that these challenges are not insurmountable.

CHAPTER III.

METHODOLOGY

As Chapter II showed, there are substantial limitations to using ground-based observations to characterize small NEOs. NEOs on the order of 500 m or less must have a relatively close approach with earth before physical characteristic data can be collected (Scheeres, 2012b). Chapter II also discusses, that an alternative to ground-based observations is to use in situ observations from an orbiting spacecraft or close flyby. With regard to internal structure and gravity mapping, placing spacecraft in orbit around the NEO is optimal. However, the dynamical environment around small bodies poses significant challenges related to spacecraft operations around them. Communication delays and environment conditions create a scenario where autonomous control will be a requirement as it was for the Hayabusa mission. In order to implement autonomous control, the challenges associated with close proximity operations and their impact on data collection must be well understood. The goal of this research is to assess these conditions as they relate to the use of SST and establish a set of requirements that can be used as the basis for further investigations into characterizing the object's internal structure. The methodology by which these requirements were derived is as follows:

1. Analyze previously flown gravity mapping missions that employed SST;

2. Develop an STK environment for a small NEO;

3. Search orbital parameter space for stable orbits suitable for SST data collection;

4. Investigate the longevity of these stable orbit;

5. Simulate range and range-rate data based for these stable orbits;

6. Compare simulated range and range-rates with the measurement capabilities of GRACE and GRAIL to determine payload requirements; and

7. Establish orbital and maneuvering requirements.

In order to establish a baseline for assessing the feasibility of measuring range and range-rate between two spacecraft in orbit around a small NEO, the concept of SST and two previously flown SST missions were examined. The missions examined were the GRACE mission and the GRAIL mission. The GRACE mission, which at the time of this writing remains operational, uses SST to map the earth's time varying gravity field. The GRAIL mission mapped the lunar gravity field during its roughly 1-year mission.

The systems analysis conducted for this segment of the research, evaluated the technique of low-low SST and its application on the GRACE and GRAIL missions. For each mission, the payload elements and techniques used to measure range and range-rate were investigated. Emphasis was placed on the measurement capabilities and resolutions attainable when measuring the range and range-rate between spacecraft. Because the payload elements being considered have proven flight heritage their measurement capabilities were used to create the standard to which the simulated data would be compared. Additionally, the orbital parameters for each mission were noted for comparison to those utilized in the STK simulation. This comparison would assess any possible scaling between missions.

An STK simulation was used to simulate an SST mission around a small NEO. This type of environment does not exist natively within STK and therefore had to be

developed. The requirements for creating this environment within STK were determined.

Asteroid 25143 Itokawa was used as the basis for creating a model for the small NEO.

This asteroid was chosen because it is roughly 500 m in diameter and the relevant data

exists for creating the STK environment. The data required to create the STK simulation

were obtained from a variety of published sources.   These data were subsequently used

to generate the STK files required to create the dynamical environment within STK. This

environment included the features natively available within STK such as SRP, drag, and

third-body gravity as well as those specific to Itokawa such as the asteroid's shape,

gravity field, and ephemeris. Once these files were included in the appropriate STK

install directory, asteroid 25143 Itokawa was available as a central body around which a

variety of scenarios could be created.   For each of the scenarios used for this work the

simulation time was set such that Itokawa was near perihelion. This created a "worst

case" scenario in terms of perturbations caused by solar radiation pressure.

After the STK environment was created, a scenario was established to explore

orbital parameter space for stable orbits suitable for collecting SST data. First, the effects

of semi-major axis on orbit stability were examined over a 30-day window, surrounding

perihelion. These data were used to establish a range of values, which result in the most

stable trajectories.

Once a suitable range of semi-major axes was established, the stability with

respect to right ascension of the ascending node (RAAN) was examined in 30º

increments for the upper and lower limits of the range or semi-major axis value. This

analysis was used to investigate the longevity of orbit stability. The resulting 24

trajectories were used to examine orbit stability with respect to inclination. The time

required for the inclination to exceed ±5º from the initial conditions was reported for each orbit. An analysis of these times was used to establish an SST data collection window for the upper and lower limits of the semi-major axis range.

After the data collection window was established based on the above method, 24 additional spacecraft were introduced into the STK scenario. Each spacecraft was paired with one of the existing spacecraft thereby creating 24 pair. Additional simulations were conducted to simulate an SST mission for each pair. These simulations were used to generate simulated tracking data between each spacecraft pair over the previously established data collection window.

The simulated SST data generated for each pair of spacecraft was used to evaluate the measurement precision that would be required during an actual SST mission around a small NEO. The simulated range and range-rate data was compared to the data obtained from the systems analysis with respect to the measurement capabilities. This comparison was used to determine if the measurements anticipated from an actual SST mission around a small NEO would be discernable based on a standard set by proven technology.

To establish a preliminary set of orbit requirements, the orbital parameters used for the STK simulations were compared to those used by the GRACE and GRAIL missions. The potential for directly scaling the mission requirements based on the central body size was also considered. The frequency of orbital correction maneuvers was determined based on the data collection windows established from the STK simulations and the subsequent variations observed in the simulated SST data.

CHAPTER IV.

SYSTEMS ANALYSIS

Radio Science

The use of spacecraft tracking as a method to map the earth's gravity field has been used since the first satellites were launched during the late 1950's (Colombo, 1984). The early methods relied on optical or radar tracking techniques and the resulting gravity models only revealed large-scale features. However, as more and more spacecraft were launched, data and the models generated from them only improved. Tracking data from the Apollo program's lunar orbiter was even used to map the Moon's gravity field. Today, our ability to track spacecraft has improved significantly and the techniques no longer rely on optical or radar data. Instead, Doppler shifts in carrier signals included in radio communications with the spacecraft are used. These investigations, which are generally referred to as radio science investigations can be used to study a variety of topics including planetary atmospheres and gravity fields.

In most cases, scientific investigations rely on payload elements designed for a specific purpose. For example, a spectrometer may be used to determine surface compositions or a laser range finder may be used to measure surface topography. While these instruments are not necessarily limited to a single function they are included to support a specific mission objective or objectives. Radio science, however, relies on the spacecraft's telemetry, tracking, and command subsystem, which serve as the interface between the spacecraft and ground stations (Wertz & Larson, 1999). Communications

between the spacecraft and the ground stations are in the form of radio signals transmitted between the spacecraft and NASA's Deep Space Network (DSN). Planetary atmospheres, natural satellites, and gravitational fields directly affect the radio signals transmitted between a spacecraft and the DSN. By observing the resulting attenuation, scintillation, refraction, rotation, or Doppler shifts caused by interaction with any of these, scientists are able to glean information regarding properties such as the composition or structure of subject being investigated (Doody, 2001).

The use of radio science to map the gravity field of a small NEO is the subject of interest here. As previously mentioned, the gravity field of an object can subsequently be used to infer information about its internal structure. As a spacecraft orbits the NEO, variations in the mass distribution within the object cause perturbations to the spacecraft's orbit. These perturbations result in small accelerations experienced by the craft, which consequently produce Doppler shifts in the radio transmissions between the spacecraft and DSN. In addition to the spacecraft's orbital motion, there are additional factors that can result in changes in the craft's motion. These must be removed from the data either through measurement or modeling. Some of the forces that can act on the spacecraft that must be accounted for include solar radiation pressure and atmospheric drag in the case of most planetary orbits. Once the Doppler shifts caused by these have been removed, the remaining Doppler shifts represent the motion cause by the variations in gravity.

For what is generally referred to as high-low SST, the measurements are between the earth and a single spacecraft. These measurements are made along the LOS between the two entities and are not a direct measurement of the spacecraft's motion with respect

to the object. Therefore, the motion of the object, which the spacecraft is orbiting, must be removed along with motion associated with its nominal orbit (Doody, 2001). The NEAR-Shoemaker demonstrated this technique of tracking a single spacecraft to map asteroid 433 Eros' gravity field, which is discussed in Chapter II.

The process of high-low SST may use earth or another spacecraft occupying a higher orbit to track the lower altitude spacecraft whether it is in earth-orbit or in orbit about another body. This is not necessarily the most efficient method to achieve global coverage. In the case of earth, an orbiting spacecraft is only visible to a single ground station for a limited amount of time during each orbit. If a global picture is required, the tracking data must be continuous as the spacecraft orbits the object. Longer data arcs are possible from a single ground station if the spacecraft is placed in a higher altitude orbit. However, since the force of gravity is a function of distance, the resolution is better when the spacecraft being tracked is in a lower orbit. This contradictory situation can be remedied if the spacecraft is tracked using another spacecraft. One option is to place one spacecraft in a low orbit and the other in a higher orbit. The higher orbit spacecraft tracks the perturbations to the orbit of the lower spacecraft. This technique allows the spacecraft being tracked to occupy a lower altitude orbit but the length of the data arcs are still limited due to the difference in orbital velocities.

An alternative proposed as early as 1969 by Wolf is referred to as low-low SST (Colombo, 1984). However, it took more than 30-years before the method was actually implemented. In the early part of this century, low-low SST was attempted for the first time using a pair of spacecraft placed in LEO. This mission is known as the GRACE mission, which at the time of this writing remains operational. The technique has since

been employed to map the lunar gravity field. To date, however, this type of SST has not been attempted around a small body. More specifically, it has not been investigated around an object roughly 500 m in diameter.

As the above discussion alludes to, low-low SST uses two spacecraft in roughly the same orbit to track one another's motion. Similar to other tracking techniques, low-low SST uses radio science techniques to track the motion of each spacecraft. With this method however, the LOS range and range-rate between two spacecraft is measured independent of the reference frame defining the positions of the two spacecraft relative to the central body. This is because the LOS measurements do not represent the position or velocity of either spacecraft but rather the projection of these vectors onto a line joining the two craft. These relative changes are related back to the motion of each spacecraft relative to the object being orbited and can ultimately be used to produce a map of the object's gravitational field.

GRACE

The Gravity Recovery and Climate Experiment spacecraft were launched in 2002. This mission uses two identical spacecraft to map both the long-term and time varying components of the Earth's gravity field. One of the main objectives of the mission is to study the time varying gravity field in-order to gain a better understanding of ocean currents, ground water storage, ice buildup at the poles, sea level changes (Tapley, Bettadpur, Ries, Thompson, & Watkins, 2004). Changes such as polar ice melting produce changes in the Earth's mass distribution, which results in changes in the Earth's gravity field.

As the two spacecraft orbit the Earth, the leading spacecraft "sees" changes in the Earth's mass distribution before the trailing spacecraft. The variances in the gravity field caused by these mass variations result in changes in the relative separation of the two craft, which are tracked using the global positioning system (GPS) and the K/Ka band ranging system (KBR).

The two spacecraft, GRACE-A and GRACE-B, are in coplanar, near-polar orbits at an altitude of approximately 450 km. The separation distance between the two spacecraft is nominally 200 km. GPS is used to obtain precise orbit determination for each spacecraft. The relative separation between the two spacecraft is tracked using the KBR. An oscillator generates the frequency for the KBR. In addition to the KBR, each spacecraft is equipped with a superstar accelerometer, GPS receiver and processor, star camera assembly, and a coarse Earth and Sun sensor (GRACE fact sheet.2003).

The accuracy of the KBR system is limited primarily by the stability of the oscillator used to generate the frequency. The oscillator aboard the GRACE spacecraft is considered an ultra stable oscillator. However, even with this oscillator, there are still uncertainties in the measurement due to noise errors. In-order to reduce these errors GRACE uses a dual one-way ranging (DOWR) method (Kim & Lee, 2009). GRACE is the first mission to employ such a technique. With DOWR, a carrier phase is transmitted by the KBR onboard each spacecraft. The phase measured at the receiver on the second spacecraft is the difference between the phase received by one spacecraft and the reference phase of the other, including the oscillator phase noise. Summing these measured phases the phase noise effectively cancels, assuming it is constant over the time of flight. The DOWR technique used in the GRACE mission is capable of measuring

separation changes between the two spacecraft to 10μm and velocity changes to 10μm/sec.

An additional source of error for GRACE is due to non-gravitational forces acting on the spacecraft. Because the two spacecraft are at such a low altitude, atmospheric drag and both solar and earth radiation pressure are substantial contributors to the non-gravitational accelerations seen by each craft (Flury, Bettadpur, & Tapley, 2008). To account for these perturbations each spacecraft is equipped with precision three-axis accelerometers. These accelerometers are accurate to 10^{-10} m/s^2/√Hz. Without the accelerometers to quantify the effects of the non-gravitational forces, the certainty in range and range rate measurements would be lower.

In addition to the external forces measured by the accelerometers, subsystems onboard each spacecraft have been found to make unexpected contributions to the accelerometer measurements. Flury et al. (2008) addresses the internal sources of error in the accelerometer data. The attitude and pointing requirements for the KBR onboard each spacecraft are maintained using cold gas thrusters. These thrusters are fired around 600 times per day. When the thrusters fire, they produce acceleration spikes in the data. Additionally, electrical currents can generate acceleration spikes when internal systems such as heaters, turn on and off (Flury et al., 2008).

The orbit properties of the GRACE spacecraft and the relationship between them are also of interest. Figure 3 plots the inclination and eccentricity for the GRACE-B satellite from 2002 until February 23, 2014. This plot shows both long and short wavelength oscillations in the satellite's inclination and only short wavelength oscillations in its eccentricity.
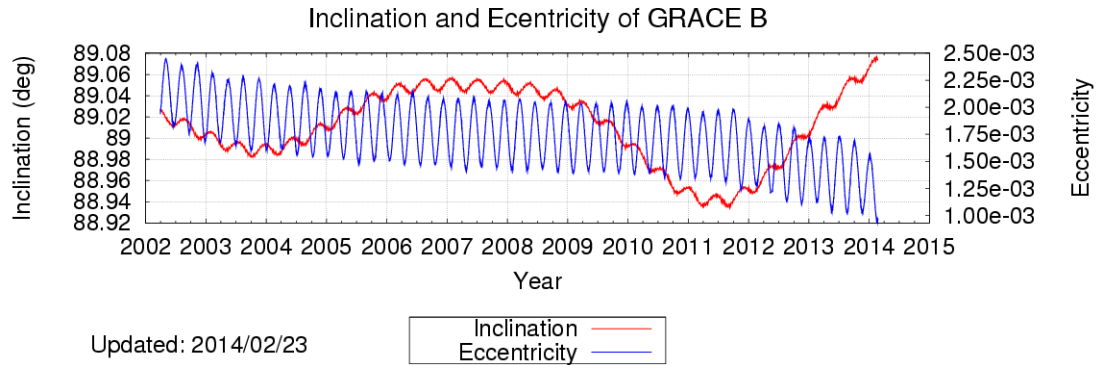
Figure 3. GRACE B Inclination and Eccentricity

This figure plots the inclination and eccentricity for the GRACE B satellite from 2002 through February 23, 2014. The inclination varies between 88.92° and 89.08° with the period of long-wavelength oscillations on the order of 8 years and the period of short wavelength oscillations closer to 0.5 years. The eccentricity ranges between 2.5 × 10⁻³ and 1.0 × 10⁻³ and oscillates with a period of approximately 0.25 years.   There does not appear to be any long-wavelength oscillations in eccentricity. Reprinted from GRACE Orbital Configuration, in GRACE: Gravity Recovery and Climate Experiment, n.d., Retrieved February 23, 2014, from http://www.csr.utexas.edu/grace/operations/configuration.html. Reprinted with permission.

Figure 4 shows a plot of the difference in inclinations of the two GRACE

spacecraft. The differences in inclinations are small on the order of 10^{-4} to 10^{-5} degrees.
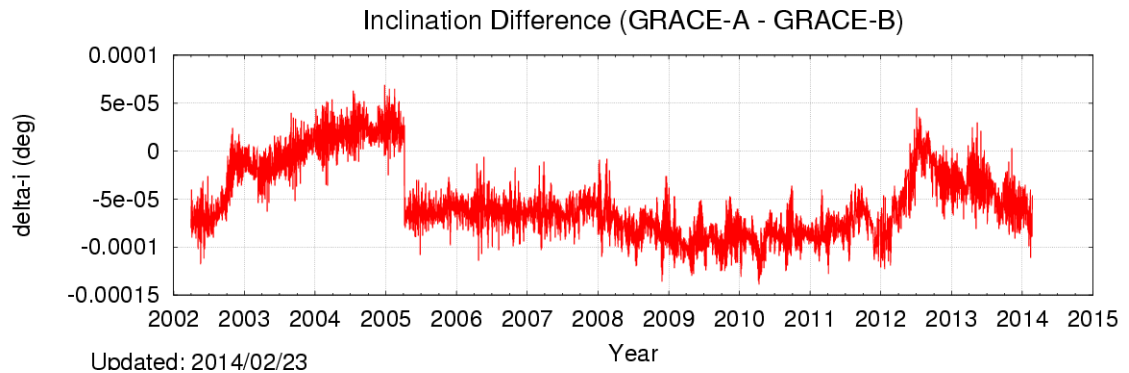
Figure 4. Inclination Difference Between GRACE A and GRACE B

This figure plots the inclination difference between the GRACE A and GRACE B spacecraft from 2002 through February 23, 2014. The difference in inclination ranges from -0.00015° to 0.00005°. Reprinted from GRACE Orbital Configuration, in GRACE: Gravity Recovery and Climate Experiment, n.d., Retrieved February 23, 2014, from

The difference between the semi-major axis of each spacecraft fluctuates by ±20 km with the exception of two spikes as shown in Figure 5. The data show several step changes in the inclination differences opposed to the typical periodic drift seen in the majority of the data. These sharp changes are due the result of spacecraft maneuvers (GRACE orbital configuration.2010).
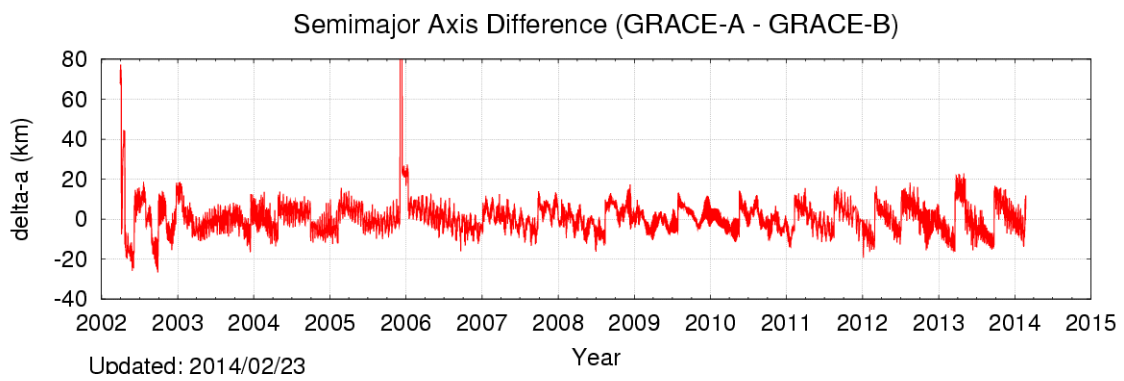
Figure 5. Semi-major Axis Difference Between GRACE A and GRACE B

This figure shows the difference between the semi-major axis of each satellite between 2002 and February 23, 2014. With the exception of two spikes, the average variance near 0 km and the step changes are the result of orbit maneuvers. Reprinted from GRACE Orbital Configuration, in GRACE: Gravity Recovery and Climate Experiment, n.d., Retrieved February 23, 2014, from http://www.csr.utexas.edu/grace/operations/configuration.html. Reprinted with permission.

GRAIL

The Gravity Recovery and Interior Laboratory mission was launched in September of 2011. The mission ended on December 17, 2012 when the spacecraft intentionally impacted the surface of the Moon. This mission's objectives were to study the interior and thermal evolution of the Moon by precisely mapping its gravity field (Lockheed Martin, 2011). The GRAIL mission, similar to the highly successful GRACE mission, was a low-low SST mission. However, while the underlying principals of the

two missions are similar, there are several significant differences in their execution

mainly due to their respective targets. Table 1 in Asmar et al. (2013) details the

differences between the two missions.

Modeling the lunar gravity field began as early as the 1960's during the Apollo

program. These efforts were limited by the technology of the time with the S-band

Doppler having an accuracy of only a few mm/s compared to better than 1.0 μm/s for

GRAIL (Lemoine et al., 2013). GRAIL used two nearly identical spacecraft to map the

lunar gravity field and was originally designed resolve mass variations down to 30 km at

the 0.5 mgal level (Enzer, Wang, & Klipstein, 2010). The two of spacecraft were placed

into near circular, near polar lunar orbits with a mean altitude of 55 km. While the

overall orbital inclinations of each spacecraft varied 2.4°, the variance between the two

inclinations was less than 0.0001° (Konopliv et al., 2013).   Table 3 summarizes the

variation in inclination, eccentricity, and inter-satellite range during the primary mission.

The data in Table 3 was compiled from Konopliv (2013).

Table 3. GRAIL Mission Parameters

This table presents select mission and orbital parameters for the GRAIL spacecraft
during the mission lifetime.

Parameter	Value
Orbit Inclination	89.2° ±1.2°
Eccentricity	0.0 – 0.02
Inter-Satellite Range	80 km – 220 km

To map the lunar gravity field with the desired accuracy, both the relative changes

in the separation and velocity of the two spacecraft must be measured as well as their

positions with respect to the Moon. The relative separation and velocity measurements

are along the LOS between the two spacecraft. With the GRACE mission, the positions

of the spacecraft were tracked using the GPS. Unlike GRACE however, the GRAIL spacecraft did not have access to the GPS. Therefore, another method was required to provide timing and tracking information. For this purpose, GRAIL used a 2 GHz s-band timing transfer system. This system was used to provide the difference in clock measurements and an 8 GHz x-band signal was used for Doppler tracking of each spacecraft. Coupled with NASA's deep space network (DSN), these two systems were used for orbit and timing determination for each spacecraft.   Similar techniques are used for interplanetary spacecraft missions.

The relative motion of each spacecraft, including position and velocity, was determined using a 32 GHz ranging signal transmitted between the two spacecraft. Similar to GRACE, a DOWR technique was applied to remove clock or oscillator noise. For the GRAIL mission the 32 GHz signals are transmitted using slightly different frequencies. This allowed phase changes on the order of 10^{-4} cycles to be detected. The pre-launch noise requirements on the system were such that relative velocities of ranging between 0.4μm/s and 1.0μm/s could be resolved (Konopliv et al., 2013). The actual performance realized by the Ka-band system was 10 times better than these requirements with a noise of 0.03μm/s (Konopliv et al., 2013).

The GRAIL mission did not include accelerometers for measuring the non-conservative forces acting upon the spacecraft. The primary sources of non-gravitational accelerations are solar radiation pressure and gravitational influence from other solar system bodies. Because there is no atmosphere around the Moon, drag was not a problem for GRAIL. Even though they were not directly measured, these effects still had

to be accounted for. It was assumed that these forces were small enough that they could be modeled rather than directly measured, as is the case with the data analysis to date.

Range and range-rate data was collected between 1 March 2012, 16:30:35 and 29 May 2012, 17:07:30, and returned more than 99.99% of the possible data (Lemoine et al., 2013). These data have been used to produce several lunar gravity models. Zuber (2013) developed a gravity model to degree and order 420 representing a resolution of 13 km. This is more than twice the original requirement of 30 km. Additional models have been developed independently by NASA's JPL and GSFC. These models, to degree and order 420, 540, and 660 are presented in Konopliv et al. (2013) and Lemoine et al. (2013). Each of the resulting models is significantly better than the original mission requirement to produce models of degree and order 180.

CHAPTER V

STK SIMULATION

Using Analytical Graphics software package STK, a scenario was developed to simulate spacecraft operations around a small NEO and generate SST data. This simulation incorporates a small NEO as the central body. The properties of asteroid Itokawa were used to create the target central body. This included the asteroid's gravity coefficients, its overall dimensions, rotation rate, and ephemeris. The currently accepted values for each of these properties were obtained from several sources, which are discussed further below. The effects of solar radiation pressure and third body gravitational perturbations were also incorporated into the STK simulation.

Central Body Creation

While STK offers a planetary data supplement that allows the user to select from several different central bodies, those available for selection consist of the planets, several moons, and the largest asteroid Ceres. Each of the included objects however, exceeds the 500 m size limit by at least an order of magnitude. Therefore, a smaller central body had to be modeled within STK for this work. The software includes provisions for generating such a model. The user defines the properties necessary for STK to represent the object's orbit around the Sun (or another solar system object if desired), its rotation rate and axis orientation, mass, gravitational parameter, spherical harmonic gravity model, and approximate shape. Additional properties for the central body may also be modeled such as terrain features and physical structures. These

additional capabilities were not used for this work and consequently will not be discussed here.

The model for each central body consists of a series of files that govern the various properties for the object. The number of individual files required varies depending on the object properties that are included in the model. In general, a central body model requires at a minimum, a central body file and a gravity model. The central body file is the main file that governs the object's properties in STK. This file contains information about the object such as its gravitational parameter, its shape, size, and the available propagators (J2, Two-Body, Astrogator, HPOP, etc.). It also points to any additional files referenced by the model including gravity models, rotation models, and ephemeris data.

The model developed for this simulation was based on the asteroid 25143 Itokawa. It employed the files necessary to generate Itokawa's gravity field to degree and order 12, its rotation, including axis orientation, and its orbit around the Sun. The specific files used are provided in the Appendix.

The degree and order 12, gravity model for Itokawa was provided courtesy of Daniel Scheeres (personal communication, June 5, 2013). This model was based on data obtained during the Hayabusa mission along with the assumption that the asteroid has uniform density. The ephemeris for Itokawa was generated using the NASA Jet Propulsion Laboratory (JPL) HORIZONS computation system. The system was accessed using JPL's telnet interface via "telnet horizons.jpl.nasa.gov 6775". Ephemeris data was calculated beginning on January 01, 2000 through January 01, 2101. The rotation model comprised data from two sources. The orientation of Itokawa's axis of rotation was

obtained from (Demura et al., 2006) while its rotation rate was obtained from the JPL

Horizons ephemeris file. Table 4 provides a summary of the rotation data used.

Table 4. Itokawa Attitude Data

This table presents the data used to model Itokawa's rotation within the STK simulation.

Property	Value(s)
Julian Date of J2000 Epoch	2453137.5
Pole Orientation Relative to Ecliptic	$\alpha = 90.54°$ Right Ascension, $\delta = -66.3°$ Declination
Rotation Rate	$\dot{w} = 12.132$ Hrs (712.16 deg/day)

The orientation of a central body's axis of rotation as defined within STK is shown in

Figure 6.
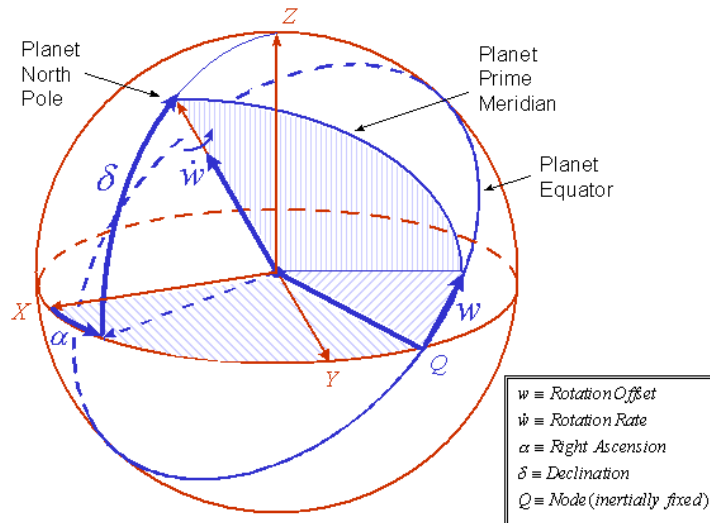
Figure 6. Pole Orientation

This figure shows the orientation of a central body's axis of rotation as it is defined in STK. STK image courtesy of Analytical Graphics, Inc.(AGI). Reprinted from, n.d., Retrieved March 19, 2014 https://www.agi.com/resources/help/online/stk/source/extfile/gator/images/ra_dec.gif. Reprinted with permission

Coordinate Systems

In STK, there are several options available for coordinate system reference frames. These options include fixed, inertial, mean of date, true of date, true of epoch, J2000, ICRF. The inertial reference frame was chosen for these simulations because it is a constant rotation from the International Celestial Reference Frame (ICRF) such that the z-axis aligned with Itokawa's axis of rotational. In the Itokawa inertial frame, the z-axis is aligned with Itokawa's axis of rotation and Itokawa's equatorial plane is located in the x-y plane. This simplified defining initial conditions for generating satellite trajectories.

The ICRF is defined by the International Astronomical Union (IAU) (STK 10.1 central body coordinate systems.2014). While celestial reference frames have been in use throughout history, they have primarily been based on the measured positions of stars.

The relatively close proximity of these stars results in a perceivable motion. This motion

means that any reference frame derived using this method will be time-dependent. The

development of very long baseline interferometry (VLBI) significantly improved

positional accuracies permitting measurements to the sub-milliarcsecond level (Ma et al.,

1998). The improved accuracy enabled the definition of non-stellar reference frames.

One such frame of reference is the ICRF, which is constructed using the positions of

extragalactic radio sources. These sources are at such great distances that they exhibit

little or no perceivable motion and therefore the ICRF is considered to be quasi-inertial

(Ma et al., 1998). The ICRF is an improvement over its predecessor, the J2000 reference

frame. While these two frames are very similar, the J2000 frame rotates slowly with

respect to the ICRF.

The ICRF has its origin at the barycenter of the solar system and is sometimes

referred to as the BCRF (STK 10.1 central body coordinate systems.2014). However,

STK does not restrict the origin for the ICRF to the barycenter. Instead the origin for the

ICRF used within STK may be the center of mass for the central body, in this case,

Itokawa. The reference frame is however, still considered quasi-inertial because the axes

defining it are aligned, in Euclidean space, with those of the more traditional ICRF (or

BCRF). Therefore, there is no loss of accuracy by translating the origin from the

barycenter to the Itokawa's center of mass.

Orbit Propagation

The next component to the development of the STK simulation was the selection

of an orbit propagation method. The orbit propagator is used to evaluate the equations of

motion for a satellite and predict its position at future times based on a set of initial

conditions. There are several options available for orbit propagation within STK including 2-Body, J2 Perturbation, J4 Perturbation, High Precision, Astrogator, and STK External. The 2-Body propagator only accounts for the force of gravity resulting from the central body, which is modeled as a point mass. The J2 and J4 propagators account for the first and second order secular variations respectively in the spherical harmonic expansion of gravity. These propagators do not account for external perturbation effects. The high precision propagator uses numerical integration techniques to integrate the equations of motion for the spacecraft. External perturbing forces can be accounted for using this method. Astrogator employs the high precision propagator and adds the ability to model trajectories and maneuvers. External propagators in STK rely on user defined file sets that may be numerical, analytic, or semi-analytic.

The simulation developed for this work made use of the high precision propagator. This choice allowed for the execution of detailed simulations, by including third-body gravitational effects and solar radiation pressure. It also permits simpler migration to the Astrogator propagator, which will allow development of a more detailed asteroid rendezvous mission simulation. This could incorporate all segments of the mission including launch, rendezvous, and orbit correcting maneuvers, as well as data collection, and even communications.

High Precision Orbit Propagation

STK's High Precision Orbit Propagator (HPOP) was used to integrate the equations of motion for the simulated spacecraft. The HPOP within STK uses one of several numerical integration techniques to integrate the equations of motion for a spacecraft. The force model uses a spherical harmonic representation of the gravity field

and can account for numerous external forces resulting from atmospheric drag, solar radiation, and third body gravitational effects. Use of the HPOP for orbit propagation is valid provided that the spacecraft's orbit does not penetrate a circumscribing sphere around the central body. If this condition is violated, the spherical harmonic representation of the gravity field is no longer valid because the resulting gravitational potential function no longer converges.

Using the HPOP within STK requires several inputs and permits the inclusion of additional properties if desired. Each of these is described below. The required definitions include the initial conditions for the spacecraft, propagation window, step size, coordinate system, force model, and the desired integration technique. Optional properties include solar radiation pressure, atmospheric drag, tides, and central body radiation pressure from both reflected and thermal photons.

<div align="center">Numerical Integration</div>

Four different numerical integration methods are available for use within STK. These methods include fourth order Runge-Kutta (RK-4), Runge-Kutta-Fehlberg with 7th or 8th order error control (RKF7/8), Bulirsch Stoer, and Gauss Jackson (GJ). The integration step size for each of these methods may be set to either a fixed interval or may use relative error to control the step size. Fixed step sizes remain constant during the orbit integration while using relative error determines the integration step size based on a user defined error tolerance. With step sizes based on relative error, the step size will vary based on the error associated with the integration.

There are three different interpolation methods that may be used. These methods include variation of parameters (VOP), Lagrange, and Hermitian. The main differences

between interpolation schemes is that VOP is better suited to integrations with large step sizes, Lagrange interpolates position and velocity separately, and Hermitian interpolates position and velocity together (STK 10.1 integrator.2014).

The ephemeris may be reported on either a fixed or variable time step. When using a fixed time step, the ephemeris will be reported at equal time intervals regardless of whether or not the integrator can adjust the step size. When the time step is not fixed, the ephemeris reporting times will be determined by integration step size.

Lastly, the minimum altitude to which the orbit may be propagated can also be defined. If the orbit drops below this altitude at any point, the integration will terminate.

Analytical Graphics published results from an integration comparison test (STK 10.1 integrator.2014). A subset of these results is presented in Table 5. The comparison tests were conducted by generating a reference orbit with a 10-second time step using the Runge-Kutta-Fehlberg 7/8 integrator and relative error control. Additional trajectories were then generated with varying combinations of integrators and force models. These were then compared to the reference orbit and the maximum difference in position was recorded.

Table 5. Comparison of Data from Integration Tests

This table presents a subset of the results from AGI's comparison of integration methods (STK 10.1 integrator.2014). The results presented focus on the Runge-Kutta-Fehlberg and Bulirsch Stoer methods and include the solar radiation pressure force model and a model including all of the available forces.

Integrator	Force Model	VOP	Time Regularization	12	13	14	15	16
RKF7/8	SRP	No	No	0.000	0.000	0.000	0.000	0.000
Bulirsch Stoer	SRP	No	No	0.000	0.000	0.000	0.000	0.000
RKF7/8	SRP	No	Yes	0.003	0.000	0.000	0.000	0.000

Table 5 cont.

Integrator	Force Model	VOP	Time Regularization	12	13	14	15	16
Bulirsch Stoer	SRP	No	Yes	0.000	0.000	0.000	0.000	0.002
RKF7/8	SRP	Yes	No	0.000	0.000	0.000	0.000	0.000
Bulirsch Stoer	SRP	Yes	No	0.000	0.000	0.000	0.000	0.035
RKF7/8	SRP	Yes	Yes	0.001	0.000	0.000	0.000	0.000
Bulirsch Stoer	SRP	Yes	Yes	0.000	0.000	0.000	0.000	0.007
RKF7/8	All	No	No	0.000	0.000	0.000	0.000	0.000
Bulirsch Stoer	All	No	No	0.000	0.000	0.000	0.000	0.000
RKF7/8	All	No	Yes	0.004	0.000	0.000	0.000	0.000
Bulirsch Stoer	All	No	Yes	0.000	0.000	0.000	0.001	0.001
RKF7/8	All	Yes	No	0.000	0.000	0.000	0.000	0.000
Bulirsch Stoer	All	Yes	No	0.000	0.000	0.000	0.000	0.001
RKF7/8	All	Yes	Yes	0.009	0.001	0.000	0.000	0.000
Bulirsch Stoer	All	Yes	Yes	0.000	0.000	0.000	0.000	0.000

The results presented in Table 5 indicate that there is little variation between the RKF7/8 and Bulirsch Stoer integration methods. Because the goal of this work was not to determine the most appropriate integration technique to use within STK, additional efforts were not expended to conduct further tests. As a result the RKF7/8 method without VOP or time regularization was used.

Third Body Gravitational Perturbations

STK also has the ability to model the gravitational effects caused by other solar system bodies such as the sun, planets, or minor planets. The objects included in the calculations are specified as part of the force model used by the HPOP. While

accounting for third body perturbations may not be as critical for modeling orbits around more massive bodies, Itokawa's low gravity amplifies the gravitational effects of other solar system objects. Hence, the effects of the sun, major planets, and two minor planets were included in this simulation.

In order to account for the gravitational effects of other solar system bodies, their positions relative to the spacecraft must be accounted for. This is accomplished by including ephemeris data for each object in the simulation. The ephemeris source used for each third body is specified independently and is defined by the central body file, the JPL DE ephemeris, or may be defined by the user. For this simulation, the default central body file and associated ephemeris was chosen for each of the third bodies included. The objects included are listed along with their respective gravitational parameters in Table 6.

Table 6. Third Body Gravitational Parameters

This table presents the objects along with their respective gravitational parameters (μ) used in the simulation to account for third body gravitational perturbations.

3rd Body	Gravitational Parameter (km^3/s^2)
Sun	$1.327122000000 \times 10^{11}$
Earth	$3.986004418000 \times 10^{5}$
Mars	$4.282837190120 \times 10^{4}$
Moon	$4.902801076000 \times 10^{3}$
Jupiter	$1.267127648383 \times 10^{8}$
Venus	$3.248585920790 \times 10^{5}$
Saturn	$3.794058536168 \times 10^{7}$
Mercury	$2.203209000000 \times 10^{4}$
Uranus	$5.794557628118 \times 10^{6}$
Neptune	$6.836534878892 \times 10^{6}$
Ceres	$7.000000000000 \times 10^{1}$
Pluto	$9.769998557980 \times 10^{2}$

Solar Radiation Pressure

Solar radiation pressure (SRP) was also taken into account when using STK's HPOP to model the satellite orbits. In addition to experiencing perturbations caused by third body gravitational forces, a spacecraft will also feel accelerations as the result of photons incident on its surface that are either reflected or absorbed. These reflections or absorptions result in a small, but non-negligible force being applied to the spacecraft.

The force acting on the spacecraft is a function of the surface area of the spacecraft exposed to the radiation and the solar flux at its location in space, and the spacecraft's mass. At a distance of 1 AU, the solar flux is approximately 1367 W/m^2 (Wertz & Larson, 1999). The magnitude of the solar flux is inversely proportional to the square of the distance from the sun.

The simulation accounted for SRP using a spherical, dual cone model within STK. This model accounts for the actual size of the sun and the distance to it. It assumes that the spacecraft is spherical and models each of the three illumination conditions possible for the orbiting craft. While this is not the most accurate nor realistic model it is sufficient for this work. However, a more detailed model based on the actual spacecraft shape will be required for more precise mission design work. The possible conditions for illumination are full exposure, partial exposure (penumbra), and zero exposure (umbra). During each of these conditions, the visible portion of the solar disk is used to calculate the satellite accelerations resulting from SRP (STK 10.1 solar radiation pressure.2014). These accelerations are calculated using Equation (9).

$$\ddot{r}_{SRP} = (\mathrm{K})(\mathrm{C_R})\left(\frac{\mathrm{A_R}}{m}\right)\left(\frac{\mathrm{L_S}}{4\pi cr^2}\right) \qquad (9)$$

In Equation (9), K is the fraction of the solar disk visible to the satellite, $\mathrm{C_R}$ is the

solar radiation pressure coefficient, $\mathrm{A_R}$ is the cross-sectional area of the satellite

presented to the Sun, m is the satellite's mass, $\mathrm{L_S}$ is the solar luminosity, c is the speed of

light, and r is the distance between the satellite and Sun. $\mathrm{C_R}$ is given by $1+\varepsilon$, where ε is

the reflectivity of the spacecraft, which depends on its composition. For a complete

absorption ε is equal to 0 and for specular reflection, ε is equal to 1 (Montenbruck & Gill,

2000). For diffuse reflection, ε is approximately equal to 0.4 (Wertz & Larson, 1999).

The reflectivity and solar radiation pressure coefficient for select spacecraft components

are listed in Table 7. For this work a diffuse reflection model was assumed with ε equal

to 0.4 yielding a solar radiation pressure coefficient of 1.4.

Table 7. Reflectivity and SRP Coefficient

This table presents the reflectivity and solar radiation pressure coefficient for select spacecraft components based on data published in (Montenbruck & Gill, 2000).

Material/Component	Reflectivity (ε)	Solar Radiation Pressure Coefficient ($\mathrm{C_R}$)
Solar Panel	0.21	1.21
High-gain Antenna	0.30	1.30
Aluminum Coated Mylar Solar Sail	0.88	1.88

The area to mass ratio, $\mathrm{A_R}/m$ was assumed to be 0.02 m^2/kg. This assumption was

based on a cross sectional area of 10.0 m^2 presented to the sun and a satellite mass of 500

kg. For comparison, the Hayabusa spacecraft had core dimensions of 1.0 m by 1.1 m by

1.6 m and a full width of 6.0m after deploying the solar panels (Hayabusa-the final

approach.2010). This yields a potential cross-sectional area of 9.6m^2. With a mass of

510kg, Hayabusa's area to mass ratio is 0.0188 m^2/kg.

<center>Spacecraft Orbits</center>

Placing a spacecraft in orbit about a small object presents significant challenges,

the first of which is establishing a bound orbit. Achieving and maintaining a bound orbit

around a small body can prove problematic because of the object's rotation and low mass.

The result is, in general, a strongly perturbed gravitational environment. The low mass

results in a relatively weak force of gravity and low escape velocity. As Chapter II

discusses, the force of gravity between two objects is inversely proportional to the square

of the distance between them. In addition, the mass distribution is rotating. This rotation

results in a rotating gravitational potential. The combination of these effects means that

the spacecraft must orbit in close proximity to the object, as the data presented in the next

chapter will show.

There are also external forces that act upon the spacecraft, which can in some

cases, exceed the gravitational force responsible for binding the spacecraft in orbit around

the object. These forces may result from solar radiation pressure, third body gravitational

forces, and can even come from the spacecraft itself as a result of thrusting maneuvers or

outgassing. For these simulations however, only perturbations resulting from SRP and

major third body gravity contributions are considered.

Orbital dynamics in strongly perturbed environments such as those of NEO have

been studied in great detail and there are a plethora of publications related to the topic

such as (Broschart, 2006; Hamilton & Burns, 1991; Pol', 2011; Scheeres, 2004; Scheeres,

Broschart, Ostro, & Benner, 2004; Scheeres, 2012a; Scheeres, 2012b). These works

<center>61</center>

address the various components associated with orbital dynamics close to asteroids in varying capacities. Work by (Scheeres, 2012b) has shown that retrograde orbits are more stable but result in higher speeds relative to the asteroid's surface and constrains the geometry of the orbit. Dynamically, the simplest orbit to consider is a synchronous one. The ideal synchronous radius can be found from Equation (10).

$$r_{sync} = \left(\frac{\mu T^2}{4\pi^2}\right)^{1/3} \tag{10}$$

Such a synchronous orbit, if stable, would eliminate the effects due to the asteroid's rotation. However, the mass distribution within the asteroid will typically limit the number of truly synchronous orbits (Scheeres, 2004). In most cases the positions for synchronous orbits will be located in the equatorial plane along the object's longest and shortest body axis but each is generally unstable, resulting in escape or impact within a few orbits (Scheeres, 2004). Additionally, such equatorial orbits are not optimal for achieving global coverage of the asteroids gravity field.

The individual factors contributing to the dynamics of a spacecraft's orbit can be modeled independently to achieve an understanding of their respective effects. However, in some cases their combined effects are important (Scheeres, 2004). In the STK simulation the effects of the asteroid's rotation, third-body gravity, and SRP are accounted for simultaneously.

Scenario Epoch

The effects of external forces acting on a spacecraft are largely dependent on the distance between the orbiting spacecraft and the source of perturbation. In the case of third-body gravitational effects and SRP, this distance is directly related to the location of

Itokawa along its orbit. As discussed above, SRP depends on the solar flux at the spacecraft's location. Making the simplifying assumption that the solar output is constant, the contributing factor to solar flux becomes distance. The subsequent analysis was conducted over a period when this distance was near its minimum or when Itokawa was near perihelion. The expected radius of perihelion for Itokawa can be found using Equation (11).

$$r_{Perihelion} = \frac{a(1 - e^2)}{1 + e} \tag{11}$$

To establish the time of perihelion during the STK scenario, a vector pointing in the direction of the Sun was then inserted into the STK simulation with its origin at Itokawa's center of mass. The magnitude of this vector was reported on 10-second intervals over 1 complete orbital period or 1.52 years. The date and time corresponding to the minimum of these data was then used as the date of perihelion.

To confirm the results of the preceding analysis, the distance and date of perihelion were compared to the values published on the JPL solar system dynamics website as of January 22, 2014 at 17:51 UT (JPL small-body database browser.2014). The published time of perihelion is 10 Jul 2013 18:57:11:820, which is within 1 minute of the date and time determined from STK thereby confirming the results from the method used. The perihelion distance found from STK varies by 10^{-5} AU from the published value. This variance translates into a difference of approximately 1496 km or 9.29×10^{-4} % difference between the published value and that obtained from STK. These results are summarized in Table 8. The slight variance in both the time and distance of

perihelion is likely due to using a step size of 10 seconds for the orbit integration in the

STK scenario.

Table 8. Perihelion Data Comparison

The radii of perihelion and aphelion for Itokawa are presented. The values determined directly from the STK simulation are compared to the published values and to those calculated using Equation (11).

Source	Distance (AU)	Date / Time
Equation (11)	0.953106667	N/A
STK	0.953115522	10 Jul 2013 18:56:30:000 UTCG
NASA JPL	0.9531066667849941	10 Jul 2013 18:57:11:820 (2013-Jul-10.77999795)

Each of the simulations discussed in Chapter VI were based on the spacecraft's

equations of motion being integrated over a thirty-one day period surrounding the date of

Itokawa's 2013 perihelion passage. This integration was performed using the RKF7(8)

algorithm with Lagrangian interpolation to degree 7. The error calculations used relative

error with a minimum tolerance of 10^{-13} and steps sizes ranging between 1 sec and 86400

sec.

CHAPTER VI.

STK DATA COLLECTION AND ANALYSIS

The orbital parameters for the GRACE and GRAIL spacecraft varied with time as revealed in Chapter IV. Variations in properties such as the inclination and eccentricity were relatively small while the overall separation of the two spacecraft was permitted to drift by several kilometers. The environment around small asteroids will likely result in more dramatic variations in these parameters, which means there is a high probability of the spacecraft being ejected from the system or impacting the surface of the asteroid. The volatility of the orbital parameters is portrayed in Figure 7, Figure 8, and Figure 9. Figure 7 shows a highly unstable orbit that impacts Itokawa after only 2 orbits. Figure 8 shows a semi-stable orbit that does not impact Itokawa and it is not ejected from the system, however the orbital parameters vary significantly from their initial state. Figure 9 shows a reasonably stable orbit where the orbital parameters remain close to the initial state and the spacecraft does not impact Itokawa and is not ejected from the system.
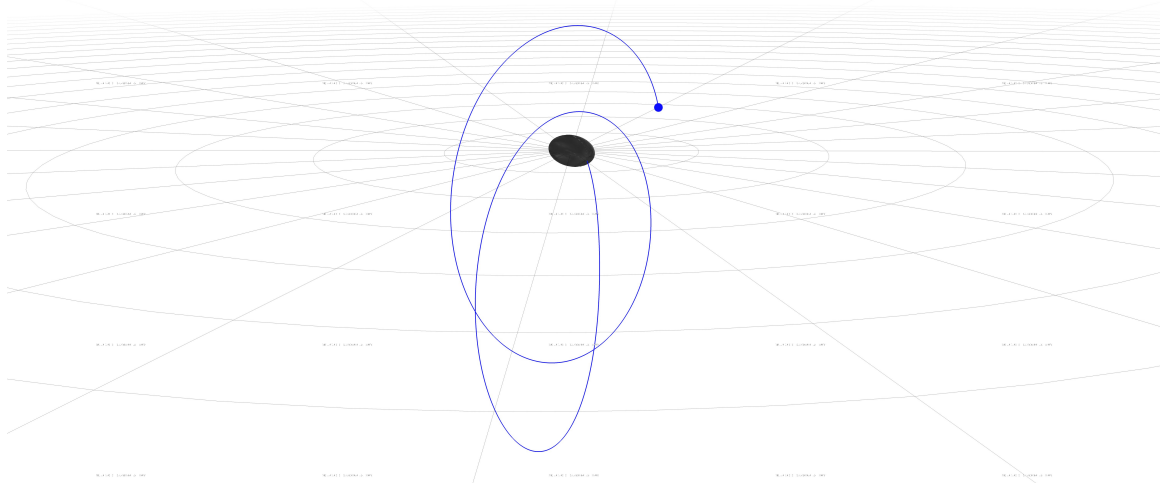
Figure 7: Unstable orbit around Itokawa

This figure shows an example of an unstable orbit around Itokawa. The spacecraft is initially in a circular, near polar orbit with a semi-major axis of 1 km. The trajectory is considered unstable because the spacecraft impacts the asteroid after less than 2 complete orbits.
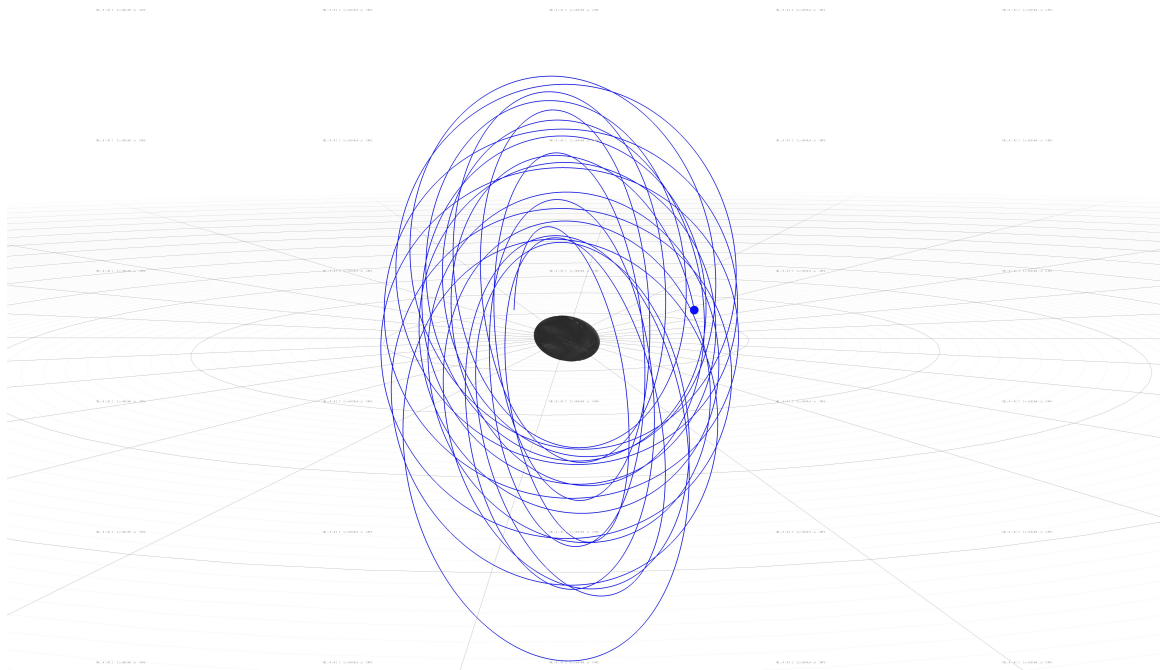

Figure 8: Semi-stable orbit around Itokawa

This figure shows the trajectory of a spacecraft initially in a circular, near polar orbit with a semi-major axis of 1 km. The orbit is propagated using STK for 30 days. The resulting trajectory is considered semi-stable since the spacecraft is not ejected from the system and does not impact the asteroid during the observed time frame. However, the resulting trajectory varies significantly from the initial conditions.
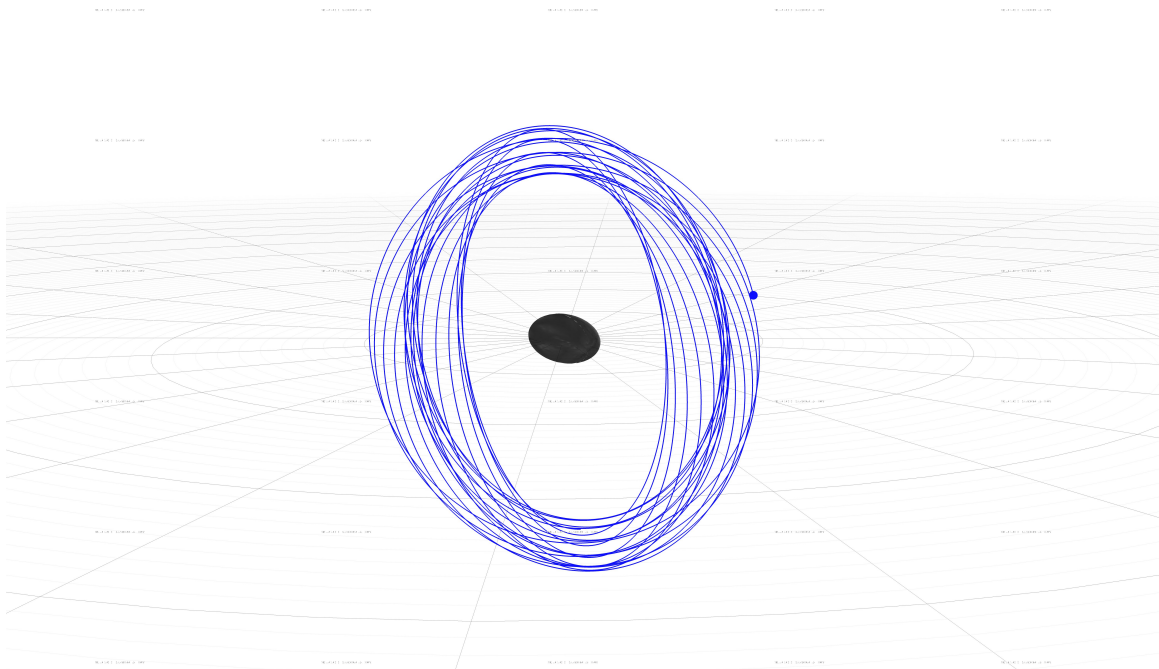

Figure 9: Stable orbit around Itokawa

This figure shows an example of a stable orbit around Itokawa. The spacecraft is initially in a circular, near polar orbit with a semi-major axis of 1 km. The orbit is considered stable since the spacecraft is not ejected from the system and does not impact the asteroid during the observation time frame. Additionally, the orbit does not vary significantly from the initial conditions.

To account for the conditions observed in Figure 7, Figure 8, and Figure 9, and the other challenges associated with spacecraft dynamics around small asteroids, several steps were taken to collect and analyze the simulation data.

Before attempting to collect and analyze the simulated range and range-rate data, the initial conditions for the spacecraft pair had to be established. This required evaluating how variations in the initial conditions affect the spacecraft trajectories. The first step was to determine a range of semi-major axis values to use as the basis for the

subsequent simulations. Once these semi-major axis values were established, they were held constant and orbit stability was further analyzed by varying the initial state of other orbital elements. The resulting data was used to establish a window of stability during which range and range-rate data could be obtained. After establishing a data collection window for the inter-satellite range and range-rate data, additional simulations were executed to simulate the SST tracking data between a pair of spacecraft in a low-low configuration.

The analysis of the STK data was compared to the GRACE and GRAIL missions discussed in Chapter IV. This comparison examined the variations in the orbit properties observed in the GRACE and GRAIL missions and compared them to those observed during the simulations. The simulated range and range-rate data was also examined against the resolving capabilities of the instrumentation used by GRACE and GRAIL to determine if the expected changes in relative position and velocity would be discernable.

Orbit Selection

The first step in selecting the initial conditions that would be used for the range and range-rate simulations was to establish a range of semi-major axis values.   These were then used as the basis for the subsequent analysis. Specifically, the first goal was to determine a range of initial semi-major axes that would result in the most stable orbits for data collection. To do this, the orbits for 7 spacecraft with altitudes ranging from a few tens of meters to nearly 10 km were generated. The semi-major axis values chosen for the initial 7 spacecraft pairs were chosen so that effects of the strongly perturbed orbital environment could be observed over a wide range of values. Several considerations were

made when choosing the upper and lower bounds for the semi-major axes for these 7 spacecraft:

1. The spacecraft must occupy a gravitationally bound orbit;

2. The relative strength of SRP should be minimized compared to the force of gravity;

3. The orbital period should be optimized; and

4. The orbit should not penetrate the circumscribing sphere around Itokawa.

The Hill sphere for an object defines the region around an object where gravitational a bound orbit can exist. The radius of this sphere around Itokawa ranges between 25 km and 45 km (Scheeres et al., 2006). Beyond this radius, bound orbits do not exist, even under ideal conditions. Because the ultimate goal is to map the gravity field for the simulated asteroid, orbital radii as large as the Hill radius are not desirable. As Chapter II discusses, there is an inverse relationship between the gravitational force and distance. This means that there is a significant reduction in the gravitational effects with increasing distance. Neglecting the effects of a non-uniform mass distribution, the gravitational potential at a distance of 25 km from Itokawa is an order of magnitude smaller than it is at 10 km and two orders of magnitude smaller than at a distance of 1 km. Additionally, the effects of SRP become more apparent as distance from the asteroid increases as a result of the lower gravitational force. The combined effect is a rapidly decaying orbit leading to the spacecraft impacting the asteroid's surface or being ejected from the system. It is for these reasons that the maximum semi-major axis value considered here is 10 km.

Conversely, the lower limit on semi-major axis values is the result of two items. The first is that the highest resolution gravity model will be obtained using low, near-polar, circular orbits with a period equal to a whole number of revolutions of the asteroid (Colombo, 1984). Therefore, the ideal orbital radii for SST can be calculated using Equation (12) where n is the number of orbits, T is the orbital period equal to, r is the orbital radius, and μ is the asteroids gravitational parameter. Using Equation (12) the smallest radius that meets these conditions is obtained when n is equal to 1, resulting in a value of 485 m.

$$ r = \sqrt[3]{\frac{nT\mu}{4\pi^2}} \tag{12} $$

The second factor driving the lower limit is the spherical harmonic representation of Itokawa's gravity field used. A spherical harmonic gravity model is only valid for points outside a circumscribing sphere surrounding the object. For this model, this circumscribing sphere has a radius of approximately 278 m. Radii less than this penetrate this imaginary sphere around Itokawa, invalidating both the spherical harmonic gravity model used and the subsequent simulation results. It is for these two reasons that the lower limit considered in this study was chosen to be 400 m.

The initial inclination and eccentricity were chosen such that the resulting orbits would be near-polar and circular thereby meeting the conditions of an ideal SST mission as described by (Colombo, 1984). This created conditions similar to the configurations used by the GRACE and GRAIL missions. However, unlike the GRACE and GRAIL missions' pro-grade, near-polar orbits, these simulations utilized retrograde orbits at 91°.

This deviation was based on work by Scheeres (2004; 2012b), which showed that retrograde orbits tend to be more stable in strongly perturbed environments.

Finally, the remaining elements, including argument of periapsis, RAAN, and true anomaly, were all chosen to be 0°. The rationale behind these choices was in part, arbitrary, but remained constant for each of the 7 orbits. Since the orbits were initially circular, the argument of periapsis is technically, undefined, so a choice of 0° is somewhat inconsequential to the initial conditions. While any initial value for the true anomaly would have been acceptable, a value of 0° places the spacecraft in the x-y plane of the given coordinate system, which for these simulations, coincides with Itokawa's equatorial plane. While the choice of RAAN was also somewhat arbitrary, a value of 0° did however simplify the subsequent analysis. Since the orbits were propagated in the Itokawa inertial reference frame with an initial inclination of 91°, a RAAN near 0° placed the initial orbital plane only 1° out of the x-z plane. If unperturbed, the y-component of the position vector should oscillate uniformly very close to 0 indefinitely. A truly polar orbit with 0° RAAN would reside solely in the x-z plane. If unperturbed, it would remain there indefinitely exhibiting no change in its y-component. However, because perturbations were expected, any deviation in inclination, argument of periapsis, and RAAN manifest as fluctuations of the y-component of each spacecraft's position vector.

The initial conditions chosen based on the above discussion are provided in Table 9.

Table 9. Initial Conditions Used to Generate Preliminary Trajectory Data

The data presented in this table shows the initial conditions used in the STK simulations for each spacecraft. These are given in terms of classical orbital elements in the inertial frame, where a is the semi-major axis in meters, e is the eccentricity, i is the inclination, ω is the argument of periapsis, Ω is the RAAN, and ν is the true anomaly each of which is

given in degrees. The ideal semi-major axis in meters (a_{ideal}) and number of complete orbits (n) as calculated from Equation (12) are also shown.

Spacecraft	a	a_{ideal}	n	e	i	ω	Ω	ν
A1	10000	10025.18955	94	0.00	91.00	0.00	0.00	0.00
B1	5000	4989.036144	33	0.00	91.00	0.00	0.00	0.00
C1	2000	2098.145958	9	0.00	91.00	0.00	0.00	0.00
D1	1000	1008.683369	3	0.00	91.00	0.00	0.00	0.00
E1	750	769.7694789	2	0.00	91.00	0.00	0.00	0.00
F1	500	484.924385	1	0.00	91.00	0.00	0.00	0.00
G1	400	Not Available	<1	0.00	91.00	0.00	0.00	0.00

Using the initial conditions given in Table 9, simulations were performed over a 30-day period surrounding the date of perihelion for Itokawa. Two separate simulations were executed for each of the 7 configurations. The first simulation includes the effects of SRP and while the second neglects them. The purpose for the two simulations was to evaluate the impact of SRP on each spacecraft's orbit and verify that the orbit perturbations observed were in part the result of the gravitational environment and not solely due to SRP. The resulting trajectories are shown in Figure 10 through Figure 23.

Gravitational and non-conservative forces acting upon the spacecraft cause perturbations to the initial orbits defined by Table 9. These perturbations cause changes in the classical orbital elements. Rather than examine these changes directly in the form of classical orbital elements, the position vector for each spacecraft was plotted as a function of time. This permitted a more concise analysis to be conducted since the specific variations are not of interest at this stage. Instead, the overall deviations from the nominal initial state are of interest.

As previously noted, the choice of coordinate system and the initial conditions should result in trajectories that exhibit periodic behavior in the components of the

position vector represented in this system. A plot of the x and z components over time

should oscillate between plus and minus a value close to the initial orbit radius and have a

frequency equal to the period of the orbit. A similar plot would result for the y-

component of the position vector with the exception that the amplitude would be

comparatively small compared to the other two components. This is due to the 1° angle

between the orbital plane and the x-z plane. Perturbations to the spacecraft's trajectory

will manifest as deviations from these uniform oscillations in the form of changes in

frequency, amplitude, or both.

The amplitude of the y-component is dependent on the initial conditions. The

expected absolute value of this amplitude is given in Table 10 for each spacecraft. The

values given in Table 10 were calculated assuming the orbits remain unperturbed. These

values are used as a baseline for gauging deviations in the y-component.

Table 10. Maximum Expected y-Component of the Position Vector

This table presents the maximum expected magnitude of the y-component of the position vector for Satellites A through G in an unperturbed environment. The values were obtained by generating a two-body solution for each satellite.

Satellite	Position Vector Max y-component (m)
SatelliteA	129.994635
SatelliteB	87.26204
SatelliteC	34.90482
SatelliteD	17.452414
SatelliteE	13.089313
SatelliteF	8.726212
SatelliteG	5.123506

Figure 10 and Figure 12 show the position vectors components for satellites A

and B when effects of SRP are neglected. These two plots display the expected behavior

in each of the components. The y-component for SatelliteA exceeds the unperturbed

magnitude of 130 m by several hundred meters while SatelliteB exceeds the unperturbed

magnitude of 87.2 m by approximately 100 m. These excess deviations are attributed to

the gravitational environment around Itokawa.

Figure 11 and Figure 13 plot the position vector components for Satellites A and

B when the effects of SRP are accounted for. These figures clearly show that the

resulting trajectories for both spacecraft are unbound. In each case the expected periodic

behavior is not seen in any of the position vector components, which is commensurate

with an escape trajectory. Since the simulations were performed at perihelion where the

effects of SRP are expected to be greater than they would be if the simulations were

conducted at aphelion, it is conceivable that these orbits could be bound under conditions

where the effects of SRP are reduced. This is supported by the fact, that when SRP is

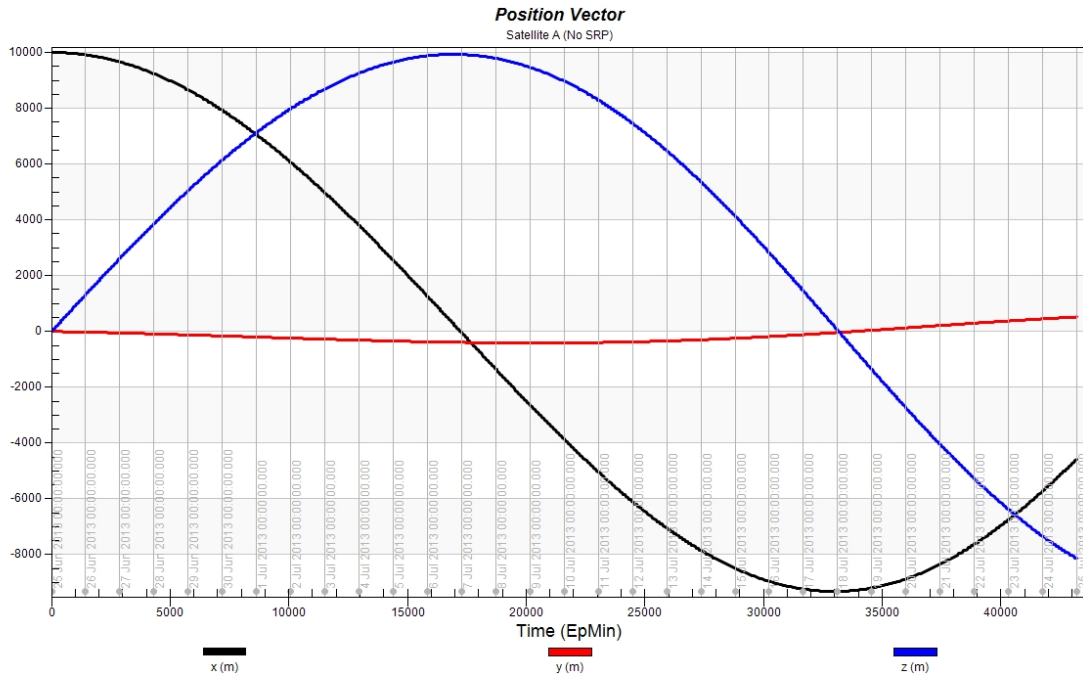neglected, the same initial conditions result in bound orbits.

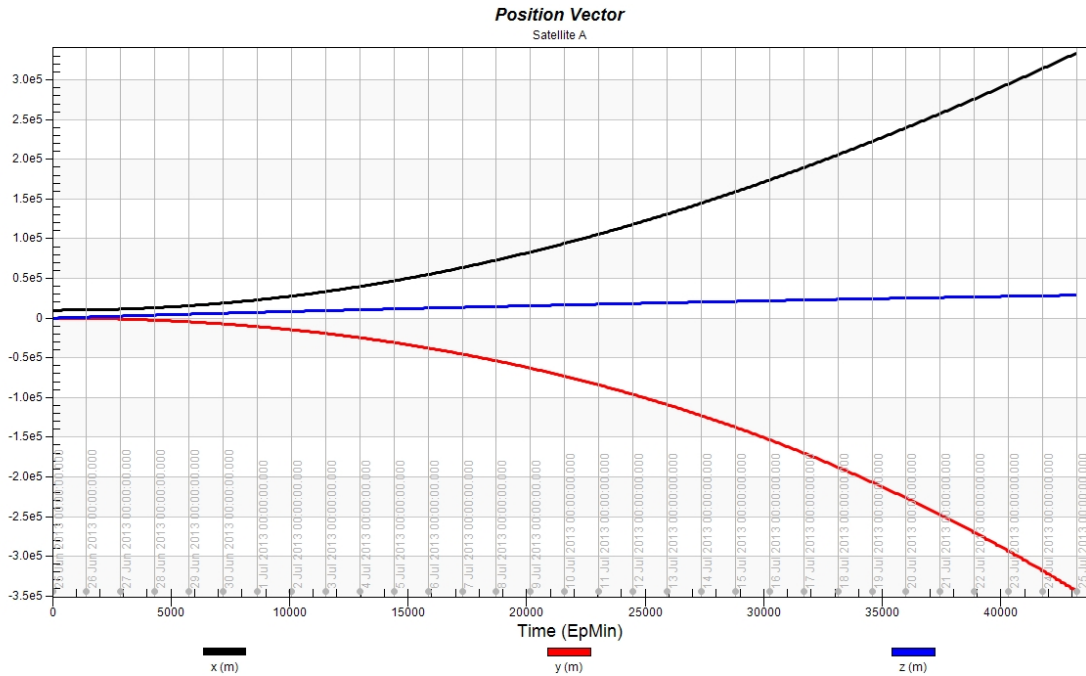Figure 10. Satellite A Position Vector Components Neglecting SRP

This figure shows a plot of the position vector components for Satellite A without including the effects of SRP. The plot shows the expected periodic behavior in both the x and z components while the y-component remains nearly flat. With out SPR, the variations in the y-component can be primarily attributed to the irregular gravitational environment. The 91° inclination only accounts for approximately 175 m of the variation seen in the y-component.

Figure 11. Satellite A Position Vector Components Including SRP

This figure shows a plot of the position vector components for Satellite A including the effects of SRP acting on the spacecraft. The non-periodic behavior of each component indicates that the spacecraft's orbit is not bound to Itokawa. The gravitational attraction of Itokawa at a distance of 10 km is not sufficient to overcome the forces associated with SRP resulting in the spacecraft being ejected from the system.
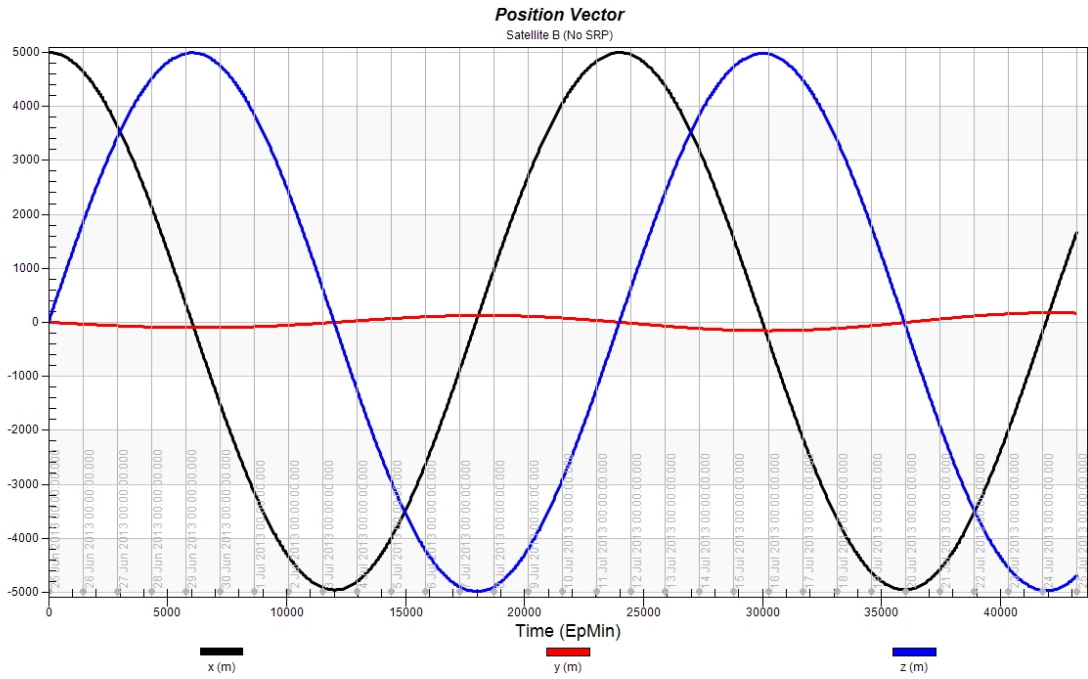
Figure 12. Satellite B Position Vector Components Neglecting SRP

This figure shows a plot of the position vector components for Satellite B without including the effects of SRP. The plot reveals the expected periodic behavior of the x and z-components while the y-component remains nearly flat. The observed variations in the y-component are due to the non-uniform gravitational environment surrounding Itokawa.
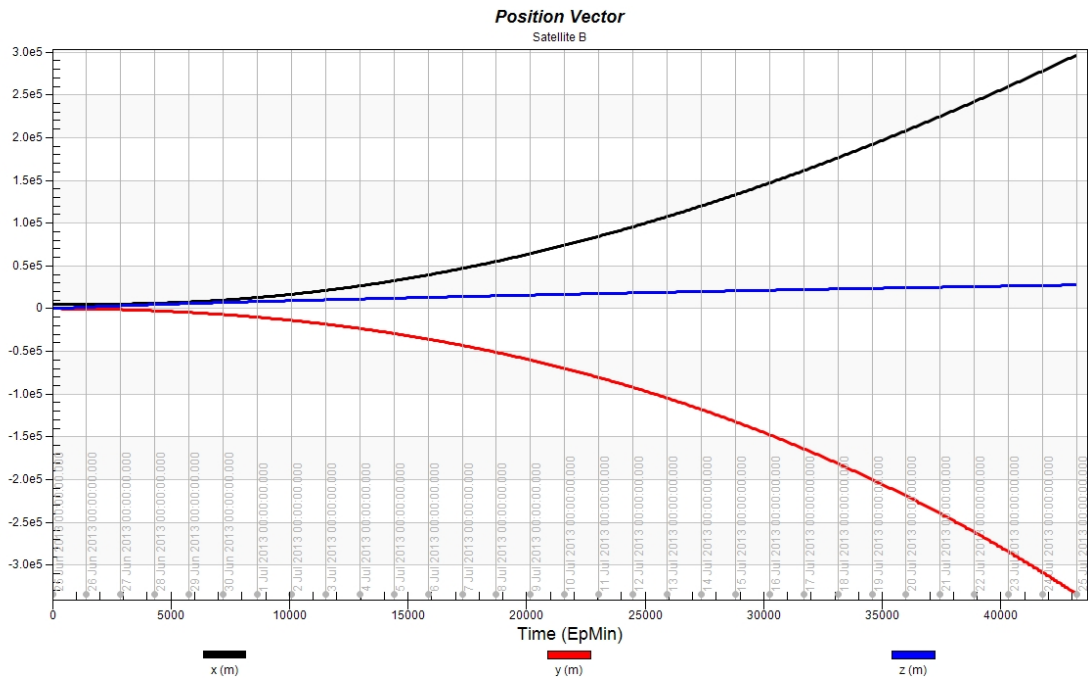

Figure 13. Satellite B Position Vector Components Including SRP

77

This figure shows a plot of the position vector components for Satellite B including the effects of SRP acting on the spacecraft. The non-periodic behavior of each component indicates that the spacecraft's orbit, like that of Spacecraft A, is not bound to Itokawa. The gravitational attraction of Itokawa at a distance of 5 km is not sufficient to overcome the forces associated with SRP resulting in the spacecraft being ejected from the system.

The results for spacecraft C and D are very similar to those obtained from spacecraft A and B. When SRP is neglected, the orbits are periodic as shown in Figure 14 and Figure 16. Unlike spacecraft A and B, however, they are not immediately ejected from the system when SRP is included. This is evident from the periodic behavior during the first 10-days shown in Figure 15 and Figure 17. The window prior to being ejected from orbit increases the potential for collecting usable tracking data using these initial conditions.
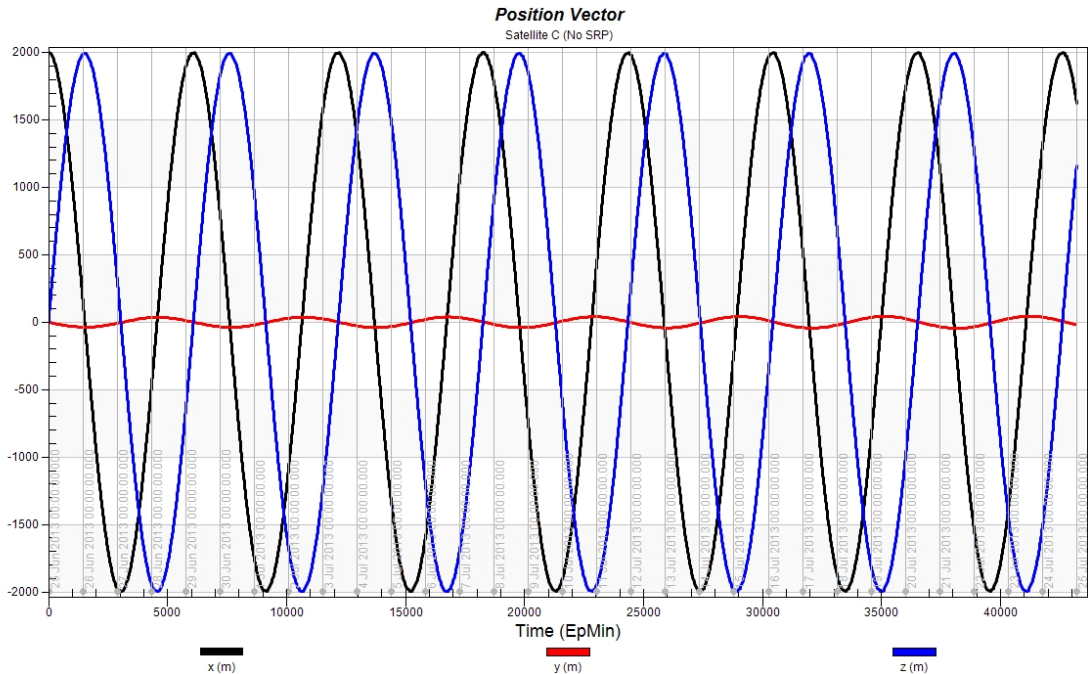
Figure 14. Satellite C Position Vector Components Neglecting SRP

This figure shows the position vector components for Spacecraft C without including the effects of SRP. The plot reveals the expected periodic behavior in each component. The increased amplitude in the variations observed in the y-component is expected as the spacecraft's distance to Itokawa decreases.
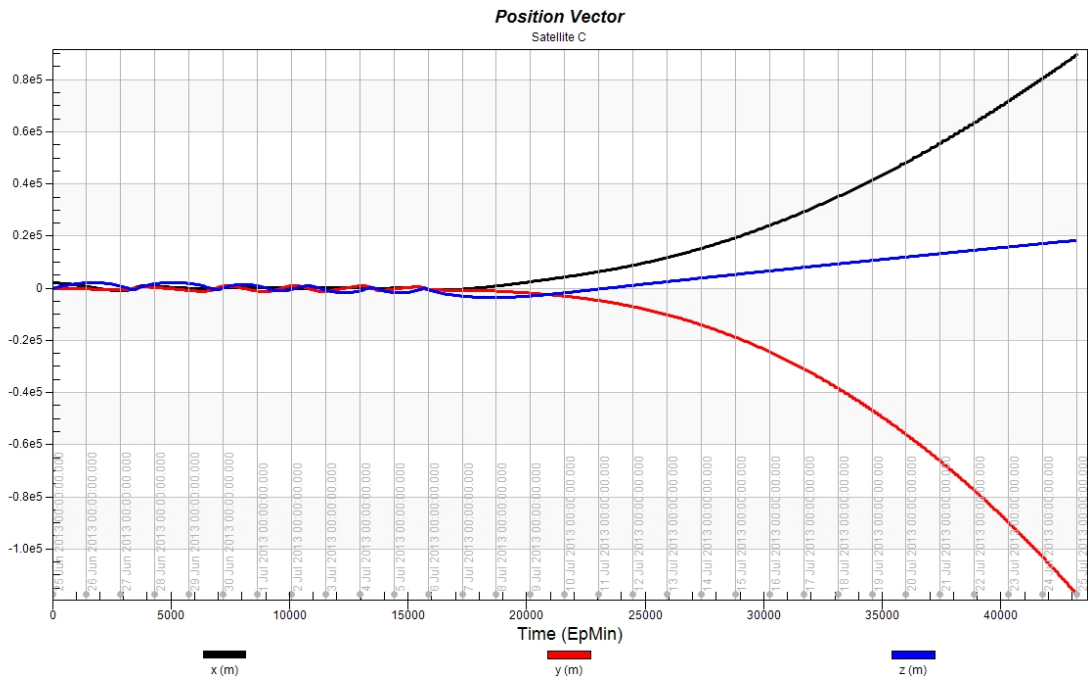

Figure 15. Satellite C Position Vector Components Including SRP

This figure shows a plot of the position vector components for Satellite C including the effects of SRP. The plot shows an initial periodic behavior in each component for several days. After roughly 10-days, each component begins to deviate exponentially from its initial periodic state.
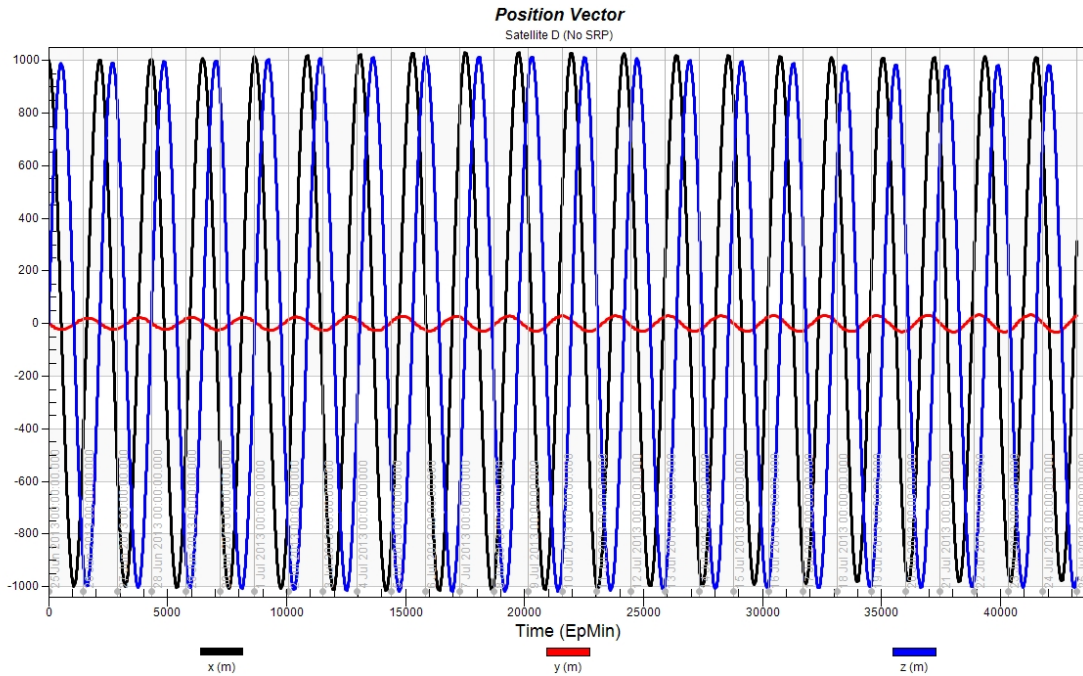

Figure 16. Satellite D Position Vector Components Neglecting SRP

This figure shows the position vector components for Spacecraft D without including the effects of SRP. The expected periodic behavior of each component is observed. The increased amplitude seen in the y-component is the result or the 91° inclination and the closer proximity to Itokawa.
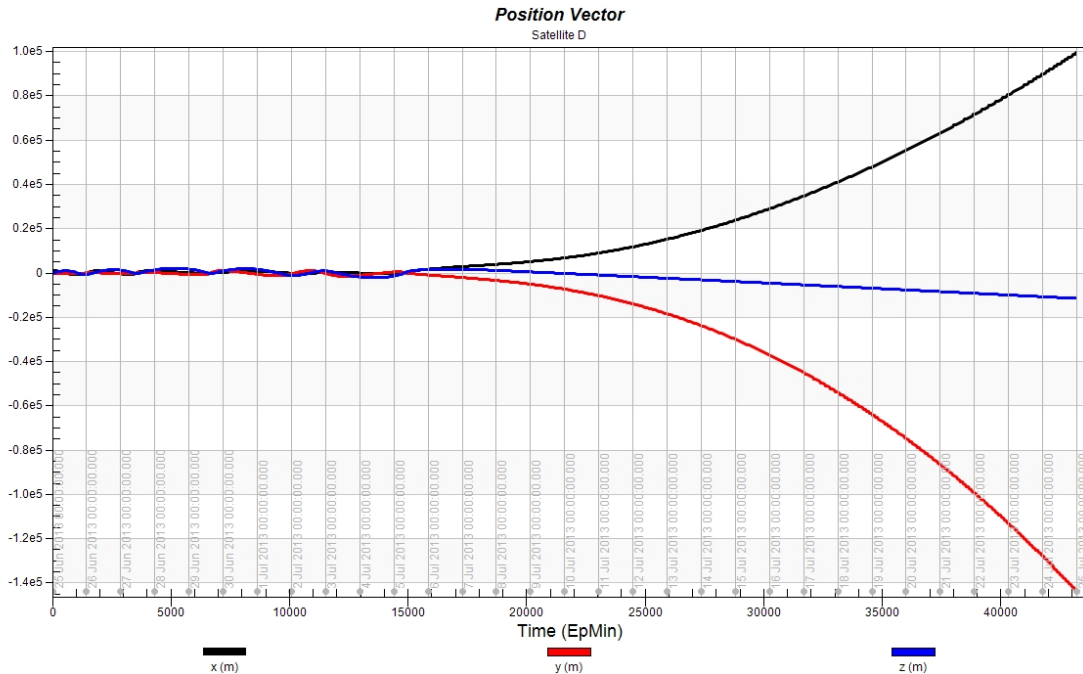
Figure 17. Satellite D Position Vector Components Including SRP

This figure shows a plot of the position vector components for Satellite D including the effects of SRP. Similar to Spacecraft C, this plot reveals that after roughly 10-days, the spacecraft enters an escape trajectory due to the effects of SRP.

The results for spacecraft E reveal more prominent deviations for each of the position vector components when SRP is neglected as Figure 18 shows. This indicates greater perturbations due to the non-uniform gravitational environment surrounding Itokawa. This result is expected since the force of gravity is inversely related to distance as discussed in Chapter II. When SRP is accounted for, the spacecraft is ultimately ejected from the system. However, it takes nearly 2-weeks for this to occur. This means that, under these conditions, potentially even longer tracking data arcs could be obtained.
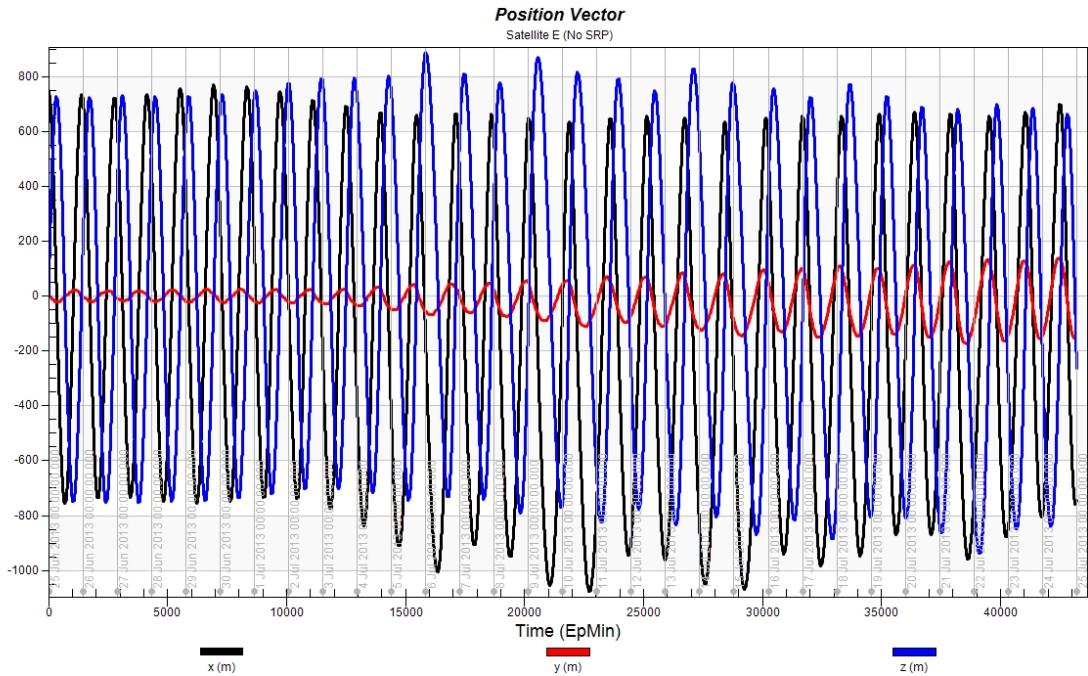
Figure 18. Satellite E Position Vector Components Neglecting SRP

This figure shows the position vector components for Spacecraft E without including the effects of SRP. While periodic behavior is observed, the varying maxima and minima seen indicates an increase in the effects of Itokawa's non-uniform gravitational environment.
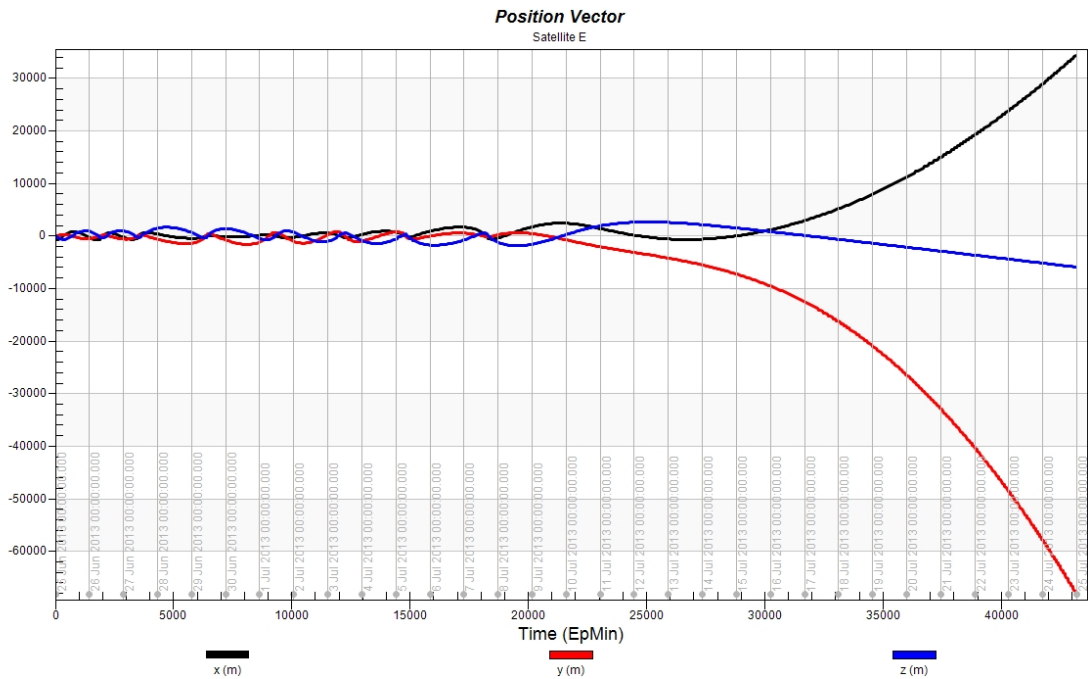

Figure 19. Satellite E Position Vector Components Including SRP

82

This figure shows a plot of the position vector components for Satellite E including the effects of SRP. The initial behavior is not directly periodic but the oscillatory nature indicates an initially bound orbit. However, the spacecraft ultimately enters an escape trajectory after roughly 15 days.

The orbits for spacecraft F and G show dramatic variations in their respective position vectors when SRP is neglected. The magnitude of these perturbations is a direct result of the proximity to Itokawa and is desirable in terms of mapping the gravity field. However, when SRP is considered, the orbit of each spacecraft decays rapidly. Spacecraft F impacts Itokawa after slightly more than a day while spacecraft G impacts after roughly 16 hours. Such a short lifetime is problematic for an SST mission and would most likely require continuous control.
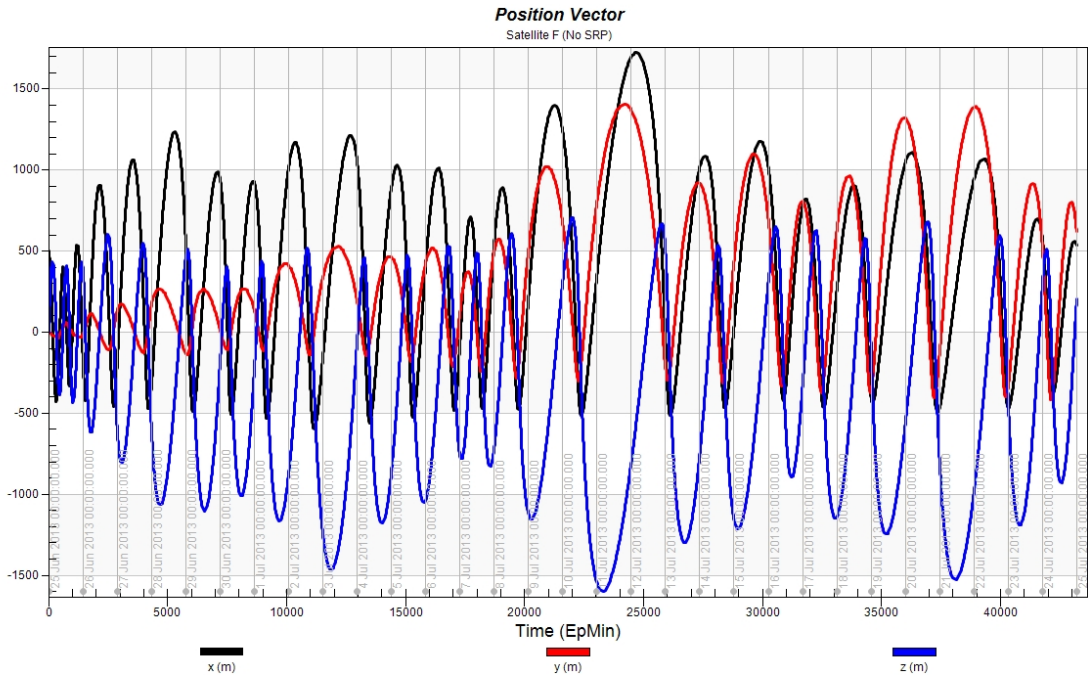
Figure 20. Satellite F Position Vector Components Neglecting SRP

This figure shows the position vector components for Spacecraft F without including the effects of SRP. The periodic nature of each component indicates a bound orbit. The variation in amplitude observed in each component is attributed to the non-uniformity in Itokawa's gravity field.
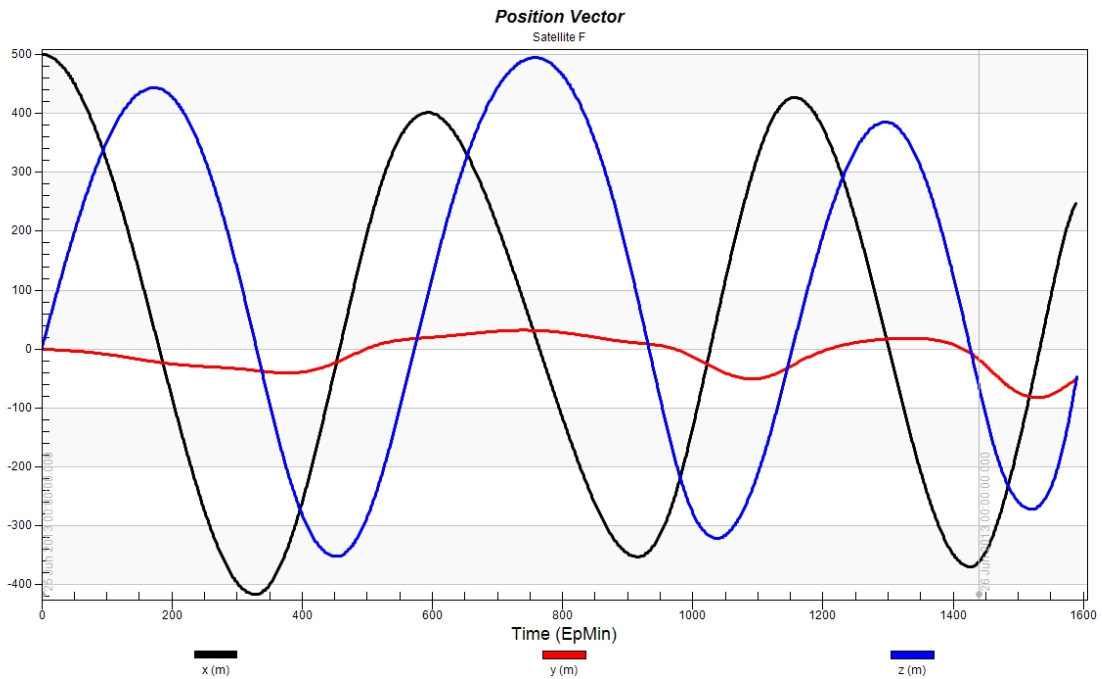

Figure 21. Satellite F Position Vector Components Including SRP

84

This figure shows a plot of the position vector components for Satellite F including the effects of SRP. When SRP is included satellite F impacts Itokawa in just over a day.
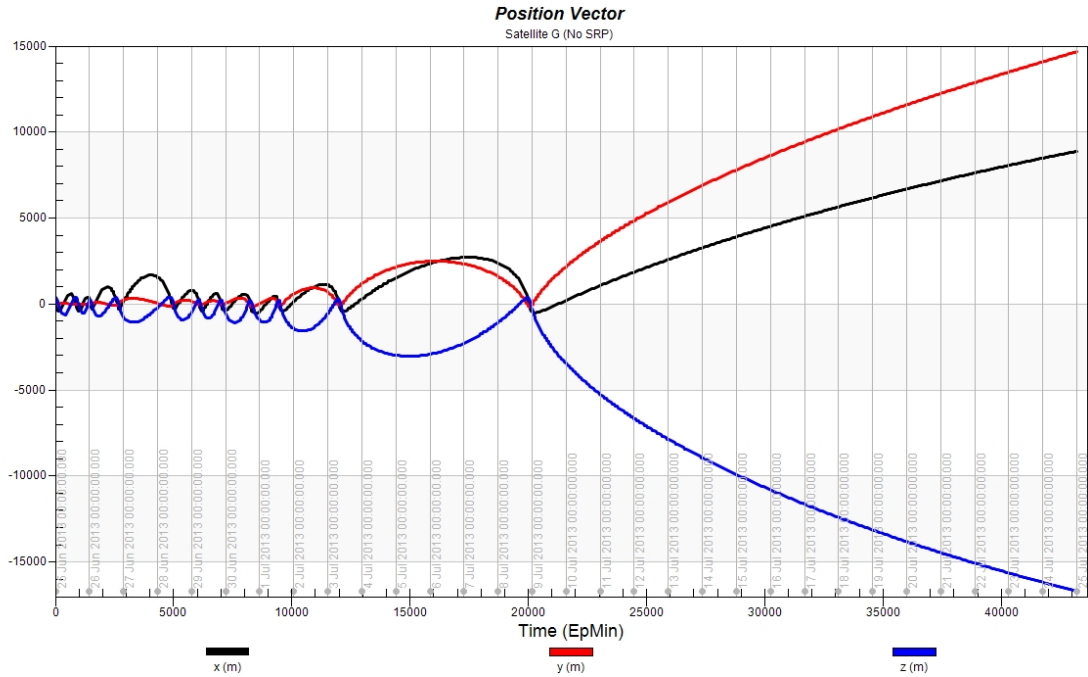

Figure 22. Satellite G Position Vector Components Neglecting SRP

This figure shows the position vector components for Spacecraft G without including the effects of SRP. After approximately 2-weeks, the spacecraft is ejected from the system.
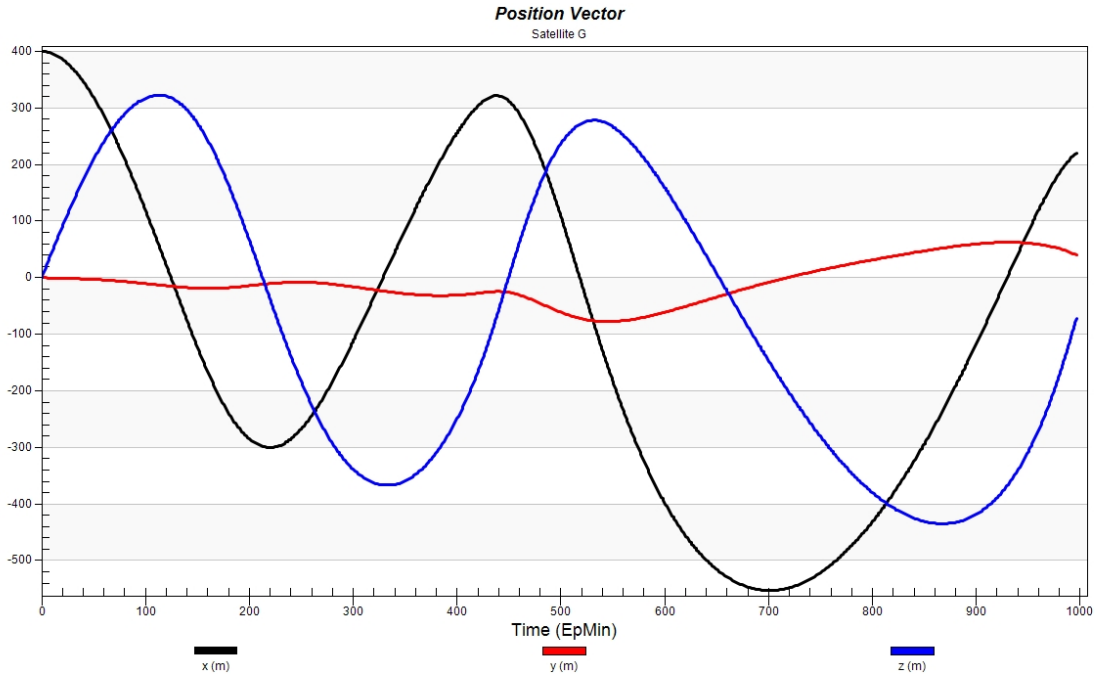

Figure 23. Satellite G Position Vector Components Including SRP

85

This figure shows a plot of the position vector components for Satellite G including the effects of SRP. The spacecraft impacts Itokawa's surface after approximately 16 hours.

Ideally, the orbit used for mapping the gravity field would be one subject to measurable gravitational perturbations but would not require constant corrective maneuvers in order to maintain orbit. Based on the results presented above the most likely candidates for such orbits are spacecraft C, D, E and F.

If the trajectories for Satellites C, D, E, and F violate the requirement that the orbit remain outside the Brillouin sphere, the subsequent data generated by the simulation will no longer be valid. To verify that this requirement is not violated, the magnitude of the position vector for spacecraft C, D, E, and F is plotted in Figure 24 as a function of time over 14-days. The plot is limited to 14-days because this is the time that corresponds to the longest periodic orbit for any of the 4 satellites. The Brillouin sphere radius is shown as a horizontal line for reference. Figure 24 shows that the trajectory for Satellite F penetrates the Brillouin sphere after slightly more than 1-day. This occurs shortly before the spacecraft impacts the surface of Itokawa. The magnitude of the position vector for Satellite C and Satellite D drops below the lower limit between day 10 and 11. However, this occurs near the end of the stable period for each spacecraft as shown in Figure 15 and Figure 17. Satellite E, never drops below the lower limit of 278 m.
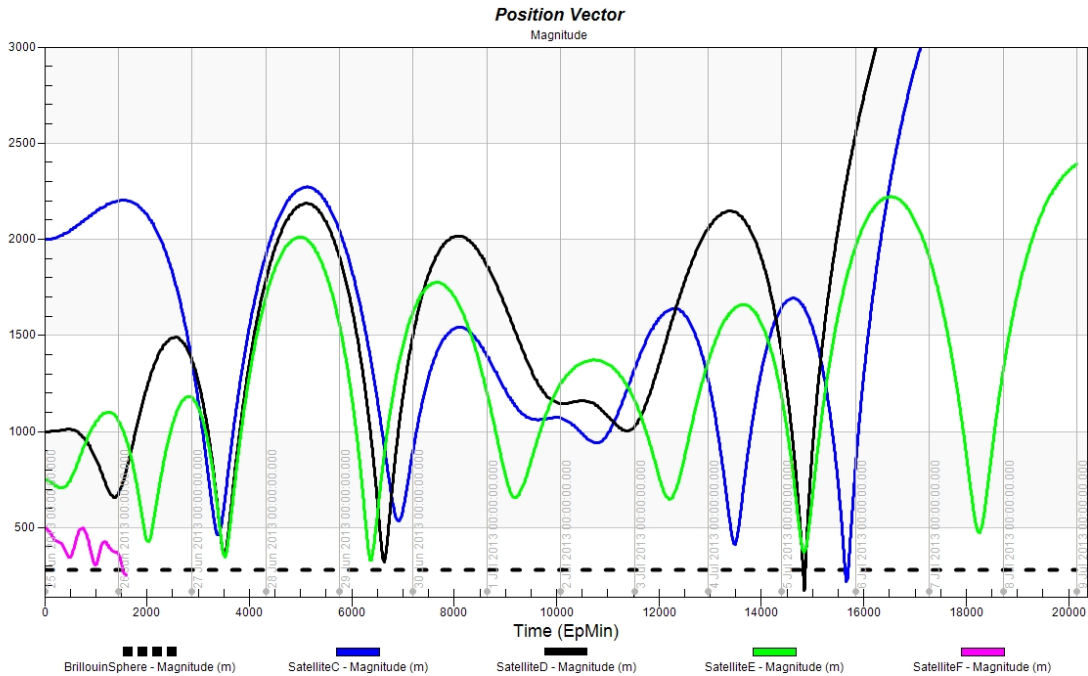
Figure 24. Position Vector Magnitudes

This figure plots the magnitude of the position vector for each spacecraft as a function of time over a 14-day period. The radius of the Brillouin Sphere is included as a reference showing the minimum radius permitted prior to invalidating the data set.

While the data presented above shows that orbits with an initial semi-major axis of between 750 m and 2000 m result in the most viable candidates for a gravity-mapping mission. The resulting trajectories suggest short-term stability over several days. As the semi-major axis increases beyond 2000 m, the effects of SRP become more pronounced, dramatically decreasing the stability of the orbit. In order to counter these effects, more frequent, if not continuous orbit corrections would be required. At best, this would complicate data collection since any accelerations resulting from non-conservative forces must be accounted for and removed from the data. While an initial semi-major axis of 2000 m results in a reasonably stable trajectory, the amplitude of the gravitational perturbations are reduced due to the increased distance from Itokawa as Figure 16

indicates. For this reason, the remainder of this work focuses on orbits with initial semi-major axis values of 750 m and 1000 m.

Data Collection Times

In addition to determining a range of initial semi-major axes suitable for SST data, collection window must be assessed. To do this, several additional simulations were executed with semi-major axis values of 750 m and 1000 m. For each set of spacecraft, D and E, all of the initial conditions were held constant save the RAAN, which was increased by 30° over the full range of 360°. The resulting 24 orbits exhibited an array of behaviors ranging from impact to escape over the 30-day window. Because of the wide variation in trajectories observed, it was prudent to determine if any of the resulting orbits penetrated the Brillouin sphere in order to ensure data validity.

A summary for each orbit was generated noting any times when the orbit crossed Brillouin sphere radius.   From these data the initial time, if any, was noted. These times are presented in Table 11.

Table 11. Time of Brillouin Sphere Penetration

This table presents the date and time when each spacecraft penetrates the circumscribing sphere around Itokawa. The number of days past the orbit epoch of 25 Jun 2013 00:00:00.000 is also shown.

Spacecraft	Radius	Time Since Orbit Epoch (days)	Date
SpacecraftD1_01	277.9	10.289	05 Jul 2013 06:55:50.754
SpacecraftD1_02		No Event Times Available	
SpacecraftD1_03		No Event Times Available	
SpacecraftD1_04		No Event Times Available	
SpacecraftD1_05	277.9	10.675	27 Jun 2013 07:15:06.465
SpacecraftD1_06	277.9	2.302	27 Jun 2013 07:15:06.465
SpacecraftD1_07	277.9	4.521	29 Jun 2013 12:30:30.663
SpacecraftD1_08		No Event Times Available	

Table 11 cont.

Spacecraft	Radius	Time Since Orbit Epoch (days)	Date
SpacecraftD1_09		No Event Times Available	
SpacecraftD1_10	277.9	27.309	22 Jul 2013 07:25:25.709
SpacecraftD1_11	277.9	3.231	28 Jun 2013 05:32:43.735
SpacecraftD1_12	277.9	3.472	28 Jun 2013 11:20:18.001
SpacecraftE1_01	277.9	3.194	28 Jun 2013 04:40:01.705
SpacecraftE1_02	277.9	2.863	27 Jun 2013 20:43:04.458
SpacecraftE1_03		No Event Times Available	
SpacecraftE1_04	277.9	13.542	08 Jul 2013 13:00:03.912
SpacecraftE1_05	277.9	2.69	27 Jun 2013 16:33:06.153
SpacecraftE1_06	277.9	2.403	27 Jun 2013 09:40:07.124
SpacecraftE1_07	277.9	3.285	28 Jun 2013 06:50:39.325
SpacecraftE1_08		No Event Times Available	
SpacecraftE1_09		No Event Times Available	
SpacecraftE1_10		No Event Times Available	
SpacecraftE1_11	277.9	2.608	27 Jun 2013 14:35:00.673
SpacecraftE1_12	277.9	3.562	28 Jun 2013 13:28:54.277

For spacecraft D, 7 of the 12 simulated trajectories decay below the Brillouin sphere radius during the simulation scenario. In addition to validating the trajectories of each spacecraft, the data in Table 11 also shows that there is a limit on the time available for data collection since all data obtained after the trajectory penetrates the circumscribing sphere is rendered invalid. The average time between the orbit epoch of 25 Jun 2013 00:00:00.000 UTCG and penetration of the Brillouin sphere radius is 8.83 days. This average is elevated due to SatelliteD1_05 and SatelliteD1_10. The median time for spacecraft D is 4.52 days.

For spacecraft E, 8 of the 12 simulated trajectories decay below the Brillouin sphere radius during the simulation scenario. The average time between the orbit epoch

of 25 Jun 2013 00:00:00.000 UTCG and penetration of the Brillouin sphere radius for spacecraft E is 4.3 days with a median of 3.03 days.

While the potential for the orbit to decay below the Brillouin sphere radius is an important consideration for this work, it is a direct result of the model used to generate the spacecraft trajectories. With respect to SST data collection, the orbit inclination is a more pertinent consideration because it affects the ability to achieve global coverage if it deviates from being in a near polar orbit. Both the gravitational and non-gravitational perturbations can result in changes to a spacecraft's orbital inclination. These effects were evaluated by plotting each satellite's inclination as a function of time over the 30-day simulation scenario. The resulting plots are shown in Figure 25 and Figure 26.

Figure 25. Orbit Inclination for Spacecraft D

Plots the inclination as a function of time for Satellites D1 through 12. After roughly 4-days, the inclination of several orbits begins to deviate by more than a few degrees from its initial 91° inclination.
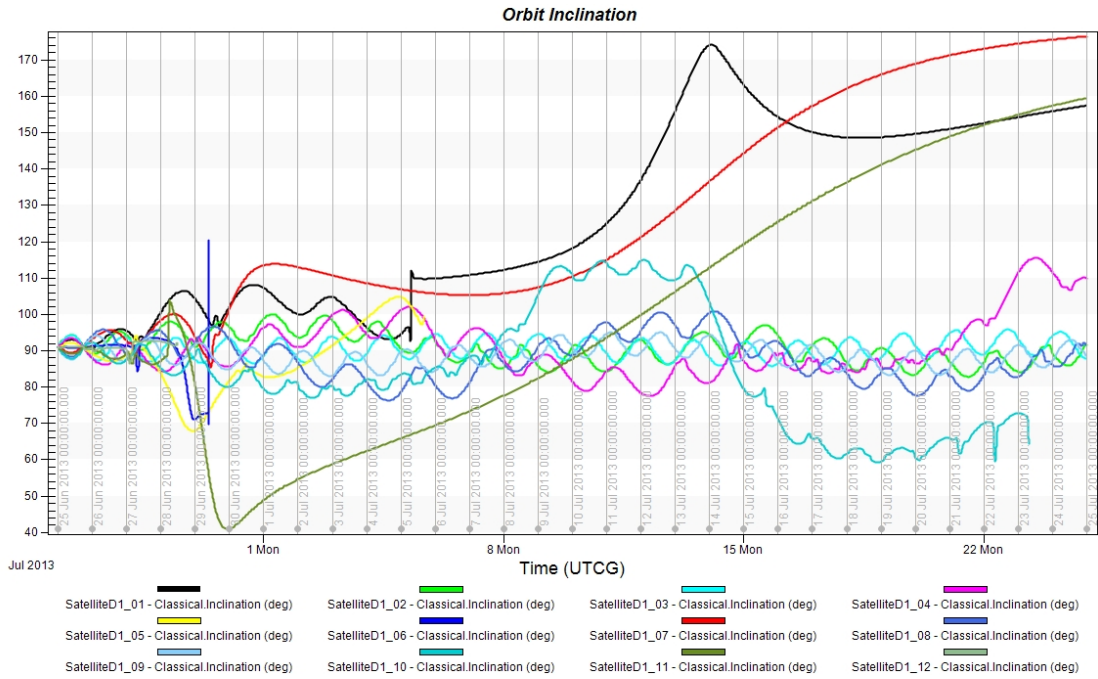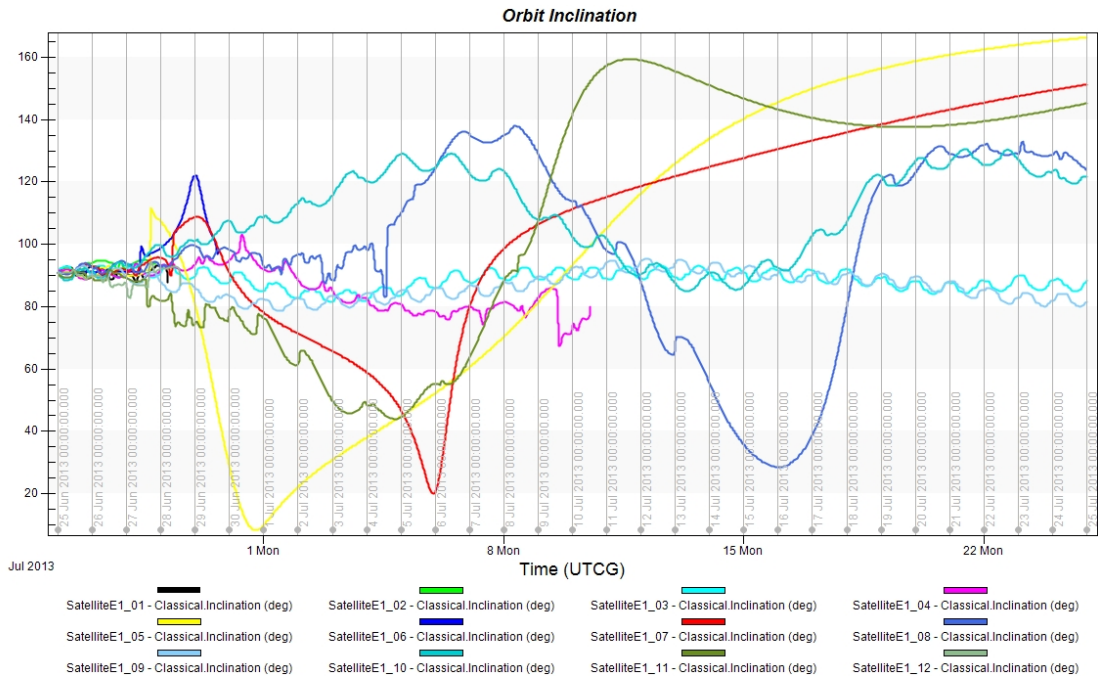

Figure 26. Orbit Inclination for Spacecraft E

Plots the inclination as a function of time for Satellites E 1 through 12. After roughly 4-days, the inclination of each orbit begins to deviate by more than a few degrees from its initial 91° inclination.

To assess the changes in inclination seen in Figure 25 and Figure 26, an analysis similar to that conducted for each spacecraft's radius was used. Near polar orbits are loosely defined as orbits with inclinations close to 90°. Because the definition of near polar orbits is not specific and that the orbits exist in a highly perturbed environment, limits of ±5° were chosen as the criterion for evaluating the inclination variances. If the inclination change exceeded 91°±5°, the corresponding date and time were reported for each spacecraft. These data are summarized is in Table 12.

Table 12. Inclination Variance

This table provides the date and time when the inclination for each spacecraft exceeds 91°±5°.

Spacecraft	Inclination Change	Time Since Orbit Epoch (days)	Date
SpacecraftD1_01	+5	2.6939378	27 Jun 2013 16:39:16.226
SpacecraftD1_02	+5	2.95250745	27 Jun 2013 22:51:36.643
SpacecraftD1_03	-5	19.23457457	14 Jul 2013 05:37:47.243
SpacecraftD1_04	+5	5.93160845	30 Jun 2013 22:21:30.970
SpacecraftD1_05	+5	8.62313655	3 Jul 2013 14:57:18.998
SpacecraftD1_06	+5	4.38982342	29 Jun 2013 09:21:20.743
SpacecraftD1_07	+5	2.75249786	27 Jun 2013 18:03:35.815
SpacecraftD1_08		No Event Times Available	
SpacecraftD1_09	-5	4.69424082	29 Jun 2013 16:39:42.407
SpacecraftD1_10	+5	13.14175868	8 Jul 2013 03:24:07.950
SpacecraftD1_11	+5	3.22553087	28 Jun 2013 05:24:45.867
SpacecraftD1_12		No Event Times Available	
SpacecraftE1_01		No Event Times Available	
SpacecraftE1_02		No Event Times Available	
SpacecraftE1_03	-5	5.71932180	30 Jun 2013 17:15:49.000

Table 12 cont.

Spacecraft	Inclination Change	Time Since Orbit Epoch (days)	Date
SpacecraftE1_04	+5	4.29898301	29 Jun 2013 07:10:32.132
SpacecraftE1_05	+5	2.68367495	27 Jun 2013 16:24:29.515
SpacecraftE1_06	+5	2.40071121	27 Jun 2013 09:37:01.449
SpacecraftE1_07	+5	3.33751358	28 Jun 2013 08:06:01.174
SpacecraftE1_08	+5	3.49013946	28 Jun 2013 11:45:48.049
SpacecraftE1_09	-5	3.15569782	28 Jun 2013 03:44:12.291
SpacecraftE1_10	+5	2.53480522	27 Jun 2013 12:50:07.171
SpacecraftE1_11	+5	13.43823010	08 Jul 2013 10:31:03.000
SpacecraftE1_12	-5	2.00790245	27 Jun 2013 00:11:22.771

Only 2 of the 12 trajectories simulated for Spacecraft D did not exceed the ±5° variances limit during the scenario time. Of the remaining 10, the average time before the inclination limits were exceeded was 6.76 days. However, the higher average time is attributed to SatellitesD1_03 and SatellitesD1_10, whose time to deviation was 19.2 days and 13.1 days respectively. The median time for this group of spacecraft was 4.54 days, which is commensurate with the overall trends seen in Figure 25.

For spacecraft E, 9 out of the 12 simulated trajectories exceeded the ±5° variances permitted. The average time required before violation occurred was 4.31 days with a median time of 3.25 days. This average is more representative of Figure 26 than the average for Satellite D is of Figure 25.

Based on the analysis above, in an uncontrolled state the available window for SST data collection is on the order of 4.5 days for circular, near polar orbits with an initial radius of 1000 m and 3.25 days if the initial radius is 750 m. These times coincide with the times found from the Brillouin sphere analysis. Consequently, they were used as

the data collection window for generating the range and range rate data between

spacecraft, which is discussed in the next section.

Range and Range-Rate

In order to generate simulated SST data, the trajectories of several additional

spacecraft had to be simulated. The initial conditions for these trajectories were chosen

such that each new spacecraft would create a pair with one of the existing spacecraft,

resulting in 24 distinct pairs. Each pair of spacecraft would initially be in the same orbit

separated by some distance. The separations between spacecraft in the GRACE and

GRAIL missions are not realistic around small NEO because such separations would

require the spacecraft to be in orbits with radii exceeding the Hill Radius for Itokawa. As

the data presented above has show, an orbit this far from Itokawa would not be bound.

To avoid this problem, the LOS separation between the simulated spacecraft had to be

much closer.

There are limits to the LOS range that can be maintained. These become even

more evident as the altitude decreases. In order to maintain the same LOS range between

spacecraft as the altitude changes, the angular separation between the two spacecraft must

also change. For two spacecraft in identical, unperturbed orbits, the maximum LOS

range occurs geometrically when the angular separation is 180°. This is not however,

realistic since at this angle, the NEO would lie directly between the two spacecraft and

would block LOS communications between the two craft. Given this, the maximum

angular separation between the two spacecraft that can exist before the object blocks the

LOS, must decrease with decreasing altitude and is ultimately dependent on the size and

shape of the object being orbited. While additional investigation into how the initial

separation between the two spacecraft affects data collection may be prudent, this work did not explore these effects. Instead, an initial angular separation of 15° was used for each spacecraft pair. The resulting initial LOS separation was then calculated using Equation (13) where ν is the initial angular separation and r is the initial orbital radius. Use of Equation (13) assumes that both orbits are circular. The resulting LOS separation for spacecraft D and E is 261.05 m and 195.79 m respectively.

$$r_{LOS} = sin\left(\frac{\upsilon}{2}\right)(2r) \tag{13}$$

New trajectories were generated for spacecraft given designations D2_01 through D2_12 and E2_01 through E2_12. The initial conditions for these new spacecraft were identical to those used for spacecraft D1_01 through D1_12 and spacecraft E1_01 through E1_12 with the exception of their true anomaly, which was set to 15°. This provided the desired initial angular separation of 15° between spacecraft.

Using the data collection windows established in the previous section, range and range-rate data was reported between each spacecraft pair. These data are plotted in Figure 27 through Figure 53. Analysis of these plots focuses on the changes in range and range-rate and their respective magnitudes over the plot time. Large changes in the LOS distance and velocity are indicative of the trajectories of the two spacecraft diverging. Since low-low SST assumes that the two spacecraft orbit along roughly the same trajectory, large deviations from this condition are not desirable. Additionally, the duration of orbit stability is of interest since data cannot be collected during the execution of corrective maneuvers.
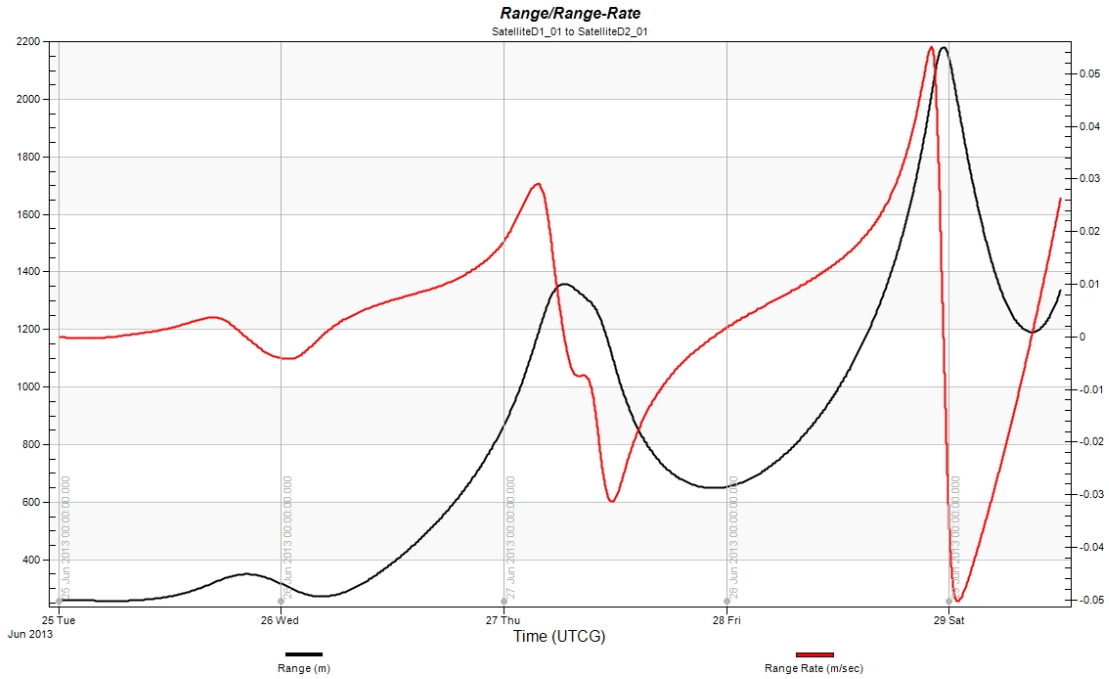
Figure 27. Range and Range-Rate Plot for SatelliteD1_01 to SatelliteD2_01

The LOS distance between SatelliteD1_01 and SatelliteD2_01 varies slightly over the first day of observations. After this, the separation between the two spacecraft quickly increases beyond 1 km. As the observations progress, the magnitude of the LOS velocity is on the order of 10^{-2} m/sec with sharp variations in direction.
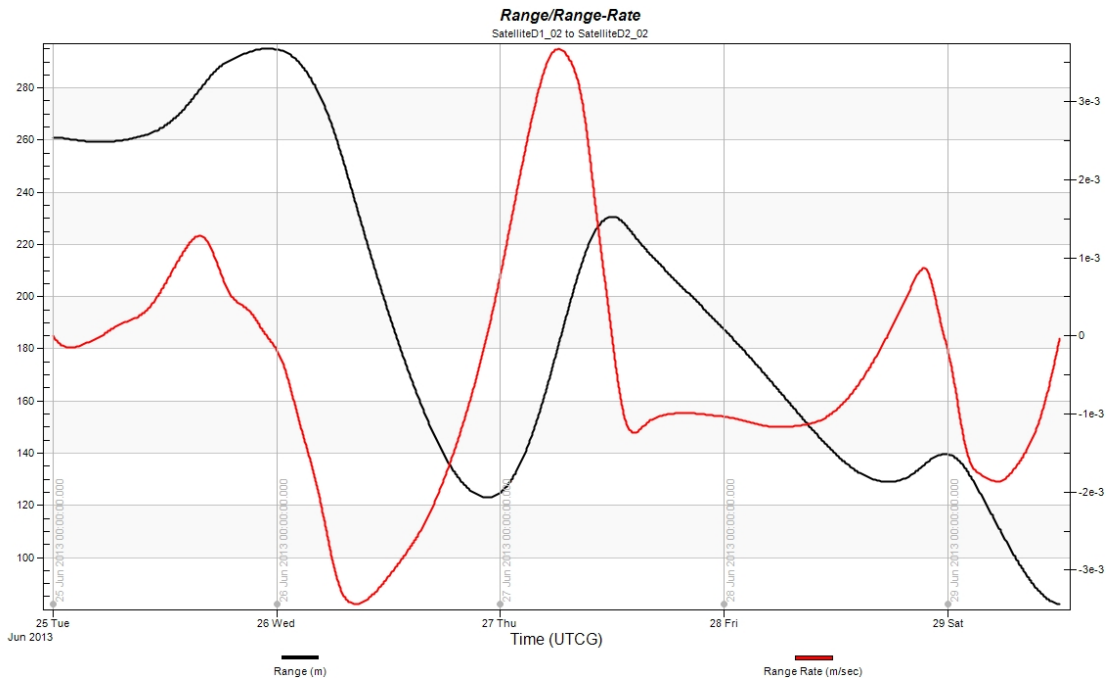

Figure 28. Range and Range-Rate Plot for SatelliteD1_02 to SatelliteD2_02

SatelliteD1_02 and SatelliteD2_02 display comparatively consistent behavior. The LOS range varies by approximately 300 m over the observation period with the range-rate remaining on the order of a few mm/sec (10^{-3} m/sec).
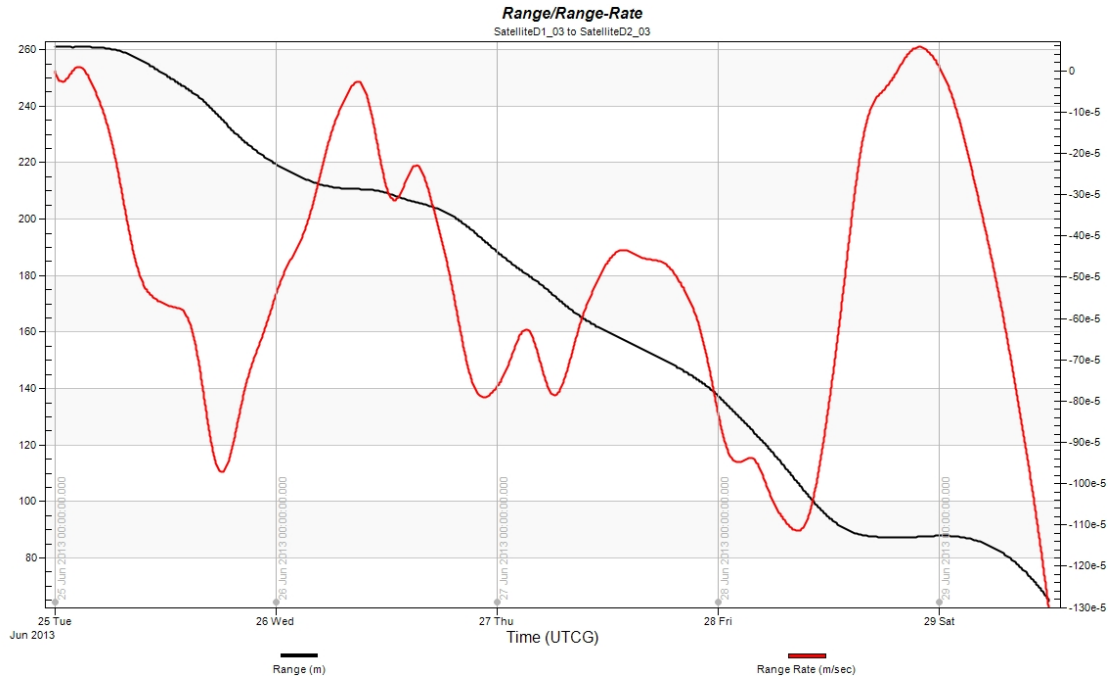

Figure 29. Range and Range-Rate Plot for SatelliteD1_03 to SatelliteD2_03

The LOS distance between SatelliteD1_03 and SatelliteD2_03 continually decreases throughout the observation window. The corresponding changes in LOS velocity are also smaller than those of the previous Satellites. The LOS velocity changes vary from 10^{-5} m/sec to 10^{-6} m/sec, which is 2 to 3 orders of magnitude less than that of the previous spacecraft.
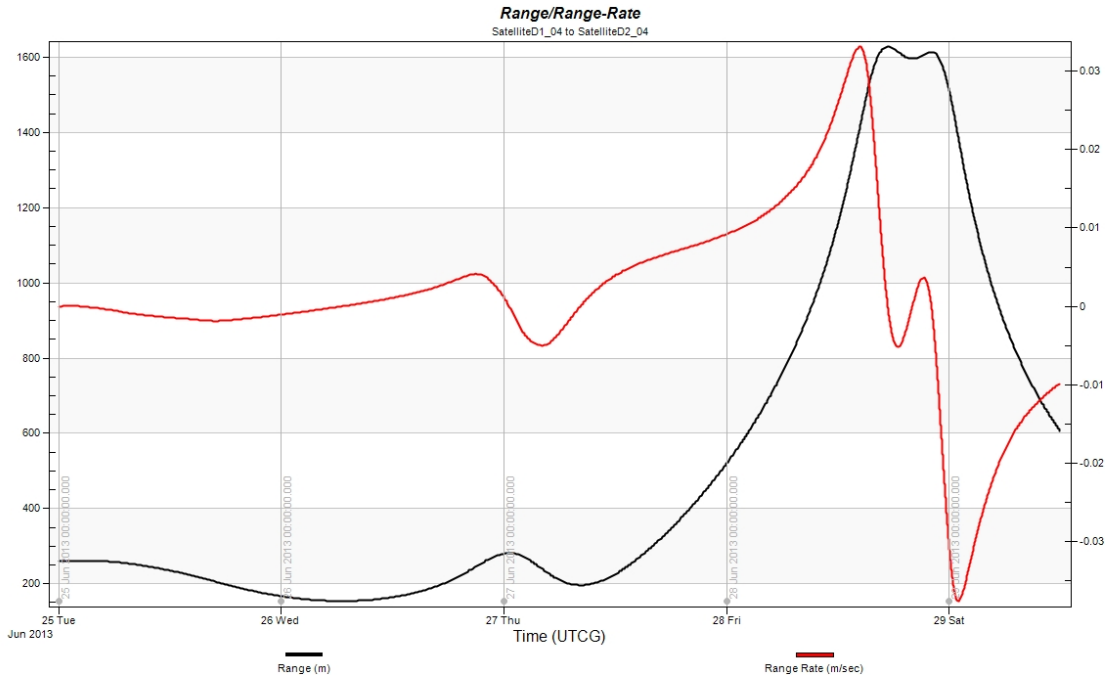
97

Figure 30. Range and Range-Rate Plot for SatelliteD1_04 to SatelliteD2_04

The range and range-rates observed between SatelliteD1_04 and SatelliteD2_04 vary consistently for nearly 2-days prior to diverging rapidly between day 3 and day 4. By the end of day 4 the separation between spacecraft exceeds 1.5 km.
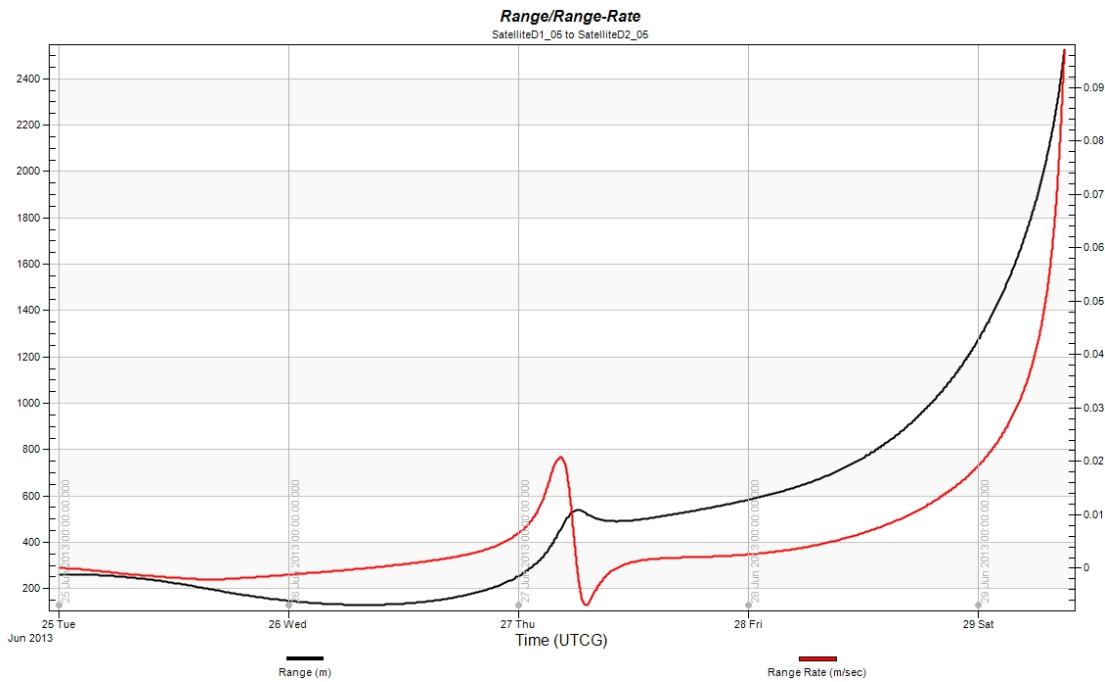

Figure 31. Range and Range-Rate Plot for SatelliteD1_05 to SatelliteD2_05

98

The LOS distance between SatelliteD1_05 and SatelliteD2_05 begins to diverge after the first day of observations. The rate of divergence continually increases beyond this point. By the end of the observations the range and range-rate curves increase exponentially.
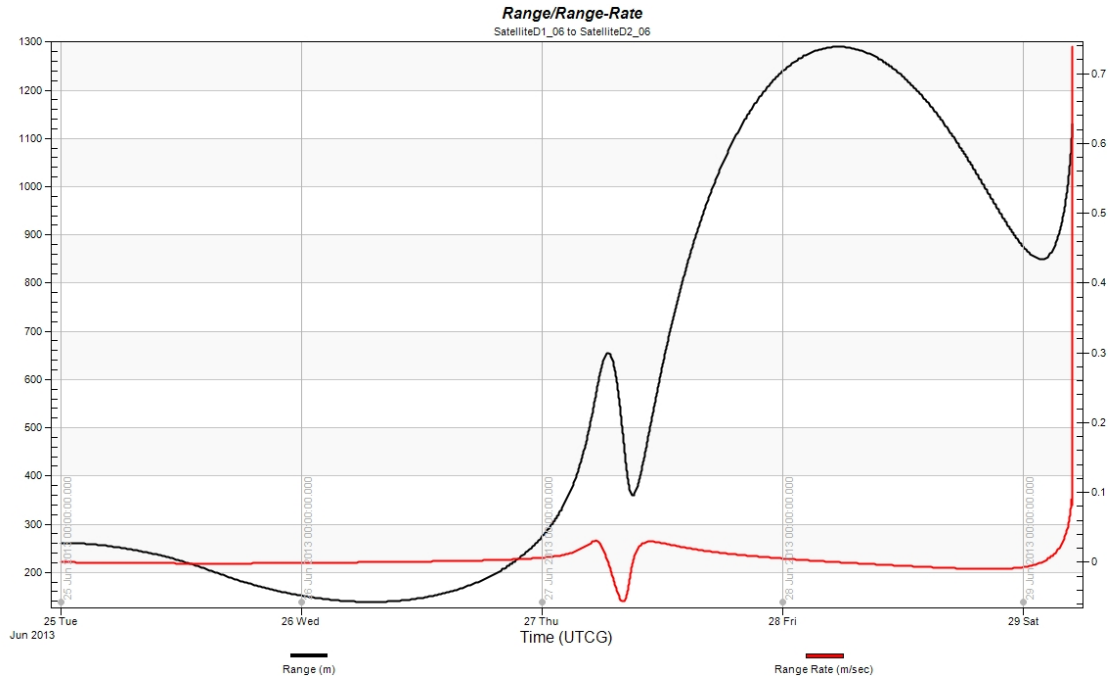

Figure 32. Range and Range-Rate Plot for SatelliteD1_06 to SatelliteD2_06

The range between SatelliteD1_06 and SatelliteD2_06 exhibits a relatively uniform periodic behavior early on. This is emphasized by the nearly flat range-rate over the same time frame. By the end of the observation window, however, both plots quickly grow exponentially.

Figure 33. Range and Range-Rate Plot for SatelliteD1_07 to SatelliteD2_07

The LOS range between SatelliteD1_07 and SatelliteD2_07 is varies by roughly 100 m for approximately 2-days. However, beyond this time the distance between the two spacecraft diverges rapidly as indicated by the LOS velocity exceeding 10^{-2} m/sec. By the end of the observation window, the distance between the two craft approaches 2 km with the relative velocity continuing to increase.
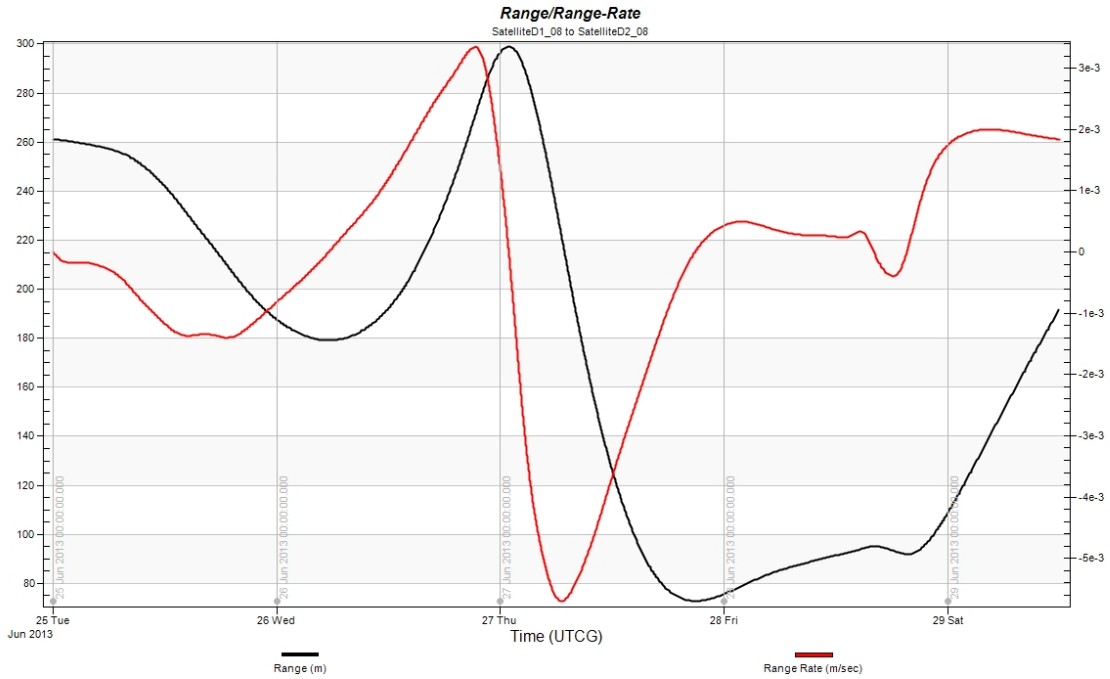
Figure 34. Range and Range-Rate Plot for SatelliteD1_08 to SatelliteD2_08

 The LOS range and range rate variations observed between SatelliteD1_08 and SatelliteD2_08 are relatively stable. The range varies between a few tens of meters and nearly 300 m with the corresponding rate of change not exceeding 10^{-3} m/sec.
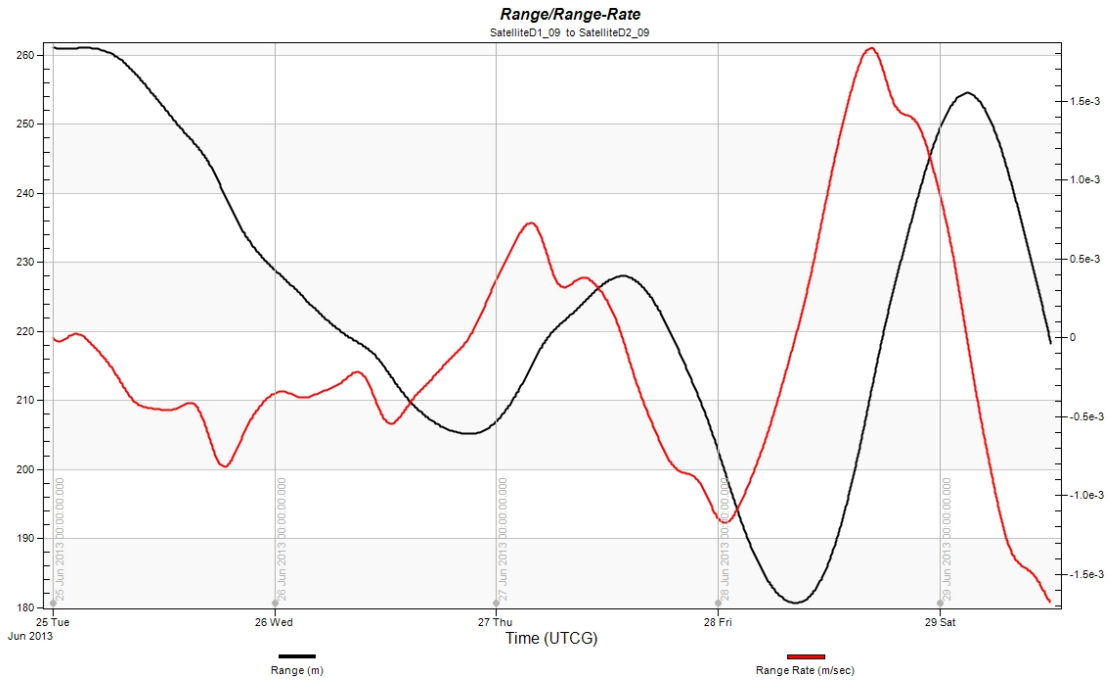
Figure 35. Range and Range-Rate Plot for SatelliteD1_09 to SatelliteD2_09

101

The LOS distance between SatelliteD1_09 and SatelliteD2_09 fluctuates between the initial separation of the two spacecraft and 180 m. The range-rate between the two craft is on the order of 10^{-4} m/sec and never exceeds 10^{-3} m/sec during the time of observation.
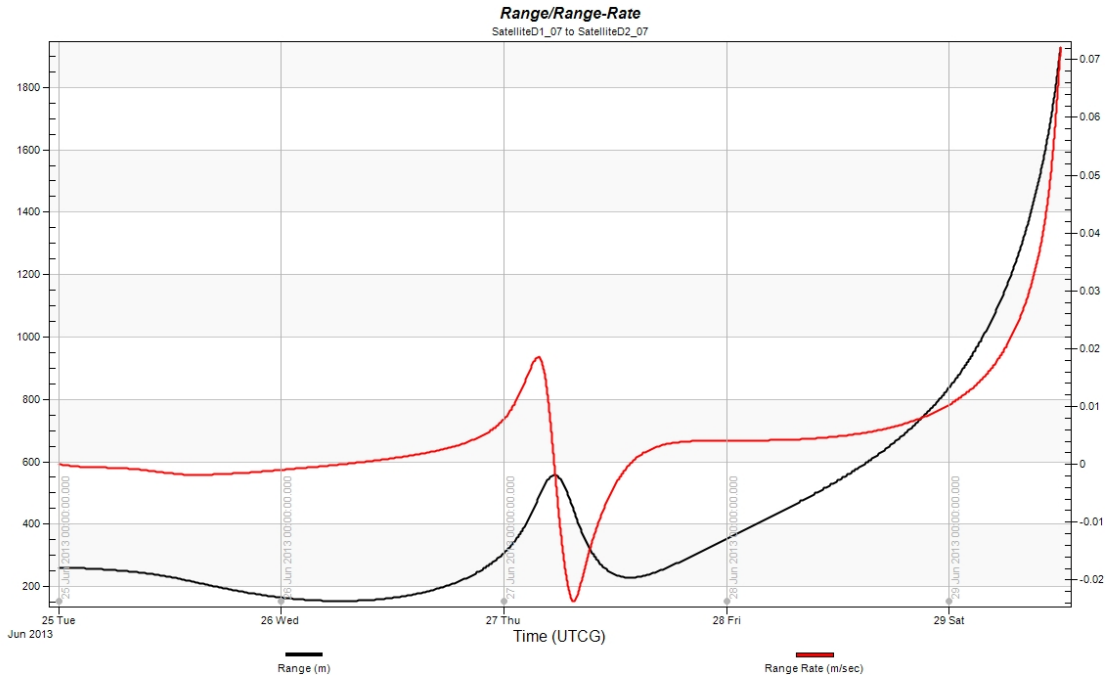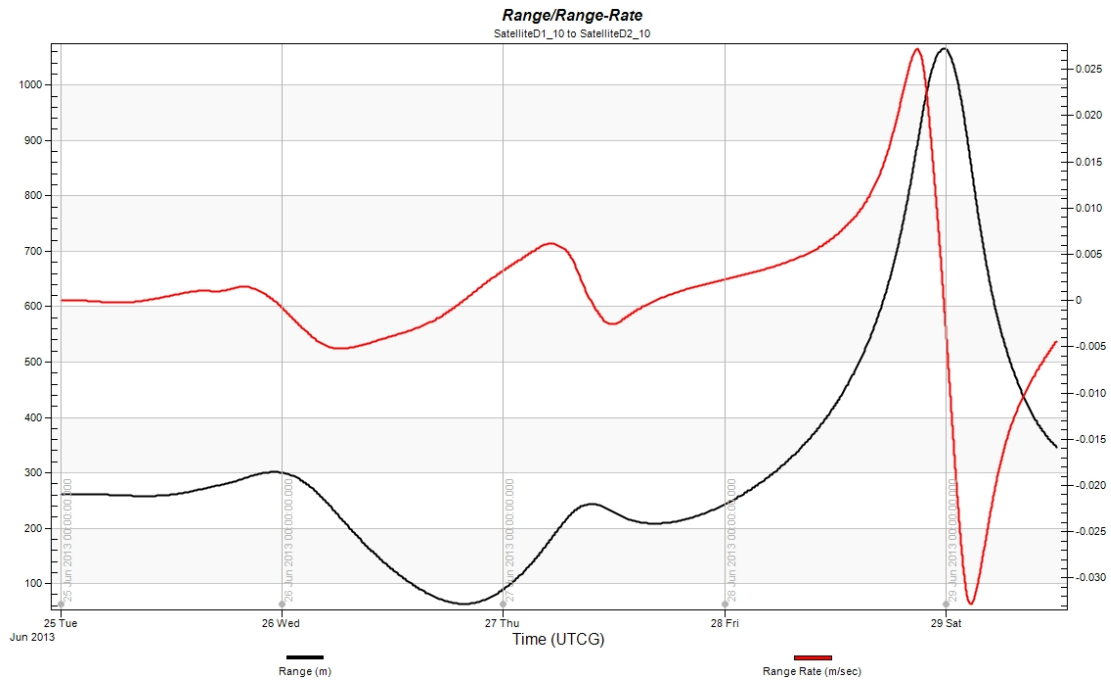

Figure 36. Range and Range-Rate Plot for SatelliteD1_10 to SatelliteD2_10

The LOS range between SatelliteD1_10 and SatelliteD2_10 exceeds 1 km by the beginning of the fourth day of observations. The corresponding range-rate also spikes at this point exceeding 2.5 x 10^{-2} m/sec.
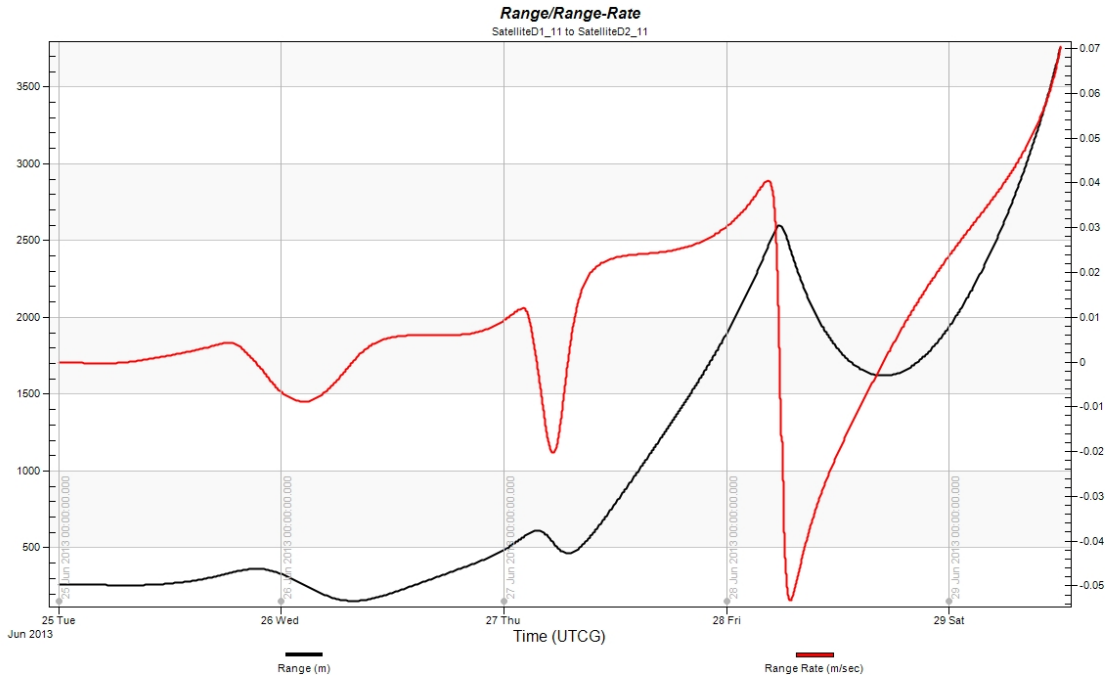
Figure 37. Range and Range-Rate Plot for SatelliteD1_11 to SatelliteD2_11

The separation between SatelliteD1_11 and SatelliteD2_11 rapidly increases over the 4.5-day observation window. By the middle of the third day, the separation reaches 1 km. At the end of the observations the distance between the two spacecraft exceeds 3.5 km and the rate of separation is continuing to increase.
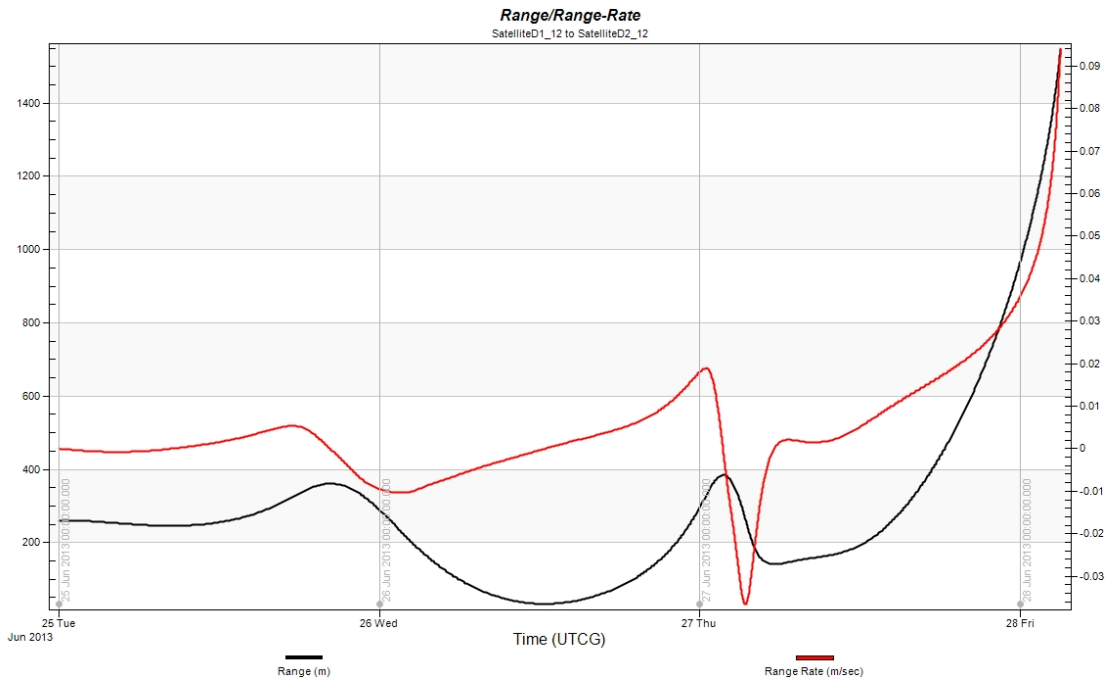
Figure 38. Range and Range-Rate Plot for SatelliteD1_12 to SatelliteD2_12

103

For the first two days of observations, the LOS range and range-rate between SatelliteD1_12 and SatelliteD2_12 fluctuates slightly. The separation is maintained within a few hundred meters and the range-rate barely exceeds 10^{-2} m/sec. However, this quickly changes by day three with both measurements increasing exponentially.

Figure 27 through Figure 38 display an array of behavior with respect to the relative motion between each pair of spacecraft. In some instances there is a rapid divergence between the two spacecraft. Other times, the two spacecraft follow nearly identical trajectories. In general, an examination of the LOS separation and velocity between the two spacecraft can be used to assess the relative stability between the two trajectories. Small changes in the LOS range generally correspond to small changes in the LOS velocity. These characteristics are indicative of relative stability between the two trajectories. For instance, Figure 29 shows the range and range-rate between SatelliteD1_03 and SatelliteD2_03. The relative separation between the two spacecraft is maintained between approximately 20 m and 250 m over the 4.5-day window and the corresponding range-rate is on the order of 10^{-5} m/s. Figure 39 shows a plot of the 3-dimensional trajectory for SatelliteD1_03 and SatelliteD2_03. In this plot, the two spacecraft follow nearly the same trajectory throughout the entire simulation. The relative stability between the two trajectories results in small changes in the LOS position and velocity between the two spacecraft. This situation is ideal for SST.

Figure 39: SatelliteD1_03 and SatelliteD2_03 Orbit Visualization

This figure shows a 3-dimensional plot of the trajectories for SatelliteD1_03 and SatelliteD2_03 over the entire simulation. The relative stability between the two trajectories is apparent.

Figure 28, Figure 34, and Figure 35 exhibit similar behavior. In these plots the range between the two spacecraft doesn't exceed more than approximately 250 m. The corresponding LOS velocity is varies between roughly 10^{-5} m/s and 10^{-3} m/s. These results imply that the associated trajectories are relatively stable overall.

Several of the plots show large variations in the LOS range between the two spacecraft. These large variations represent a divergence between the their respective trajectories. This can be seen, for example, by comparing the range and range-rate plot between SatelliteD1_04 and SatelliteD2_04 to a 3-dimensional plot of their respective trajectories. While the changes in range and range-rate shown in Figure 30 are initially small, the LOS separation between the two spacecraft increases rapidly after 2-days.

This is followed by a rapid decline by the fourth day. These large changes occur as the

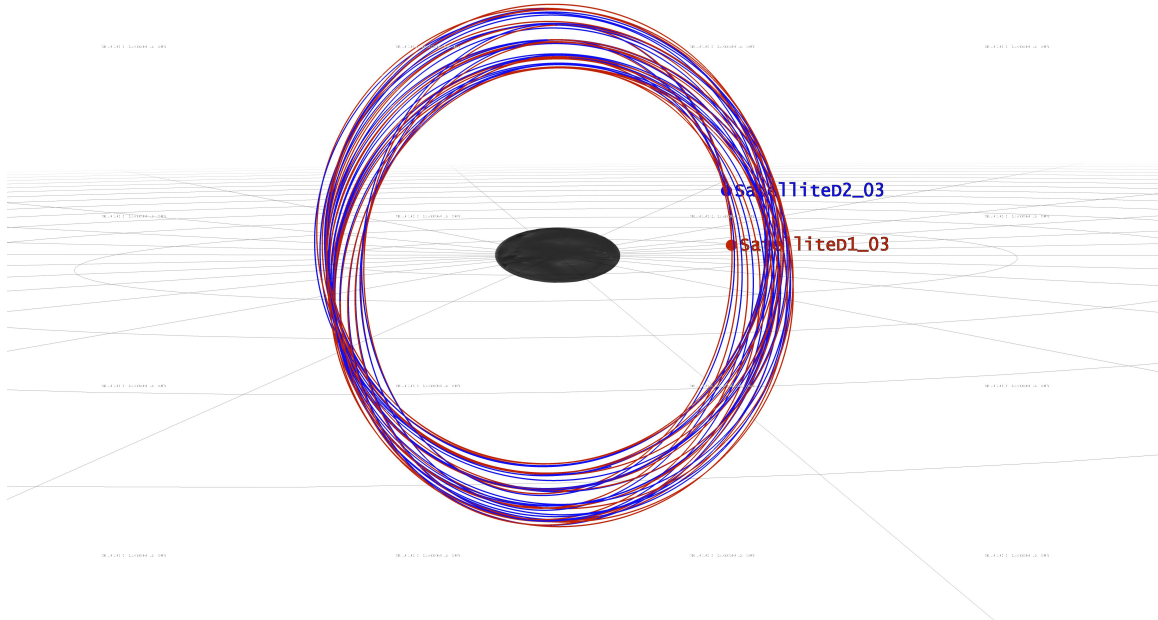two trajectories diverge as seen in Figure 40.
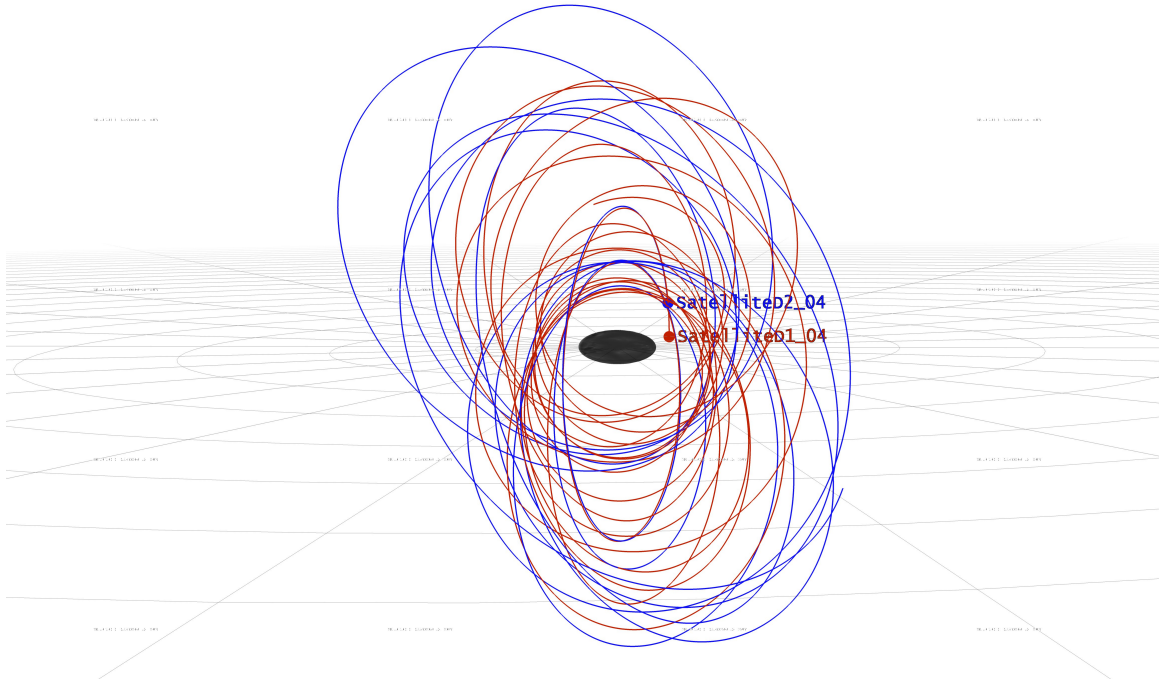
Figure 40: SatelliteD1_04 and SatelliteD2_04 Orbit Visualization

This figure shows a 3-dimensional plot of the trajectories for SatelliteD1_04 and SatelliteD2_04 over the entire simulation. While the two spacecraft follow roughly the same trajectory over the first few orbits, the trajectories diverge significantly throughout the simulation.

Similar behavior is seen in Figure 27 and Figure 36 where the LOS ranges display

large fluctuations, which exceed 1 km. The interpretation is that these trajectories remain

bound and do not impact Itokawa. They are however, perturbed significantly from their

initial state. The ultimate result is a divergence between the two trajectories, which is not

conducive for SST.

Another characteristic observed in the range and range-rate plots is an exponential

growth in both variables. This behavior occurs when one or both of the two spacecraft

either impact the asteroid or enter an escape trajectory form the system. For example,

Figure 31 displays this behavior with the range and range-rate increasing exponentially by the end of the third day. Figure 41 shows the 3-dimensional trajectories for SatellitesD1_05 and SatelliteD2_05. Both spacecraft impact the surface of Itokawa after only a few orbits as indicated by the exponential growth of the range and range-rate seen in Figure 31.
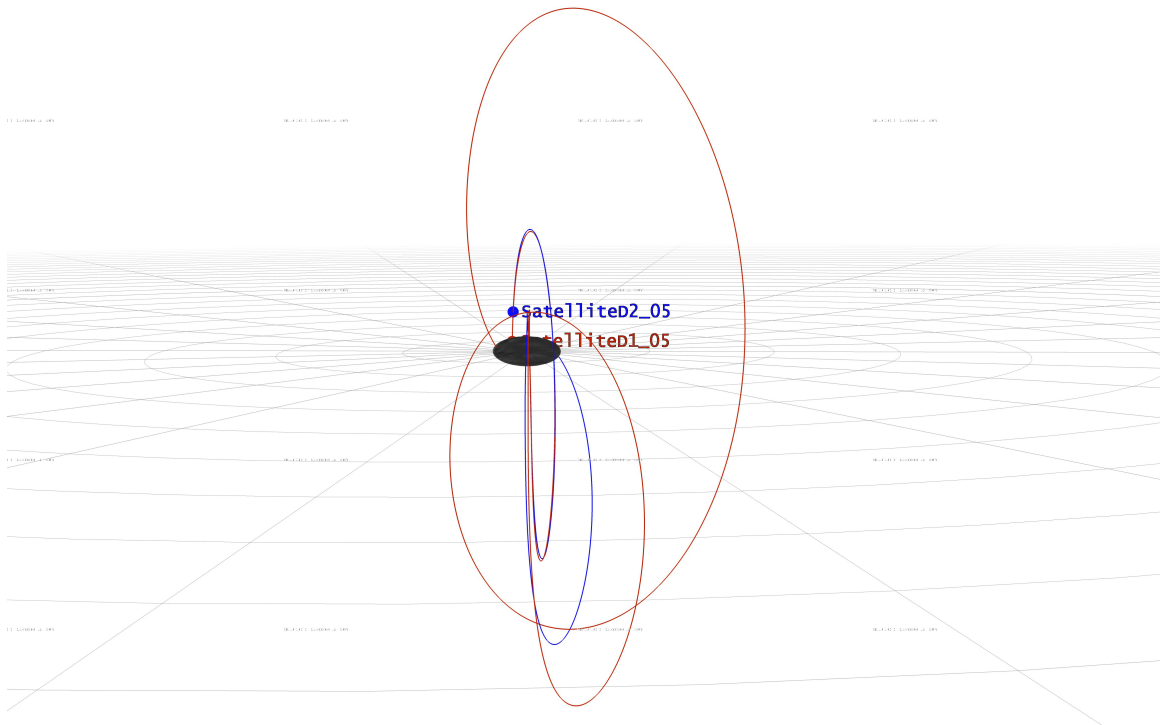
Figure 41: SatelliteD1_05 and SatelliteD2_05 Orbit Visualization

The trajectories of SatelliteD1_05 and SatelliteD2_05 are shown. SatelliteD2_05 impacts the asteroid's surface after the first orbit. SatelliteD1_05 impacts after approximately 3 orbits.

Similar exponential growth in the range and range-rate is observed in Figure 32, Figure 33, Figure 37, and Figure 38. This indicates that at least one of the two spacecraft impacts Itokawa or is ejected from the system. The magnitudes observed for both the range and range rate observed in these figures are suggestive that large variations in orbital trajectories exist.

Figure 42. Range and Range-Rate Plot for SatelliteE1_01 to SatelliteE2_01

The LOS range and range-rate between SatelliteE1_01 and SatelliteE2_01 begins to vary by more than 500 m by the second day of observations. By the end of the observation window, both quantities begin to increase exponentially.

Figure 43. Range and Range-Rate Plot for SatelliteE1_02 to SatelliteE2_02

The LOS range between SatelliteE1_02 and SatelliteE2_02 varies by roughly ±100 m over the first day. By the second day the separation between the two craft exceeds 1 km.

108

The separation continues to vary widely for the remainder of the observation period. These wide fluctuations in LOS range over the short time are accompanied by LOS range-rates on the order of cm/sec.
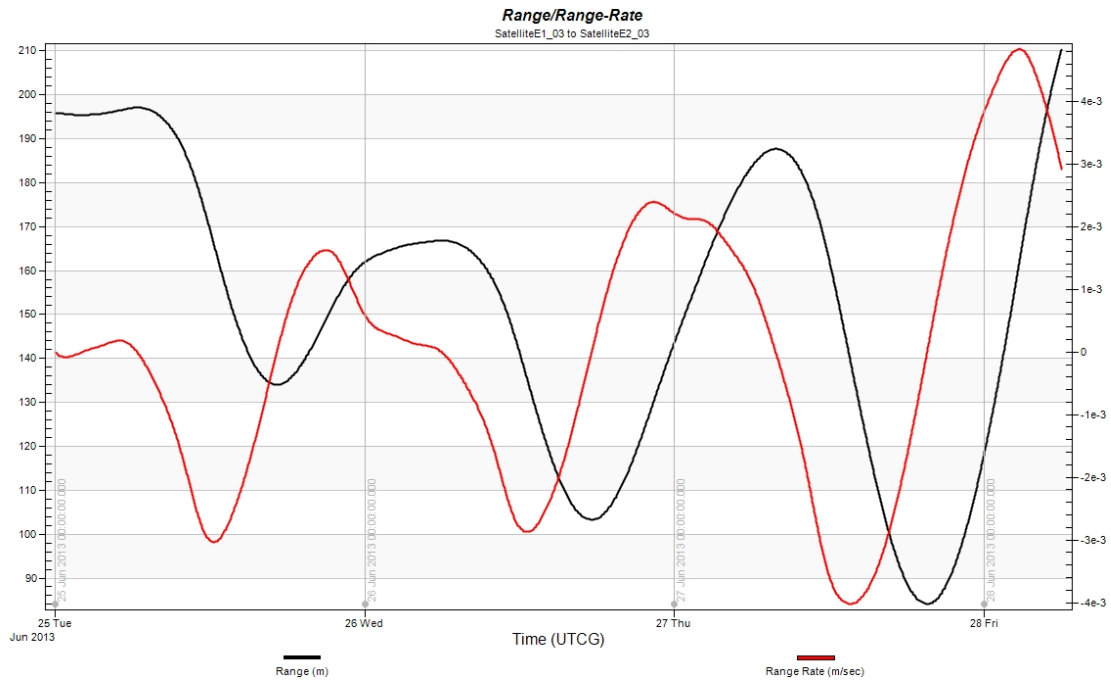
Figure 44. Range and Range-Rate Plot for SatelliteE1_03 to SatelliteE2_03

The LOS range and range-rate plots for SatelliteE1_03 and SatelliteE2_03 display more stability with the range varying by approximately 130 m over the period of observation while the range-rate remains on the order of 10^{-3} m/sec. The overall trend in LOS range appears periodic with continually increasing amplitude.

Figure 45. Range and Range-Rate Plot for SatelliteE1_04 to SatelliteE2_04

The LOS range between SatelliteE1_04 and SatelliteE2_04 remains less than 200 m for the first two days of observations. After the second day however, the distance between the two spacecraft quickly approaches 1 km. This results in correspondingly high range-rate measurements that reach a few cm/sec.
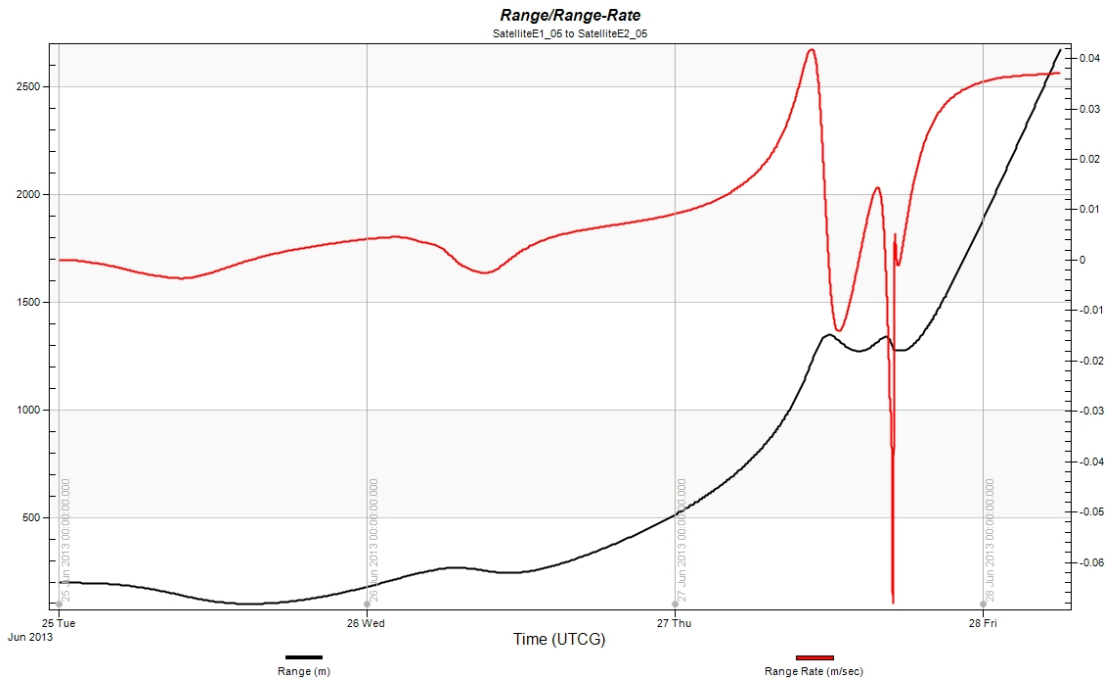
Figure 46. Range and Range-Rate Plot for SatelliteE1_05 to SatelliteE2_05

The overall trend in LOS range between SatelliteE1_05 and SatelliteE2_05 is a continual increase, which exceeds 2.6 km after the third day.

Figure 47. Range and Range-Rate Plot for SatelliteE1_06 to SatelliteE2_06

The trend for the LOS range and range-rate for SatelliteE1_06 and SatelliteE2_06 is similar to the previous pair exhibiting a nearly continual increase in separation over the observation period with some spikes in the LOS velocity.
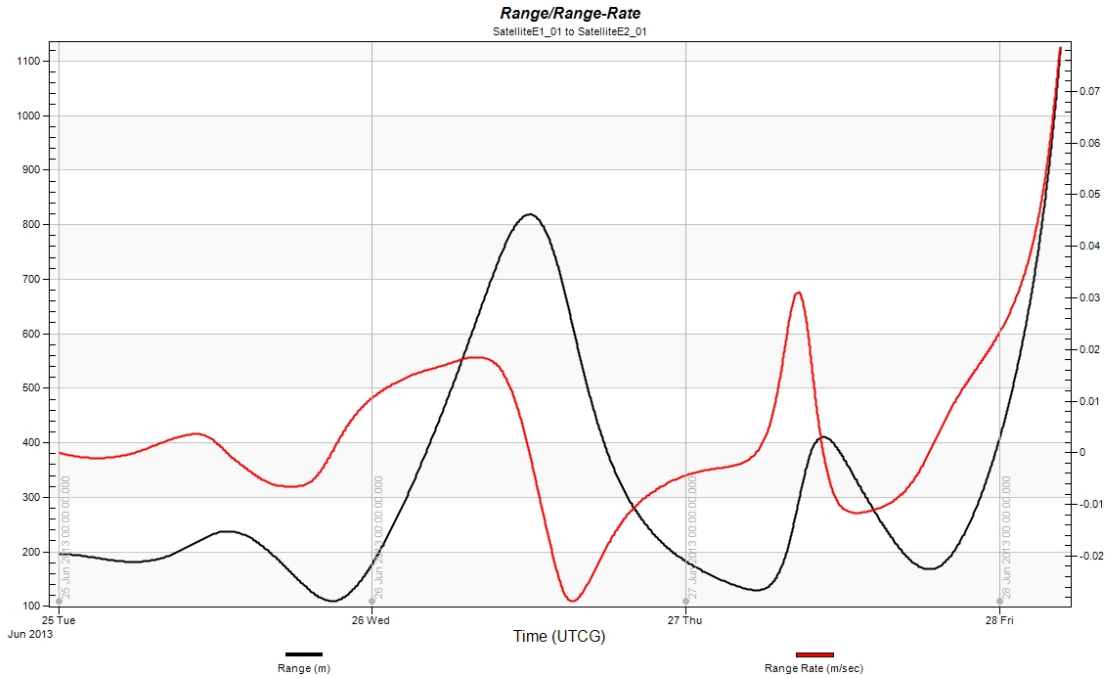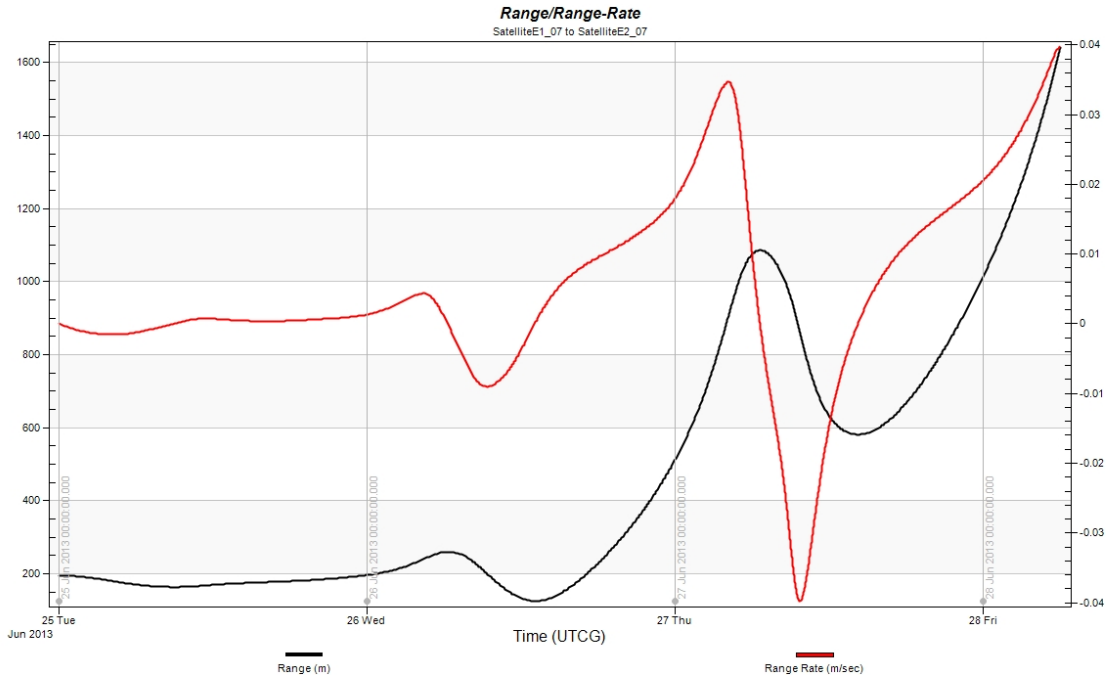
Figure 48. Range and Range-Rate Plot for SatelliteE1_07 to SatelliteE2_07

The LOS range between SatelliteE1_07 and SatelliteE2_07 remains stable for the first day prior to increasing rapidly. By the end of the observation period, the separation exceed 1.5 km while the range-rate reaches 10^{-2} m/sec.
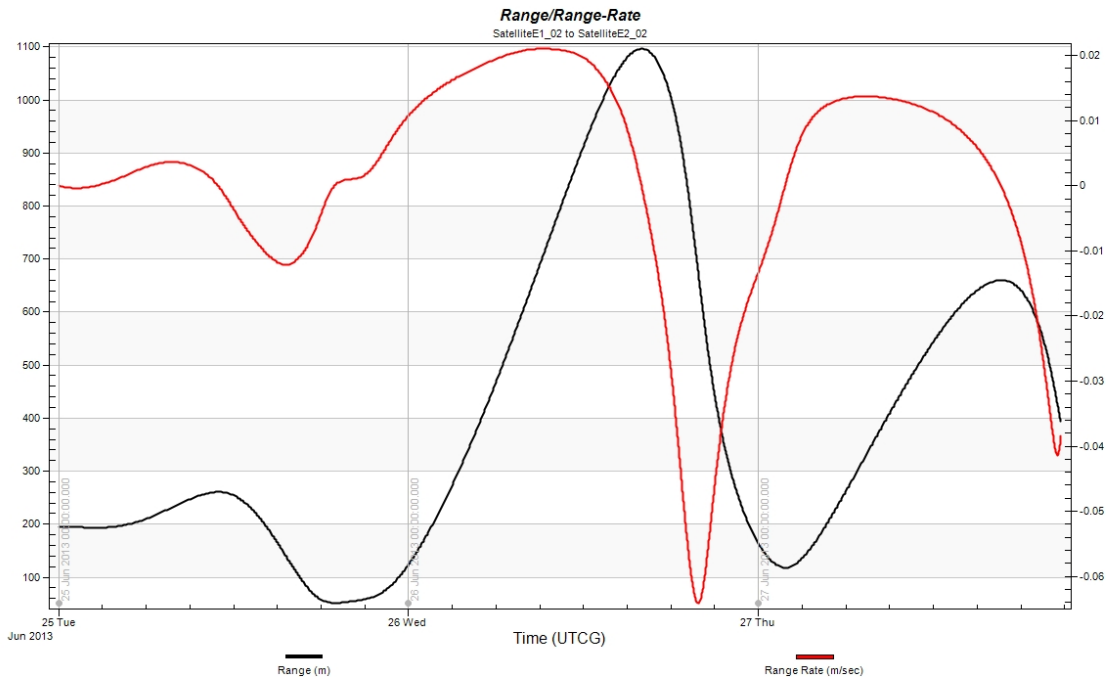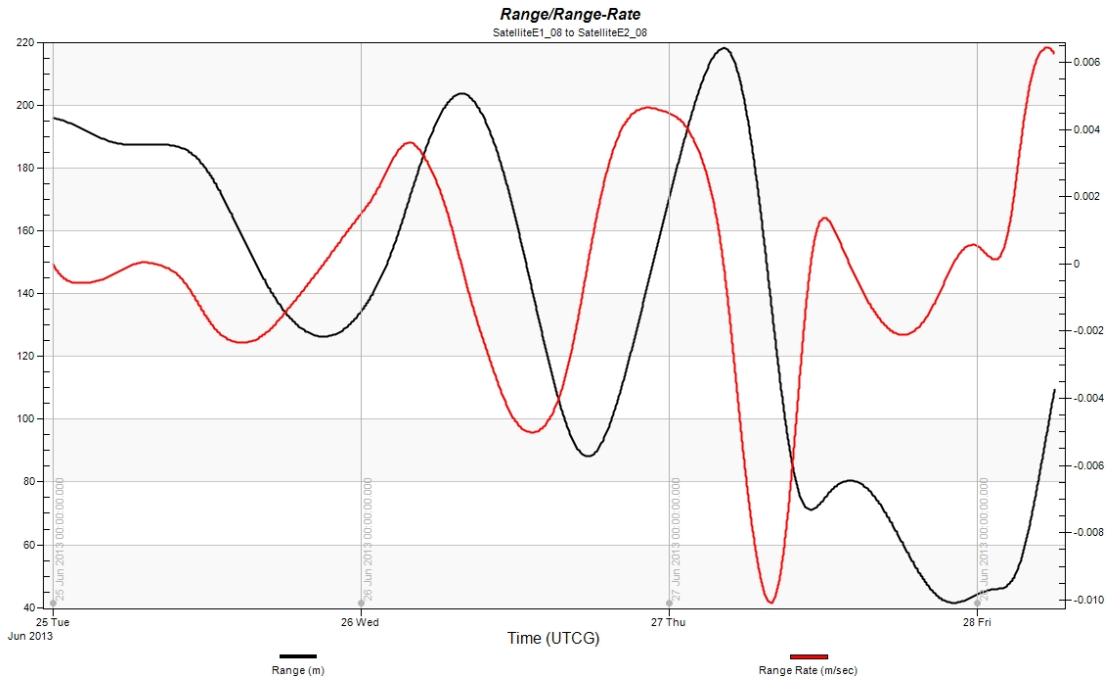

Figure 49. Range and Range-Rate Plot for SatelliteE1_08 to SatelliteE2_08

*The LOS range between SatelliteE1_08 and SatelliteE2_08 varies by only 180 m.
However, several of the variations occur quickly due to range-rates reaching 10^{-2} m/sec.
In particular the there is a rapid decrease in separation that occurs a few hours into the
third day of observation.*
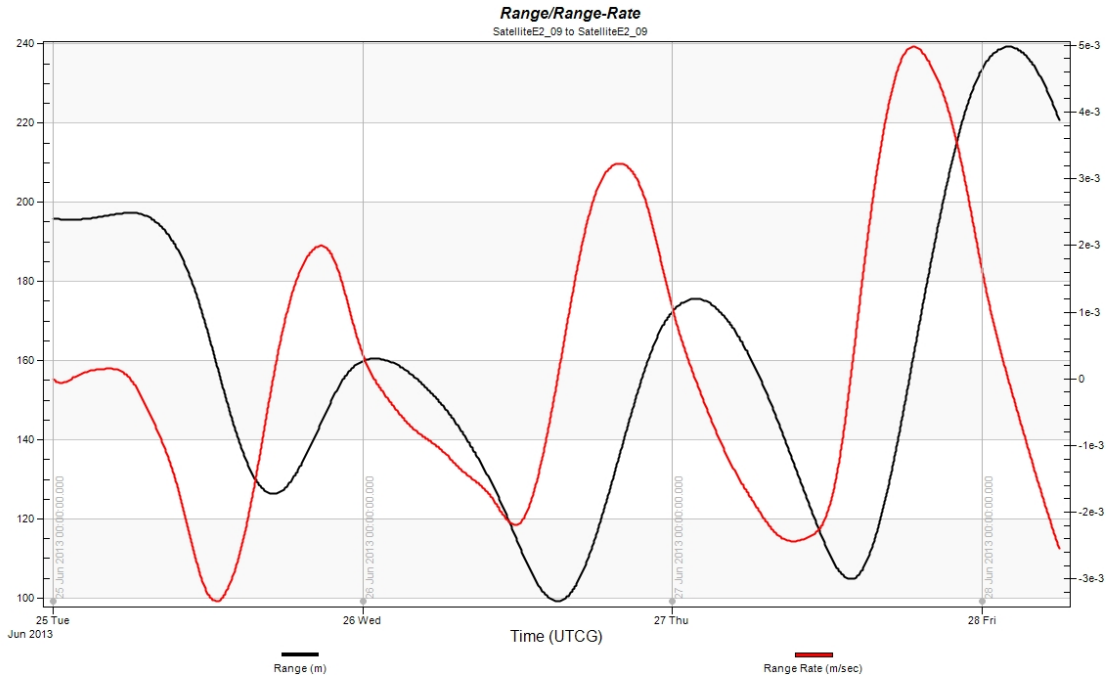
Figure 50. Range and Range-Rate Plot for SatelliteE1_09 to SatelliteE2_09

*The LOS range between SatelliteE1_09 and SatelliteE2_09 stays within ±100 m over the
observation window and the relative velocity between the two spacecraft is on the order
of 10^{-3} m/sec. The relatively small changes in LOS range between the two spacecraft are
indicative of overall orbit stability.*
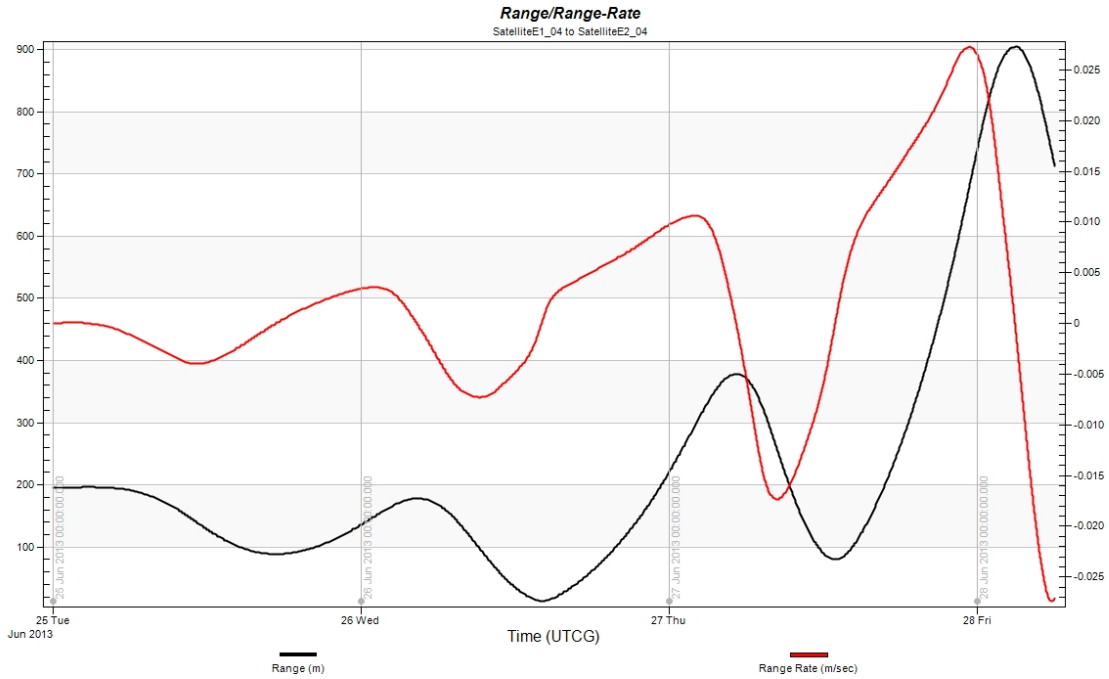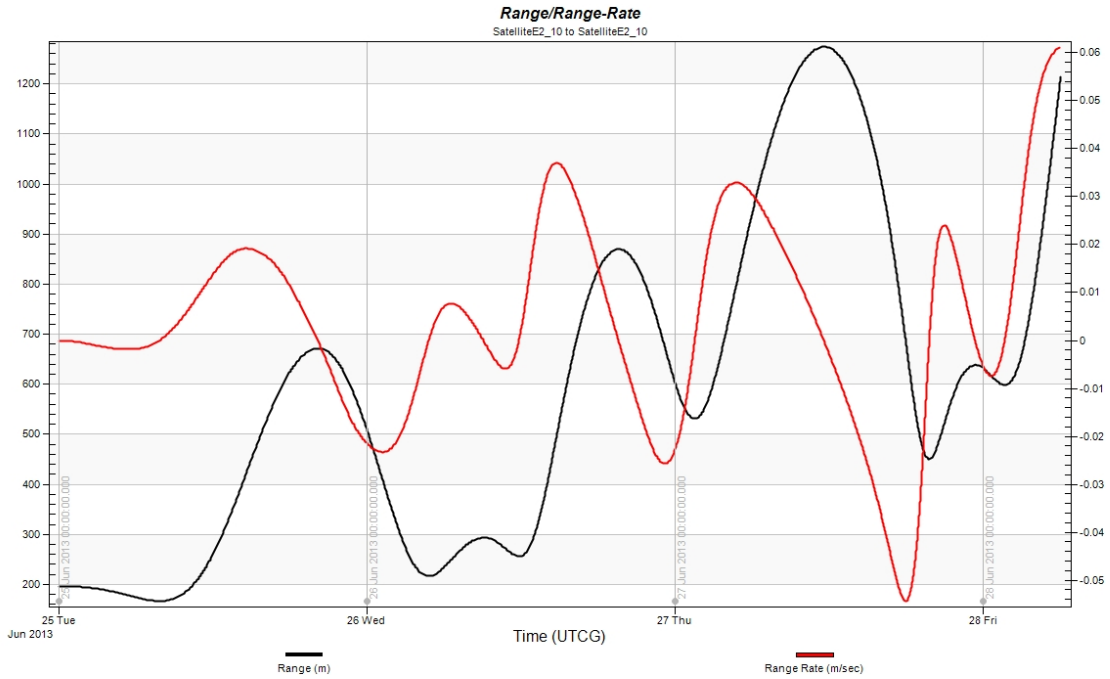
Figure 51. Range and Range-Rate Plot for SatelliteE1_10 to SatelliteE2_10

The trajectories for SatelliteE1_10 and SatelliteE2_10 diverge quickly with their relative separation exceeding 500 m in the first 24 hours. The range-rate varies by $\pm 3 \times 10^{-2}$ m/sec for most of the observation period. At some points the range-rate reaches $\pm 5 \times 10^{-2}$ m/sec.
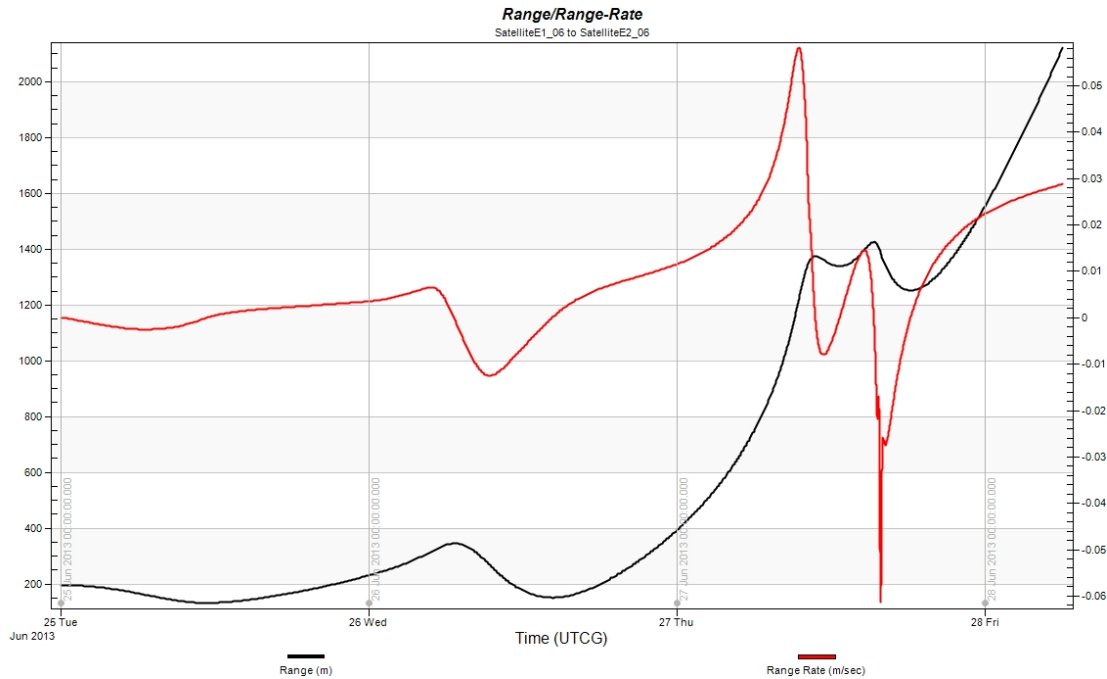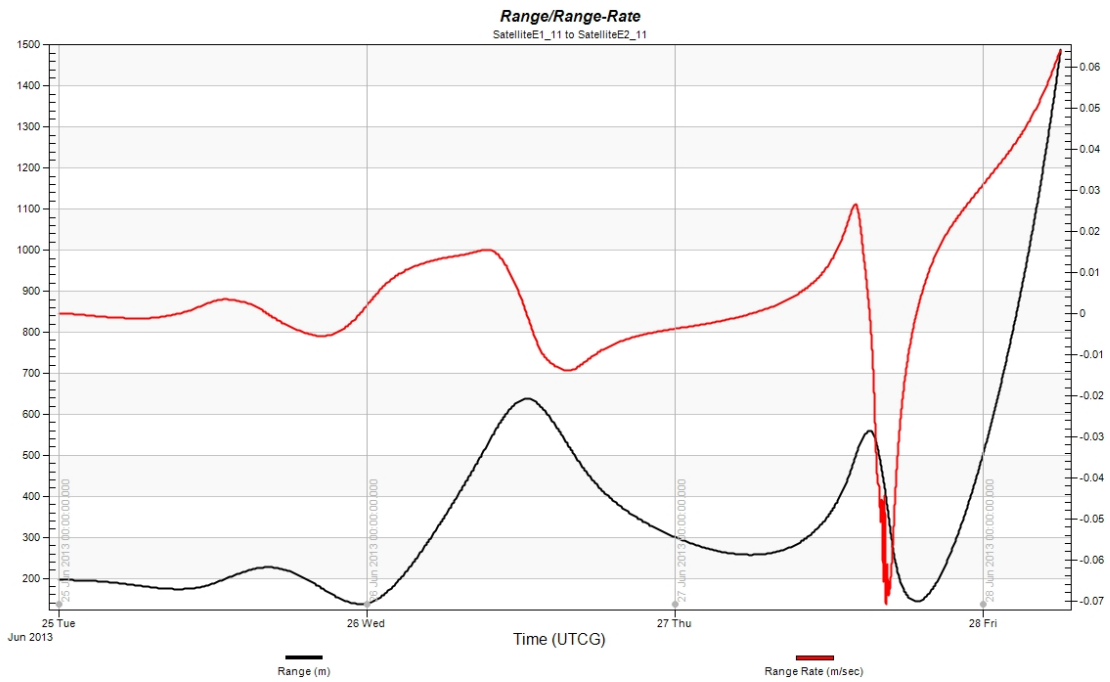

Figure 52. Range and Range-Rate Plot for SatelliteE1_11 to SatelliteE2_11

114

*The LOS range and range-rate between SatelliteE1_11 and SatelliteE2_11 remain
relatively small for the first day of observation. After this however, the range-rate
increases to several cm/sec resulting in large variations in the separation of the two
spacecraft. By the third day, the range-rate is continually increasing and the range
begins to increase exponentially.*
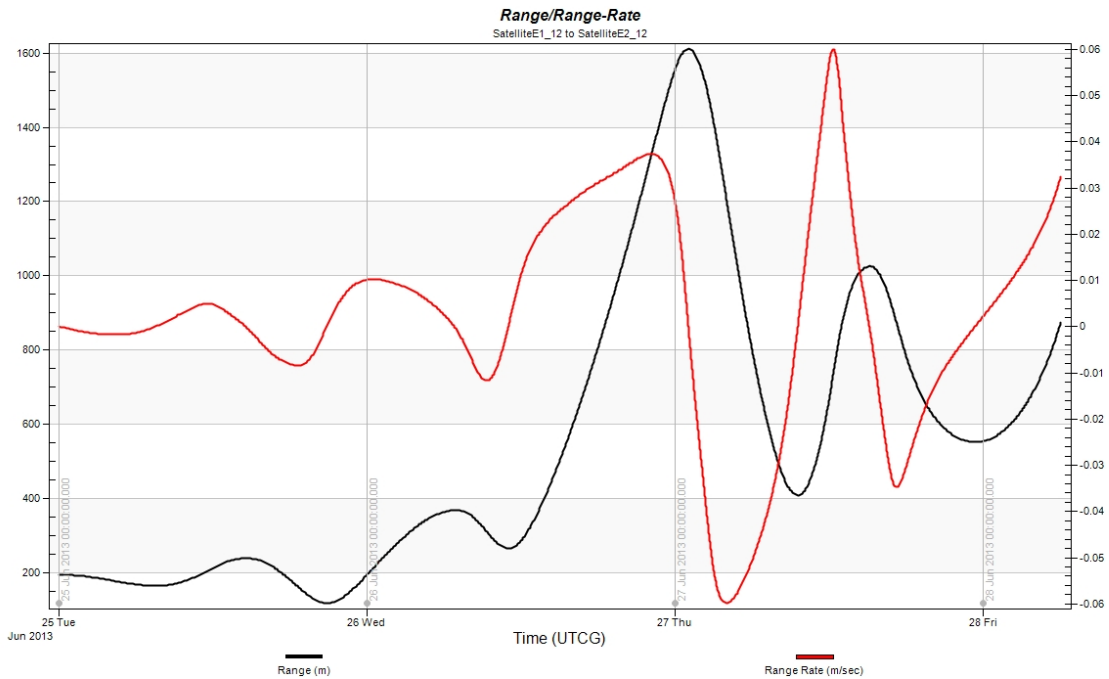
Figure 53. Range and Range-Rate Plot for SatelliteE1_12 to SatelliteE2_12

*This figure reveals large variations in the range and range-rate between SatelliteE1_12
and SatelliteE2_12. After two days the separation between the two spacecraft exceeds
1.5 km with the corresponding range-rates reaching $\pm 6 \times 10^{-2}$ m/sec.*

The range and range-rate plots shown Figure 42 through Figure 53 are assessed in
the same manner as those in Figure 27 through Figure 38. Small variations in the LOS
separation and velocity indicate relative stability between the trajectories of the two
spacecraft. Large periodic variations in these properties represent a divergence between
the two trajectories. Exponential growth is interpreted as one or both of the spacecraft
impacting the asteroid or being ejected from the system.

Figure 44, Figure 49, and Figure 50 exhibit small variations in the range and
range-rate throughout the entire observation window. These small variations represent

stability between the trajectories. The range and range-rate plots shown in Figure 43 and Figure 45 display large periodic changes of approximately 1 km in separation and 10^{-2} m/s in LOS velocity.   The remaining plots in this series all show exponential growth in the LOS range and range-rate. In each of these cases, one or both of the spacecraft impact the surface of Itokawa or are ejected from the system.

Despite the significant variations observed between Figure 27 through Figure 38 and Figure 42 through Figure 53, large divergences between the trajectories for each pair of spacecraft are not seen until after 24 hours. While large divergence between trajectories is the result of variations in Itokawa's gravity field and SRP, the rapid changes observed in many of the range and range-rate plots not desirable.   These rapid changes are associated with diverging trajectories, which conflicts with the assumption that the two spacecraft are in approximately the same orbit. However, since this divergence doesn't begin until after the first 24 hours, data collection is still possible during this period of relative stability.

It should be noted that the analysis techniques used to evaluate the range and range-rate plots does not represent an assessment of the relative stability between trajectories outside of the plot times. In some cases, trajectories deemed stable by this analysis ultimately diverge over time. However, since this analysis is not concerned with long-term stability in excess of the times established in the previous section, the conclusions made from this analysis are not conflicting.

CHAPTER VII.

DISCUSSION

There are two main points of interest in the comparison between the systems

analysis conducted for GRACE and GRAIL and the data obtained from the STK

simulation. One is how the measurement capabilities of the hardware employed on the

GRACE and GRAIL missions compare to the simulated data. The other is how the orbit

trajectories maintained during the missions compare to those used for the simulation.

The goal of the proceeding analysis is to, first determine whether or not the technique of

SST can be applied to two spacecraft in orbit around a small NEO based on the

measurement capabilities demonstrated by actual missions. Second, a preliminary set of

parameters that will govern the orbital requirements for SST data collection around a

small NEO will be established.

Systems Analysis Comparison

The results of the range and range-rate analysis above reveal two distinct cases.

The first of these is a short period of stability in both the LOS range and range-rate

changes between the two spacecraft. This is followed by a rapid increase in the

magnitude and rate of change for these properties. With the second case, the same initial

stability is observed but unlike the first case, it is followed by continued stability. These

behaviors are observed in the orbits of both groups of satellites, Satellites D and Satellites

E.

The range-rate observed for each pair of spacecraft varies between $\pm 10^{-5}$ m/s at its lowest to nearly 0.1 m/s at its highest. The higher range-rates tend to be associated with excessive divergence of the two spacecraft while the lower values tend to exist when the two spacecraft occupy nearly the same orbit as dictated by the principles of SST. These are the conditions during which the changes in LOS position and velocity need to be measured.

Comparing the low-end range-rate of $\pm 10^{-5}$ m/s to the measurement capabilities of GRACE and GRAIL is favorable. GRACE measures changes in range and range-rate on the order of 10×10^{-6} m and 10×10^{-6} m/s respectively. The GRAIL spacecraft were originally required to be capable of discerning position and velocity changes on the order of 1×10^{-6} m and 1×10^{-6} m/sec respectively. The system's actual performance was 10 times better at 1×10^{-7} m and 1×10^{-7} m/s. In each case, the hardware is able to resolve changes an order of magnitude smaller than smallest sustained changes observed in the simulations. This confirms that under the conditions used in the simulations, range and range rate between two spacecraft in orbit around a small NEO would be discernable using existing technology. However, it is important to note that the measurements considered here include the effects of non-conservative forces such as SRP. These effects would need to be removed from the data during processing. In the case of the range and range-rate for SatelliteD1_03 to SatelliteD2_03 shown in Figure 29, the range rate was on the order of 10^{-5} m/s. Removing the effects of SRP from these data results in a range-rate on the order of 10^{-4} m/s as shown in Figure 54.
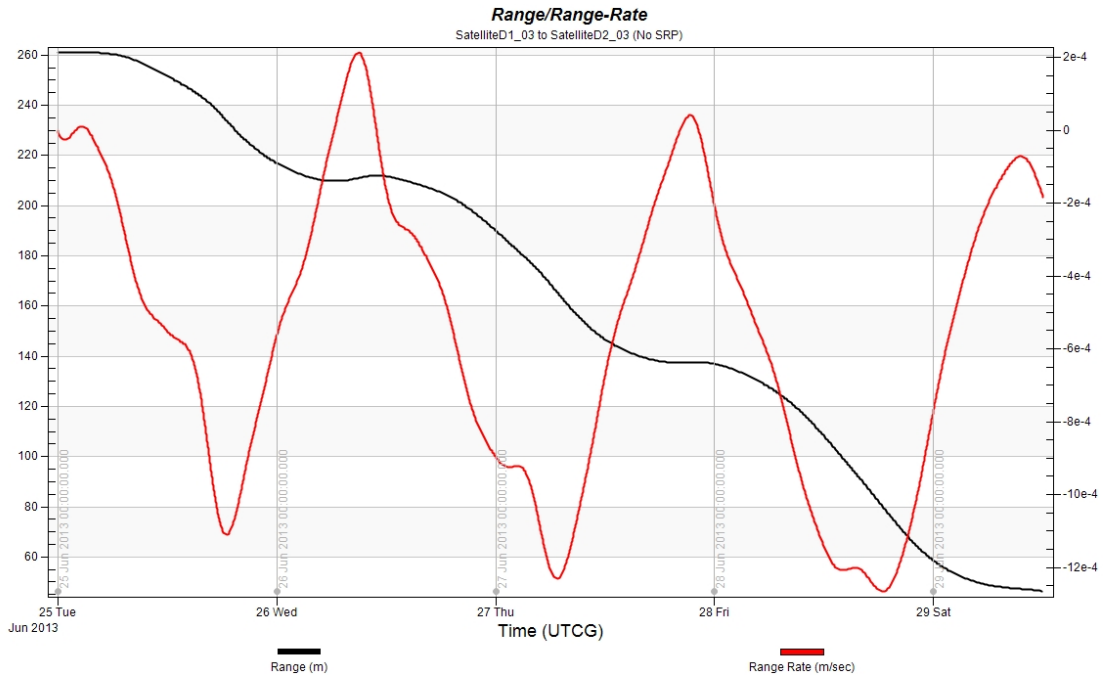
Figure 54. Range and Range-Rate for SatelliteD1_03 to SatelliteD2_03 Without SRP

This figure shows the range and range-rate between SatelliteD1_03 and SatelliteD2_03
as a function of time when the effects of SRP are neglected. The resulting LOS velocities
are on the order of 10^{-4} m/s and the LOS distance spans a range of 200 m.

A comparison of the results shown in Figure 29 with those shown in Figure 54

show that the LOS velocity between spacecraft when SRP is included is actually lower

than when it is neglected. This is caused by the fact that as a spacecraft orbits the NEO

the direction of the gravitational forces and SRP varies. This illustrates the need to

account for these non non-conservative forces when employing SST. This can be

achieved through measurement, as it was with GRACE or modeling similar to GRAIL.

Orbit Requirements

As Figure 3, Figure 4, and Figure 5 show, the orbits of the GRACE satellites are

very stable compared to the data seen in the simulations.   Similar stability can be seen in

the GRAIL mission from the data in Table 3. The simulated data is comparatively less

stable than either of these missions. This was expected due to the strongly perturbed

119

environment coupled with the fact that orbit controls were not implemented in the simulation. Such corrective maneuvers will be a requirement for data collection. These will need to be executed autonomously because of the dynamics of the environment and the communication delays that are expected with NEO missions. Such an autonomous control system is currently being developed at the University of North Dakota (Zimmer et al., 2014). A control system capable of executing such maneuvers however, will require conditions under which such maneuvers should be executed. The results of this work have established a preliminary set of such conditions.

The combined results from the analysis used to establish data collection times and the subsequent range and range-rate analysis indicate that orbit correction maneuvers should be executed with a frequency of no less than once every 24 hours. This conclusion is based on the analysis conducted to establish SST data collection times and the changes observed in the LOS range and range-rate data. In nearly all of the simulations conducted, after 3-days the changes in a spacecraft's trajectory began to diverge rapidly. When extended to a pair of spacecraft, these conditions create a situation where at least one of the two spacecraft was no longer in a circular, near polar orbit coplanar with the other spacecraft. Such conditions violate the principles behind SST.

When examining the range and range-rate data, the trajectories of the two spacecraft begin to diverge rapidly after approximately 24 hours. This observation further tightens the requirements for orbit correction maneuvers. Based on this analysis, performing correcting maneuvers at least once every 24 hours would prevent this divergence from occurring. In some cases corrections may need to be made more frequently.

A threshold of ±5° in inclination change was used to determine a range and range

rate data collection window used here. This limit was reached for most trajectories in

only a few days. Based on the analysis of the GRACE and GRAIL missions, the orbit

inclination will need to be controlled more accurately than ±5° from its initial value. An

autonomous control system should monitor and maintain the orbit inclination for both

spacecraft while maintaining a difference in inclinations between the two trajectories of

less than 1°. Eccentricities should be maintained near 0 so that the orbits are near circular.

Such requirements are commensurate with the limits observed for the GRACE and

GRAIL missions. Table 13 summarizes the differences between the orbit parameters

used in the STK simulation and those from the GRACE and GRAIL analysis. This table

also includes a comparison of the simulated range and range-rate measurements with the

actual accuracies obtainable using hardware from the GRACE and GRAIL missions.

Table 13. Parameter Comparison

This table summarizes the comparison between the orbit parameters used for the STK
simulation and those employed on the GRACE and GRAIL missions.

Parameter	STK Simulation	GRACE	GRAIL
Inclination	91±5°	~89°±1°	89.2°±1.2°
Inclination Difference	< 1°	< .0001°	< .0001°
Eccentricity	~ 0	$0-10^{-3}$	$0-0.02$
Range Accuracy	10^{-5} m (required)	10^{-6} m (actual)	10^{-7} m (actual)
Range-Rate Accuracy	10^{-5} m/s (required)	10^{-6} m/s (actual)	10^{-7} m/s (actual)

The mean orbital period for a circular, unperturbed orbit with a radius of 1000 m

is 35.927 hr and 23.335 hr for the same orbit with a radius of 750 m. In the case of

Itokawa, the asteroid would rotate nearly twice for the 750 m orbit and 3-times for the

1000 m orbit.   Each of these orbital radii results in an orbital period approximately equal

to an integer number of asteroid rotations as defined by Equation (12). Based on this, the orbital radii for the pair of spacecraft could drift by several hundred meters between 750 m and 1000 m while still maintaining an optimal number of asteroid rotations per orbital period.

The analysis discussed above has concluded that SST around a small NEO will produce measurable range and range-rate data provided that the preliminary orbit requirements established in this work are met. These requirements are given in Table 14.

Table 14. Preliminary Orbit Requirements

This table presents the preliminary set of orbit requirements for executing SST around a small NEO.

Parameter	Requirement
Inclination	~91±5°
Inclination Difference	< 1°
Eccentricity	~ 0
Orbit Radius	750 m to 1000 m⁻
Corrective Maneuver Frequency	Minimum 1/day

While this work has shown that the use of SST in a low-low configuration around a small NEO should be possible, it has not addressed the potential resolution attainable for the gravity model resulting from these data. Successful execution of a low-low SST mission will require the use of autonomous spacecraft control and detailed measurements (or modeling) of the non-conservative forces acting on the spacecraft. Such measurements could be accommodated by the inclusion of accelerometers onboard the spacecraft. A preliminary set of mission parameters has been presented, which will serve as a basis for further investigations into the development of both mission requirements

for examining internal structure via gravity field mapping and autonomous spacecraft control systems.

Future Work

While this thesis has shown that the use of low-low SST in the small NEO environment should be able to produce measurable data under the conditions set forth here, it does not suggest that this technique is the optimal in situ method for mapping the gravity field for this type of object. SST is one means by which the gravitational field of a small NEO might be mapped. Other techniques such a space borne gravity gradiometer similar to that used on the GOCE spacecraft, or even surface gradiometers may prove more effective in the small NEO environment. In either case, the requirements for executing these techniques will require spacecraft operations in close proximity to the NEO.

In addition to considering the implementation of SST around a small NEO, this work has developed a tool that can be used to explore mission concepts that require operation in close proximity to the NEO. While the simulation developed utilized the properties of asteroid 21543 Itokawa to create the central body, it is flexible and can easily be adapted to utilize the properties of a different asteroid. It is also possible incorporate a model of a yet unknown asteroid for which the properties are arbitrarily derived. Therefore, this tool can be used to conduct additional dynamical studies around a variety of objects by modifying the central body properties to create alternative environments.

The usefulness of this tool was recently demonstrated after a conversation with Mark Sykes on March 20, 2014 led to an alternate mission concept that could potentially

be used to map the gravity field of a small NEO. This concept would use a primary spacecraft to deploy a number of smaller, uncontrolled sub-spacecraft. The primary spacecraft would precisely track these sub-spacecraft yielding information on the gravitational environment around the NEO. The work presented here allowed preliminary investigations into this concept to be conducted quickly. By utilizing the STK environment developed here, this alternative concept was simulated using a primary spacecraft and two sub-spacecraft. The resulting simulation served to verify the concept and ultimately inspired further development of the idea. This concept represents one of many possibilities for future work in the area of gravity mapping and investigating the internal structure of small NEO.

APPENDIX

STK Simulation Files

Itokawa.cb

```
BEGIN              CentralBody

    Name                    Itokawa
    Prefix                  Astero
    ShortDescription        Asteroid
    Description             Asteroid
    Type                    Asteroid
    FuncCbInit              AsterInit
    FuncCbFree              PlanetFree
    FuncCbLoad              PlanetLoad
    FuncCbSave              PlanetSave
    FuncCbCopy              PlanetCopy
    FuncCbSet               PlanetSet


BEGIN              AstroDefinition
    Gm              2.36
    RefDistance     161.9150859
    MinRadius       104.5
    MaxAltitude         0.00000000000000e+000

    GravityModel        ItokawaGrv

    Shape               TriaxialEllipsoid

    MajorAxis           277.9
    MiddleAxis          151.35
    MinorAxis           121.5

    ParentName          Sun

    PathGenerator       GreatArc
    PathGenerator       J2Perturbation
    PathGenerator       J4Perturbation
    PathGenerator       Rocket
    PathGenerator       TwoBody
    PathGenerator       StkExternal
    PathGenerator       Astrogator
    PathGenerator        SPICE
    PathGenerator         HoldCBIPosition
```

```
PathGenerator            HoldCBFPosition
PathGenerator            HPOP


END                      AstroDefinition


BEGIN                    SpinData
    RotationDefinitionFile      ItokawaAttitude2000.rot
END                      SpinData


BEGIN        EphemerisData
    EphemerisSource          JplSpice
    JplIndex                 -1
    JplSpiceId               202514
END                      EphemerisData


BEGIN        Itokawa

END          Itokawa


    ReadOnly              No

END                      CentralBody



                    ItokawaGrvScheeres.grv


stk.v.4.0


Model          ItokawaGrv
CentralBody        Itokawa


Degree          12
Order           12


Gm          2.36
RefDistance      161.9150859


Normalized      Yes
# Source - Dr. Daniel Scheeres, personal communication 6/5/2013


# 0 0   1.000000000E+00      0.000000000e00
# 1 1   1.461195065E-14      2.370523004E-12
# 1 0   -1.534335106E-12     0.000000000e00


BEGIN Coefficients
```

2	0	-1.452160768e-01	0.000000000e00
3	0	3.611474708e-02	0.000000000e00
4	0	8.785251185e-02	0.000000000e00
5	0	-6.602375017e-02	0.000000000e00
6	0	-6.431630206e-02	0.000000000e00
7	0	1.077970258e-01	0.000000000e00
8	0	2.507252409e-02	0.000000000e00
9	0	-1.563793306e-01	0.000000000e00
10	0	6.230503503e-02	0.000000000e00
11	0	1.796984720e-01	0.000000000e00
12	0	-2.213556990e-01	0.000000000e00
2	1	1.524222282e-12	-3.573992248e-13
2	2	2.194205011e-01	4.598252992e-12
3	1	-2.813916144e-02	-6.136925676e-03
3	2	-4.689404935e-02	-1.179643094e-02
3	3	6.902225436e-02	3.397597184e-02
4	1	3.406934239e-02	4.869945484e-03
4	2	-1.232631492e-01	9.795730731e-05
4	3	-3.067321356e-02	-1.502588532e-02
4	4	1.502819876e-01	1.162738947e-02
5	1	3.247783490e-02	6.391076476e-03
5	2	8.903382732e-02	1.584332764e-02
5	3	-5.706652250e-02	-2.423977214e-02
5	4	-7.405165012e-02	-2.690402686e-02
5	5	1.150998115e-01	5.933678261e-02
6	1	-8.245602513e-02	-9.421580695e-03
6	2	9.147685415e-02	-6.388877783e-03
6	3	8.007845548e-02	2.849107068e-02
6	4	-1.000217163e-01	1.365751595e-03
6	5	-6.915124969e-02	-4.334189582e-02
6	6	1.449263345e-01	3.995152659e-02
7	1	-9.615806644e-03	-2.669606904e-03
7	2	-1.486553349e-01	-2.158707627e-02
7	3	3.457040140e-02	1.178862218e-02
7	4	1.359485266e-01	4.368730023e-02
7	5	-8.131810172e-02	-3.266056959e-02
7	6	-1.082384996e-01	-6.414363972e-02
7	7	1.695547066e-01	9.553459019e-02
8	1	1.444826356e-01	1.423055839e-02
8	2	-3.868517080e-02	2.282790158e-02
8	3	-1.475385914e-01	-4.463037581e-02
8	4	5.232230139e-02	-3.213954948e-02
8	5	1.464014105e-01	7.739209104e-02
8	6	-8.465782190e-02	8.289274453e-03
8	7	-1.270705080e-01	-1.033042418e-01
8	8	1.630982362e-01	9.646630023e-02

9	1	-7.032114496e-02	-7.705696323e-03
9	2	2.199623466e-01	2.340122174e-02
9	3	3.958505238e-02	1.928839292e-02
9	4	-2.141146640e-01	-5.574773180e-02
9	5	1.866066067e-02	-1.714914642e-02
9	6	1.962216876e-01	1.021960261e-01
9	7	-1.017271957e-01	-2.009790644e-02
9	8	-1.535651619e-01	-1.505103215e-01
9	9	2.369512539e-01	1.610687013e-01
10	1	-1.958629568e-01	-1.444374601e-02
10	2	-8.156922005e-02	-5.624669344e-02
10	3	2.130388233e-01	4.965925000e-02
10	4	5.774364689e-02	9.831641156e-02
10	5	-2.360093708e-01	-1.007105221e-01
10	6	-8.367015189e-03	-1.042950607e-01
10	7	2.437890987e-01	1.678328443e-01
10	8	-7.174280746e-02	3.687029147e-02
10	9	-2.078758904e-01	-2.283323027e-01
10	10	1.991331430e-01	2.127996651e-01
11	1	2.450121220e-01	2.767110943e-02
11	2	-2.605017716e-01	-2.258133903e-03
11	3	-2.082957741e-01	-8.088636718e-02
11	4	2.758748562e-01	2.903410047e-02
11	5	1.339736965e-01	1.226365635e-01
11	6	-2.877307138e-01	-1.001054315e-01
11	7	-2.231393688e-02	-1.271240161e-01
11	8	2.741402474e-01	2.186120061e-01
11	9	-1.218136290e-01	4.030001524e-02
11	10	-2.077021450e-01	-3.442980509e-01
11	11	3.203410165e-01	2.887293589e-01
12	1	1.568911244e-01	-4.338658733e-03
12	2	3.059804503e-01	1.077207471e-01
12	3	-2.055417273e-01	-1.678466709e-03
12	4	-2.769224481e-01	-2.092077074e-01
12	5	2.849975335e-01	4.948569619e-02
12	6	2.081714974e-01	2.837839116e-01
12	7	-3.598595719e-01	-1.578673598e-01
12	8	-8.709549860e-02	-2.846735288e-01
12	9	3.811175008e-01	3.240786212e-01
12	10	-7.467830121e-02	1.227873763e-01
12	11	-3.006410243e-01	-4.900976480e-01
12	12	2.480757978e-01	4.573924272e-01

END Coefficients

ItokawaAttitude2000.rot

From "Report of the IAU/IAG Working Group on Cartographic Coordinates and
Rotational Elements of the Planets and satellites: 2000",
Celestial Mechanics 82: 83-110, 2002.

BEGIN RotationalData
        ModelName   IAU 2000
        Description   Coefficients from the IAU 2000 parameter set

        RotationEpoch   2453137.5

Rotational Axis Source: Demura et. al, 2006 - Pole and Global shape of 25143 Itokawa

Pole Longitude relative to Earth ecliptic
        Begin RotationalElement
                Type   SpinAxisRightAscension
                Constant   90.53000000000000
                Rate   -0.00000000000000
                RateDot   0.0
                NumberOfTerms   0
        End RotationalElement

Pole Latitude relative to Earth ecliptic
        Begin RotationalElement
                Type   SpinAxisDeclination
                Constant   -66.3000000000000
                Rate   -0.000000000000000
                RateDot   0.0
                NumberOfTerms   0
        End RotationalElement

Rotational rate in minutes based on JPL ephemeris data available at
telnet://horizons.jpl.nasa.gov:6775
Rotational rate provided in hours of 12.132 hours converted to degrees per day.
        Begin RotationalElement
                Type   Rotation
                Constant   0.00000000000
                Rate   -712.16
                RateDot   0.0
                NumberOfTerms   0
        End RotationalElement

END RotationalData

REFERENCES

Asmar, S., Konopliv, A., Watkins, M., Williams, J., Park, R., Kruizinga, G., . . . Zuber, M. (2013). The scientific measurement system of the gravity recovery and interior laboratory (GRAIL) mission. *Space Science Reviews, 178*(1), 25-55. doi:10.1007/s11214-013-9962-0

Benner, L. (2013a). Asteroid 3-D shape models estimated from delay-doppler radar data. Retrieved March, 14, 2014, from http://echo.jpl.nasa.gov/~lance/shapes/asteroid_shapes.html

Benner, L. (2013b). Binary and ternary near-earth asteroids. Retrieved March 13, 2014, from http://echo.jpl.nasa.gov/~lance/binary.neas.html

Binzel, R. P., A'Hearn, M., Asphaug, E., Barucci, M. A., Belton, M., Benz, W., . . . Zuber, M. T. (2003). Interiors of small bodies: Foundations and perspectives. *Planetary & Space Science, 51*(7), 443. doi:10.1016/S0032-0633(03)00051-5

Binzel, R. P., & Kofman, W. (2005). Internal structure of near-earth objects. *Comptes Rendus Physique, 6*(3), 321-326. doi:10.1016/j.crhy.2005.01.001

Britt, D. T., Yeomans, D., Housen, K., & Consolmagno, G. (2002). Asteroid density, porosity, and structure. *Asteroids III, , 485-500.

Broschart, S. B. (2006). *Close proximity spacecraft maneuvers near irregularly shaped small bodies: Hovering, translation, and descent.* University of Michigan).

Busch, M. W., Benner, L. A. M., Ostro, S. J., Giorgini, J. D., Jurgens, R. F., Rose, R., . . . Hine, A. A. (2008). Physical properties of near-earth asteroid (33342) 1998 WT24. *ICARUS, 195*(2), 614-621. doi:10.1016/j.icarus.2008.01.020

Busch, M. W., Giorgini, J. D., Ostro, S. J., Benner, L. A. M., Jurgens, R. F., Rose, R., . . . Margot, J. (2007). Physical modeling of near-earth asteroid (29075) 1950 DA. *ICARUS, 190*(2), 608-621. doi:10.1016/j.icarus.2007.03.032

Busch, M. W., Ostro, S. J., Benner, L. A. M., Giorgini, J. D., Jurgens, R. F., Rose, R., . . . Broschart, S. B. (2006). Radar and optical observations and physical modeling of near-earth asteroid 10115 (1992 SK). *ICARUS, 181*(1), 145-155. doi:10.1016/j.icarus.2005.10.024

Carry, B. (2012). Density of asteroids. *Planetary & Space Science, 73*(1), 98-118. doi:10.1016/j.pss.2012.03.009

Carry, B., K., Carry, B., Kaasalainen, M., Merline, W. J., Müller, T. G., . . . Sierks, H. (2012). Shape modeling technique KOALA validated by ESA rosetta at (21) lutetia. *Planetary and Space Science, 66*(1), 200-212. doi:10.1016/j.pss.2011.12.018

Cheng, A. F., Barnouin-Jha, O., Prockter, L., Zuber, M. T., Neumann, G., Smith, D. E., . . . Thomas, P. (2002). Small- scale topography of 433 eros from laser altimetry and imaging. *Icarus, 155*(1), 51-74. doi:10.1006/icar.2001.6750

Cheng, A. F. (2002). Near earth asteroid rendezvous: Mission summary. *Asteroids III,* , 351-366.

Church, C., & Fevig, R. (2013). A feasibility study on the characterization of the internal structure of small neos with small spacecraft. Paper presented at the *Lunar and Planetary Institute Science Conference Abstracts, , 44* 2999.

Colombo, O. L. (1984). *The global mapping of gravity with two satellites* Netherlands Geodetic Commission. Retrieved from http://www.ncgeo.nl/phocadownload/28Colombo.pdf

De Luise, F., Perna, D., Dotto, E., Fornasier, S., Belskaya, I. N., Boattini, A., . . . Fulchignoni, M. (2007). Physical investigation of the potentially hazardous asteroid (144898) 2004 VD17. *ICARUS, 191*(2), 628-635. doi:10.1016/j.icarus.2007.05.018

Demura, H., Kobayashi, S., Nemoto, E., Matsumoto, N., Furuya, M., Yukishita, A., . . . Hirata, N. (2006). Pole and global shape of 25143 itokawa. *Science, 312*(5778), 1347-1349.

Doody, D. (2001). *The basics of space flight* JPL. Retrieved from http://www2.jpl.nasa.gov/basics/editorial.php

Dotto, E., Barucci, M. A., Binzel, R. P., & Delbó, M. (2005). Surface compositions of NEOs. *Comptes Rendus Physique, 6*(3), 303-312. doi:10.1016/j.crhy.2004.12.015

Enzer, D. G., Wang, R. T., & Klipstein, W. M. (2010). GRAIL — A microwave ranging instrument to map out the lunar gravity field. Paper presented at the *Frequency Control Symposium (FCS), 2010 IEEE International,* 572-577.

Flury, J., Bettadpur, S., & Tapley, B. D. (2008). Precise accelerometry onboard the GRACE gravity field satellite mission. *Advances in Space Research, 42*(8), 1414-1423. doi:10.1016/j.asr.2008.05.004

Fujiwara, A., Kawaguchi, J., Yeomans, D. K., Abe, M., Mukai, T., Okada, T., . . . Nakamura, R. (2006). The rubble-pile asteroid itokawa as observed by hayabusa. *Science, 312*(5778), 1330-1334.

Gaskell, R., Olivier Barnouin-Jha, Scheeres, D., Mukai, T., Hirata, N., Abe, S., . . . Kominato, T. (2006). Landmark navigation studies and target characterization in the hayabusa encounter with itokawa. Paper presented at the doi:10.2514/6.2006-6660

GRACE fact sheet. (2003). Retrieved February 28, 2012, from http://grace.jpl.nasa.gov/files/GRACE_Fact_Sheet.pdf

GRACE orbital configuration. (2010). Retrieved February 22, 2014, from http://www.csr.utexas.edu/grace/operations/configuration.html

Hamilton, D. P., & Burns, J. A. (1991). Orbital stability zones about asteroids. *Icarus, 92*(1), 118-131. doi:10.1016/0019-1035(91)90039-V

Han, S. (2004). Efficient determination of global gravity field from satellite-to-satellite

    tracking mission. *Celestial Mechanics and Dynamical Astronomy, 88*(1), 69-102.

    doi:10.1023/B:CELE.0000009383.07092.1f

Hayabusa-the final approach. (2010). Retrieved November, 20, 2013, from

    http://hayabusa.jaxa.jp/e/

Hofmann-Wellenhof, B., & Moritz, H. (2005). *Physical geodesy* WienNewYork.

Jekeli, C. (1999). The determination of gravitational potential differences from satellite-

    to-satellite tracking. *Celestial Mechanics and Dynamical Astronomy, 75*(2), 85-101.

    doi:10.1023/A:1008313405488

JPL small-body database browser. (2014). Retrieved January 22, 2014, from

    http://ssd.jpl.nasa.gov/sbdb.cgi?sstr=itokawa;orb=0;cov=1;log=0;cad=0#elem

Kawaguchi, J., Fujiwara, A., & Uesugi, T. (2008). Hayabusa—Its technology and science

    accomplishment summary and hayabusa-2. *Acta Astronautica, 62*(10), 639-647.

    doi:10.1016/j.actaastro.2008.01.028

Kim, J., & Lee, S. W. (2009). Flight performance analysis of GRACE K-band ranging

    instrument with simulation data. *Acta Astronautica, 65*(11), 1571-1581.

    doi:10.1016/j.actaastro.2009.04.010

Kochetova, O. (2004). Determination of large asteroid masses by the dynamical method.

    Solar System Research, 38(1), 66-75. doi:10.1023/B:SOLS.0000015157.65020.84

Kohout, T., Kiuru, R., Montonen, M., Scheirich, P., Britt, D., Macke, R., & Consolmagno, G. (2011). Internal structure and physical properties of the asteroid 2008 TC₃inferred from a study of the almahata sitta meteorites. *ICARUS, 212*(2), 697-700. doi:10.1016/j.icarus.2011.01.037

Konopliv, A. S., Park, R. S., Yuan, D., Asmar, S. W., Watkins, M. M., Williams, J. G., . . . Zuber, M. T. (2013). The JPL lunar gravity field to spherical harmonic degree 660 from the GRAIL primary mission. *Journal of Geophysical Research: Planets, 118*(7), 1415-1434. doi:10.1002/jgre.20097

Konopliv, A. S., Miller, J. K., Owen, W. M., Yeomans, D. K., Giorgini, J. D., Garmier, R., & Barriot, J. (2002). A global solution for the gravity field, rotation, landmarks, and ephemeris of eros. *ICARUS, 160*(2), 289. doi:10.1006/icar.2002.6975

Koschny, D., Drolshagen, J., & Bobrinsky, N. (2010). Relevance of asteroid occultation measurements to determination of characteristics of near-earth objects. *Cosmic Research, 48*(5), 403-408. doi:10.1134/S0010952510050059

Lederer, S. M., D., Lederer, S. M., Domingue, D. L., Vilas, F., Abe, M., . . . Takagi, Y. (2005). Physical characteristics of hayabusa target asteroid 25143 itokawa. *Icarus, 173*(1), 153-165. doi:10.1016/j.icarus.2004.07.022

Lemoine, F. G., Goossens, S., Sabaka, T. J., Nicholas, J. B., Mazarico, E., Rowlands, D. D., . . . Zuber, M. T. (2013). High– degree gravity models from GRAIL primary mission data. *Journal of Geophysical Research: Planets, 118*(8), 1676-1698. doi:10.1002/jgre.20118

Lockheed Martin. (2011). GRAIL fact sheet. Retrieved February, 2012, from
http://www.lockheedmartin.com/content/dam/lockheed/data/space/documents/grail/
GRAIL_FactSheet_2011.pdf

Ma, C., Arias, E. F., Eubanks, T. M., Fey, A. L., Gontier, A. M., Jacobs, C. S., . . .
Charlot, P. (1998). The international celestial reference frame as realized by very
long baseline interferometry. \aj, 116, 516-546. doi:10.1086/300408

Michalak, G. (2000). Determination of asteroid masses --- I. (1) ceres, (2) pallas and (4)
vesta. \aap, 360, 363-374.

Miller, J. K., Konopliv, A. S., Antreasian, P. G., Bordi, J. J., Chesley, S., Helfrich, C. E., .
. . Scheeres, D. J. (2002). Determination of shape, gravity, and rotational state of
asteroid 433 eros. *ICARUS, 155*(1), 3. doi:10.1006/icar.2001.6753

Montenbruck, O., & Gill, E. (2000). *Satellite orbits: Models, methods, and applications*
Springer Berlin Heidelberg.

Morrison, D. e. (1992). *The spaceguard survey: Report of the NASA international near-
earth object detection workshop. jet propulsion laboratory/california institute of
technology, pasedena, CA, january 25, 1992.* Pasedena, CA: Jet Propulsion
Laborator/California Institute of Technology.

Mukai, T., A., Mukai, T., Abe, S., Hirata, N., Nakamura, R., . . . Yoshikawa, M. (2007).
An overview of the LIDAR observations of asteroid 25143 itokawa. *Advances in
Space Research, 40*(2), 187-192. doi:10.1016/j.asr.2007.04.075

Near earth object program. (2014). Retrieved February 28, 2014, from

    http://neo.jpl.nasa.gov/neo/groups.html

Ostro, S. J., Benner, L. A. M., Nolan, M. C., Magri, C., Giorgini, J. D., Scheeres, D. J., . .

    . Jong, E. M. (2004). Radar observations of asteroid 25143 itokawa (1998 SF36.

    Meteoritics & Planetary Science, 39(3), 407-424. doi:10.1111/j.1945-

    5100.2004.tb00102.x

Pol', V. G. (2011). Dynamical parameters of spacecraft motion near small celestial body.

    Solar System Research, 45(7), 614-621. doi:10.1134/S0038094611070239

Scheeres, D. J. (2004). Close proximity operations for implementing mitigation

    strategies. *2004 Planetary Defens Conference: Protecting Earth from Asteroids,*

    Orange County, California.

Scheeres, D. J., Broschart, S., Ostro, S., & Benner, L. (2004). The dynamical

    environment about asteroid 25143 itokawa, target of the hayabusa mission.

    AIAA/AAS Astrodynamics Specialist Conference and Exhibit, doi:10.2514/6.2004-

    4864

Scheeres, D. J. (2012a). Orbital mechanics about small bodies. *Acta Astronautica, 72*, 1-

    14. doi:10.1016/j.actaastro.2011.10.021

Scheeres, D. J., Gaskell, R., Abe, S., O, B., Hashimoto, T., Kawaguchi, J., . . . Uo, M.

    (2006). The actual dynamical environment about itokawa. American Institute of

    Aeronautics and Astronautics. doi:10.2514/6.2006-6661

Scheeres, D. J. (2012b). *Orbital motion in strongly perturbed environments: Applications to asteroid, comet and planetary satellite orbiters* Springer.

Somenzi, L., F., Somenzi, L., Fienga, A., Laskar, J., & Kuchynka, P. (2010). Determination of asteroid masses from their close encounters with mars. *Planetary and Space Science, 58*(5), 858-863. doi:10.1016/j.pss.2010.01.010

STK 10.1 central body coordinate systems. (2014). Retrieved June 3, 2013, from http://www.agi.com/resources/help/online/stk/10.1/index.html

STK 10.1 integrator. (2014). Retrieved October 31, 2013, from http://www.agi.com/resources/help/online/stk/10.1/index.html

STK 10.1 solar radiation pressure. (2014). Retrieved October 29, 2013, from http://www.agi.com/resources/help/online/stk/10.1/index.html

Tapley, B. D., Bettadpur, S., Ries, J. C., Thompson, P. F., & Watkins, M. M. (2004). GRACE measurements of mass variability in the earth system. *Science, 305*(5683), 503-505.

Wertz, J. R., & Larson, W. J. (1999). *Space mission analysis and design* Springer Netherlands.

Zimmer, M., Williams, K., Johnson, J., Church, C., Fevig, R., & Semke, W. (2014). Precision control of autonomous spacecraft during close-proximity NEO operations using classical control methodologies. Paper presented at the *Lunar and Planetary Institute Science Conference Abstracts, , 45* 2226.

Zuber, M. T., Smith, D. E., Watkins, M. M., Asmar, S. W., Konopliv, A. S., Lemoine, F. G., . . . Yuan, D. (2013). Gravity field of the moon from the gravity recovery and interior laboratory (GRAIL) mission. *Science, 339*(6120), 668.